

SPARK PLASMA SINTERING OF TITANIUM  
ALUMINIDE INTERMETALLICS AND ITS  
COMPOSITES

By

ABDELHAKIM AHMED ALDOSHAN

Bachelor of Science in Mechanical Engineering

King Saud University

Riyadh, Saudi Arabia

2005

Submitted to the Faculty of the  
Graduate College of the  
Oklahoma State University  
in partial fulfillment of  
the requirements for  
the Degree of  
MASTER OF SCIENCE  
July, 2012

SPARK PLASMA SINTERING OF TITANIUM  
ALUMINIDE INTERMETALLICS AND ITS  
COMPOSITES

Thesis Approved:

Dr. Sandip P. Harimkar

---

Thesis Adviser

Dr. Raman P. Singh

---

Dr. Kaan A. Kalkan

---

Dr. Sheryl A. Tucker

---

Dean of the Graduate College

## TABLE OF CONTENTS

Chapter	Page
1. INTRODUCTION .....	1
1.1 Intermetallics.....	1
1.2 Aluminum and its Properties .....	2
1.3 Titanium and its Properties .....	4
1.4 Titanium Aluminides: A Review .....	4
1.4.1 Phase Diagram of Titanium Aluminides.....	5
1.4.2 Microstructure of Titanium Aluminides .....	7
1.4.3 Mechanical properties of Titanium Aluminides .....	10
1.4.4 Importance of Titanium Aluminides as Structural Material .....	14
1.4.5 Difficulties with Titanium Aluminides .....	14
1.4.6 Titanium Aluminides with Other Aluminides .....	15
1.4.7 Applications of Titanium Aluminides .....	16
1.5 Processing Methods of Titanium Aluminides.....	19
1.5.1 Reactive Sintering .....	20
1.6 Spark Plasma Sintering.....	22
1.6.1 Spark Plasma Sintering Parameters.....	24
1.6 Spark Plasma Sintering of Titanium Aluminides .....	25
1.7 Objective .....	26
2. EXPERIMENTAL DETAILS .....	27
2.1 Materials .....	27
2.2 Ball Milling.....	28
2.3 Spark Plasma Sintering.....	28
2.4 Fabrication of Bulk Samples of Titanium Aluminides and Composites .....	30
2.5 Characterization and Testing Methods .....	31
2.5.1 Density Measurement .....	31

Chapter	Page
2.5.2 Phase and Microstructure Analysis.....	32
2.5.3 Wear Test.....	32
2.6 Mechanical Testing.....	33
2.6.1 Microhardness.....	33
2.6.2 Compression Test.....	33
3. RERSULTS AND DISCUSSION .....	35
3.1 Characterization of the Milled Powder .....	35
3.2 Spark Plasma Sintering of Titanium Aluminides .....	37
3.2.1 Effect of the Sintering Temperature on Density .....	40
3.2.2 Effect of the Sintering Temperature on Ti-Al Phases Formation .....	42
3.2.3 Effect of the Sintering Temperature on Evolution of the Microstructure .....	45
3.2.4 Microhardness and Compression Testing Analysis of Titanium Aluminides .....	51
3.2.5 Fractography of the Spark Plasma Sintered Titanium Aluminides .....	53
3.2.6 Wear Analysis of the Spark Plasma Sintered Titanium Aluminides .....	56
3.3 Spark Plasma Sintering of Graphene reinforced Titanium Aluminides composites.....	62
3.3.1 Effect of the Sintering Temperature on Density .....	62
3.3.2 Effect of the Sintering Temperature on Ti-Al Composites Phases Formation .....	63
3.3.3 Microhardness and Compression testing Analysis .....	67
3.3.4 Fractography of Spark Plasma Sintered Titanium Aluminides Composites .....	70
3.3.5 Wear analysis of Titanium Aluminide Composites .....	73
4. CONCLUSIONS.....	82
5. FUTURE WORK.....	84
REFERENCES .....	85

## LIST OF TABLES

Table		Page
Table 1.1	Comparing some physical and mechanical properties of TiAl with its constituent elements.....	3
Table 1.2	Effect of alloying elements on $\gamma$ -TiAl intermetallics.....	12
Table 1.3	Mechanical properties of various $\gamma$ -TiAl fabricated with alloying elements.....	13
Table 1.4	Physical and mechanical properties of aluminide intermetallics.....	16
Table 2.1	Specifications of the materials used in the current work.....	27
Table 3.1	XRD TiAl toTi <sub>3</sub> Al ratio of titanium aluminide composites at different temperatures.....	66

## LIST OF FIGURES

Figure		Page
Fig. 1.1	Density of some light and heavy metals.....	3
Fig. 1.2	Binary phase diagram of titanium aluminides.....	5
Fig. 1.3	Crystal structures of the three main titanium aluminides.....	7
Fig. 1.4	Heat treatment of TiAl for different microstructures.....	8
Fig. 1.5	Dual TiAl intermetallics microstructures: a) Near $\gamma$ , b) Duplex, c) Nearly lamellar, and d) Fully lamellar.....	9
Fig. 1.6	Effect of increasing Al content on the Vickers hardness and elongation of binary Ti-Al alloys.....	11
Fig. 1.7	Gamma titanium aluminide turbine engine blade.....	17
Fig. 1.8	Low pressure $\gamma$ titanium aluminides turbine rotor of CF6-80C engine.....	18
Fig. 1.9	Gamma titanium aluminides high performance car valves.....	19
Fig. 1.10	Mechanism of SPS process.....	21
Fig. 1.11	Schematic diagram of Spark Plasma Sintering set up.....	23
Fig. 2.1	Spark Plasma Sintering machine components.....	29
Fig. 2.2	Two different assemblies of graphite dies.....	30
Fig. 2.3	Schematic description of ball milling and SPS of titanium aluminides and titanium aluminide composites.....	31
Fig. 2.4	Compression testing equipment.....	34
Fig. 3.1	SEM micrograph of milled Ti-Al powders.....	36

Figure		Page
Fig. 3.2	SEM micrograph of milled Ti-Al-graphene powders.....	36
Fig. 3.3	X-ray diffraction patterns of ball milled Ti-Al powder with a) 0%wt. graphene, b) 2 wt.% graphene and c) 4 wt.% graphene.....	37
Fig. 3.4	Typical spark plasma sintered disc shapes of titanium aluminide composites.....	38
Fig. 3.5	Temperature and punch displacement variation during spark plasma sintering of titanium aluminides and its composites.....	39
Fig. 3.6	Punch displacement variation during spark plasma sintering of titanium aluminides and its composites.....	39
Fig. 3.7	Density of SPS titanium aluminide samples at different temperatures.....	41
Fig. 3.8	Porosity of titanium aluminide samples sintered at different temperatures.....	41
Fig. 3.9	Free energy of formation of Ti-Al intermetallic compounds as a function of temperature.....	43
Fig. 3.10	XRD patterns of a) Ti-Al powder, and spark plasma sintered samples at, b) 900 °C, c) 1000 °C and d) 1100 °C, and b) 1200 °C.....	45
Fig. 3.11	a) and b) SEM micrograph of 900 °C, c) and d) EDS images of (b).....	46
Fig. 3.12	Sample sintered at 1000 °C a) and b) SEM micrograph, c) and d) SEM micrograph of the etched surface, e) and f) EDS images of (c).....	48
Fig. 3.13	Sample sintered at 1100 °C a) and b) SEM micrograph, c) and d) SEM micrograph of the etched surface, e) and f) EDS images of (c).....	49
Fig. 3.14	Sample sintered at 1200 °C a) and b) SEM micrograph, c) and d) SEM micrograph of the etched surface, e) and f) EDS images of (c).....	50
Fig. 3.15	Microhardness values of titanium aluminide samples sintered at different temperatures.....	51
Fig. 3.16	Compressive stress-strain curves of SPS titanium aluminide compound..	53

Figure		Page
Fig. 3.17	Fracture surfaces of compressive loading samples sintered at (a) - (b) 900 °C, (c) - (d) 1000 °C, (e) - (f) 1100 °C, and (g) - (h) 1200 °C.....	55
Fig. 3.18	Cumulative weight loss versus sliding time of spark plasma sintered titanium aluminide samples fabricated at different temperatures.....	56
Fig. 3.19	Total weight loss as a function of sliding time of spark plasma sintered titanium aluminide samples fabricated at different temperatures.....	57
Fig. 3.20	Average coefficient of friction as a function of sliding time of SPS titanium aluminide samples fabricated at different temperatures.....	58
Fig. 3.21	Line profiles across the wear track of SPS samples at different temperatures.....	60
Fig. 3.22	Surface profiles of wear tracks of SPS titanium aluminide samples fabricated at (a) 900 °C, (b) 1000 °C, (c) 1100 °C, and (d) 1200 °C.....	61
Fig. 3.23	Density of SPS titanium aluminide composite samples at different sintering temperatures.....	63
Fig. 3.24	XRD patterns of a) Ti-Al-graphene powder, and titanium aluminide composites (2 wt.% graphene) samples sintered at, b) 900 °C, c) 1000 °C, d) 1100 °C, and e) 1200 °C.....	65
Fig. 3.25	XRD patterns of a) Ti-Al-graphene powder, and titanium aluminide composites (4 wt.% graphene) samples sintered at, b) 900 °C, c) 1000 °C, d) 1100 °C, and e) 1200 °C.....	65
Fig. 3.26	Vickers's microhardness of SPS titanium aluminide composites (0, 2 and 4 wt.% graphene) fabricated at different temperatures.....	67
Fig. 3.27	Compressive stress-strain curves of SPS titanium aluminide composites (2 wt.% graphene) fabricated at different temperatures.....	68
Fig. 3.28	Compressive stress-strain curves of SPS titanium aluminide composites (4 wt.% graphene) fabricated at different temperatures.....	68
Fig. 3.29	Fracture surfaces of compressive loading samples (2 wt.% graphene) sintered at (a) - (b) 900 °C, (c) - (d) 1000 °C, (e) - (f) 1100 °C, and (g) - (h) 1200 °C.....	70



Figure		Page
Fig. 3.30	Fracture surfaces of compressive loading samples (4 wt.% graphene) sintered at (a) - (b) 900 °C, (c) - (d) 1000 °C, (e) - (f) 1100 °C, and (g) - (h) 1200 °C.....	71
Fig. 3.31	Cumulative weight loss as a function of sliding time of SPS titanium aluminide composites samples (2 wt.% graphene) fabricated at different temperatures.....	73
Fig. 3.32	Cumulative weight loss as a function of sliding time of SPS titanium aluminide composites samples (4 wt.% graphene) fabricated at different temperatures.....	73
Fig. 3.33	Total weight loss as a function of sliding time of sintered titanium aluminide composites samples (0, 2, 4 wt.% graphene) fabricated at different temperatures.....	74
Fig. 3.34	Average coefficient of friction as a function of sliding time of sintered titanium aluminide composite samples (2 wt.% graphene) fabricated at different temperatures.....	75
Fig. 3.35	Average coefficient of friction as a function of sliding time of sintered titanium aluminide composite samples (4 wt. % graphene) fabricated at different temperatures.....	76
Fig. 3.36	Line profiles across the wear track of SPS titanium aluminide composite samples (2 wt.% graphene) fabricated at different temperatures.....	77
Fig. 3.37	Surface profiles of wear tracks of sintered titanium aluminide composites (2 wt.% graphene) fabricated at (a) 900 °C, (b) 1000 °C,(c) 1100 °C, and (d) 1200 °C.....	78
Fig. 3.38	Line profiles across the wear track of SPS titanium aluminide composite samples (4 wt.% graphene) fabricated at different temperatures.....	79
Fig. 3.39	Surface profiles of wear tracks of sintered titanium aluminide composites (4 wt.% graphene) fabricated at (a) 900 °C, (b) 1000 °C,(c) 1100 °C, and (d) 1200 °C.....	80

## CHAPTER 1

### INTRODUCTION

#### 1.1 Intermetallics

Intermetallics represent a manifold class of materials that possess intermediate properties between metallic and non-metallic materials. The intermetallics compounds are formed by a combination of two or more metals and exhibit different crystal structure and properties than their constituent elements. Since the early ages (2500 B.C.), the metallurgists have used intermetallics in many applications in different life aspects because of their attractive properties. Some of the applications of intermetallics are in coating of bronze tools, ornamental parts, mirror, dental restorative, printing, superconductors, permanent magnets, and high temperature structural components (automotive and aeroengines parts) [1]. The iron and nickel intermetallics such as  $\text{Fe}_3\text{Al}$ ,  $\text{FeAl}$ ,  $\text{Ni}_3\text{Al}$ , and  $\text{NiAl}$  played a significant role as structural materials specifically in high temperature applications. On the other hand, titanium aluminides such as  $\text{TiAl}$  and  $\text{Ti}_3\text{Al}$  present significant potential to be a good replacement to existing conventional titanium alloys, iron aluminides, and nickel superalloys [2]. A lot of interest has been given lately to  $\gamma\text{-TiAl}$  intermetallic compound due to its excellent properties at high temperature structural applications. This work will be mainly focused on the processing of  $\gamma\text{-TiAl}$  from elemental powders (Ti and Al).

## 1.2 Aluminum and its Properties

Aluminum is one of the most well-known non-ferrous metals in the earth. It is the third most abundant element in the earth's crust. Since the discovery of aluminum element, it has been the target of all metallurgists to involve it in most daily products. Aluminum possesses attractive physical and mechanical properties such as low density (Fig. 1.1), strength, high ductility as it is listed in Table 1.1 [3]. Therefore, it is found that aluminum is suitable for lightweight products, light or unloaded structural applications, and high formability related applications such as thin packing foils. Aluminum has become part of daily life products that range from cheap to highly advanced products. Most of the applications of aluminum are in beverages cans, food packaging, aluminum foils, structural applications, automobile/aerospace industry, and office and lab appliances.

Considering all excellent physical and mechanical properties of aluminum, it has become an important element in many alloys and intermetallics. Iron, nickel, and titanium aluminides compounds are solid examples of the use of aluminum in intermetallics industry. Changing aluminum content in titanium-aluminum system leads to different titanium aluminide compounds such as  $\gamma$ -TiAl,  $\alpha_2$ -Ti<sub>3</sub>Al and TiAl<sub>3</sub> as well as influences physical, tribological and mechanical properties [4].

**Table 1.1** Comparing some physical and mechanical properties of TiAl with its constituent elements [3].

Property	Aluminum	Titanium	TiAl-based intermetallic
Density	2.7 g/cm <sup>3</sup>	4.5 g/cm <sup>3</sup>	3.7-3.9 g/cm <sup>3</sup>
Melting temperature	660 °C	1670 °C	1480 °C
Yield strength	7-11 MPa	910 MPa	400-650 MPa
Vickers hardness	0.167 GPa	1.23-1.35 GPa	2-3.1 GPa
Young's modulus	70 GPa	115 GPa	160-180 GPa

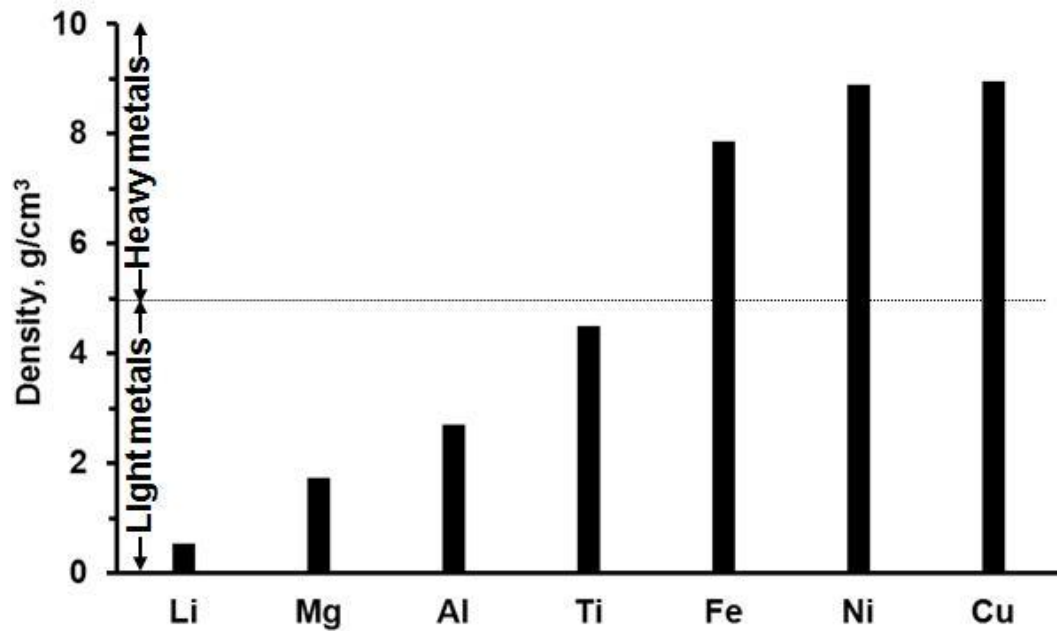


**Fig. 1.1** Density of some light and heavy metals.

### 1.3 Titanium and its Properties

Since discovery of titanium in 1791, it has attracted the attention and has become one of the most popular metals in engineering related projects. Titanium is a non-ferrous transition element and it is the fourth most abundant structural element in the earth's crust. Furthermore, synthesizing titanium is complex because it is difficult to find titanium in a pure form due to natural tendency of titanium to react with other elements such as nitrogen and oxygen. On the other hand, in terms of the physical and mechanical properties as shown in Table 1, titanium possesses excellent properties compared with aluminum. Furthermore, titanium is classified among light-weight metals which makes it denser than aluminum as well as lighter than iron as shown in Fig. 1.1. Titanium exhibits higher corrosion resistance in severe corrosive environments than aluminum. In addition, due to low thermal conductivity of titanium, high temperatures that result during machining of Ti leads to poor machinability. Moreover, high tendency of titanium to react with gases in air during machining makes it difficult to get well-manufactured parts [5]. Titanium has become a part of many structural and other engineering applications [6]; some of the applications are in aircraft frames and engines, exterior walls and roofing of buildings, sporting goods (bicycle frames, golf club heads, tennis rackets, etc.), bio-implants, and automotive components (valve, connecting rods, fasteners, suspension springs, etc).

### 1.4 Titanium Aluminides: A Review

Titanium aluminides are intermetallic compounds of titanium and aluminum. In the equilibrium state of Ti-Al system, several phases such as disordered intermetallic phases, disordered solution phases and ordered intermetallic phases can be formed. The ordered intermetallic titanium aluminides,  $\alpha_2$ -Ti<sub>3</sub>Al and  $\gamma$ -TiAl, possess attractive properties particularly at high temperature structural applications (~ 700 °C).  $\gamma$ -TiAl exhibits better properties at high temperature range

(~ 700 °C) in comparison with  $\alpha_2$ -Ti<sub>3</sub>Al and occupies a good position with Ni-based superalloys [7].

#### 1.4.1 Phase Diagram of Titanium Aluminides

The binary phase diagram in Ti-Al system shows different intermetallic phases that result from reaction between titanium and aluminum. There are three thermodynamically equilibrium phases, the stoichiometric phases, the disordered solution phases and the ordered intermetallic phases. The stoichiometric phases are TiAl<sub>2</sub> and Ti<sub>2</sub>Al<sub>5</sub>. Also, the disordered solution phases consist of liquid-Ti and liquid-Al. The last category in the Ti-Al equilibrium phases is the ordered intermetallic phases which are  $\alpha_2$ -Ti<sub>3</sub>Al,  $\gamma$ -TiAl, and TiAl<sub>3</sub> [8].

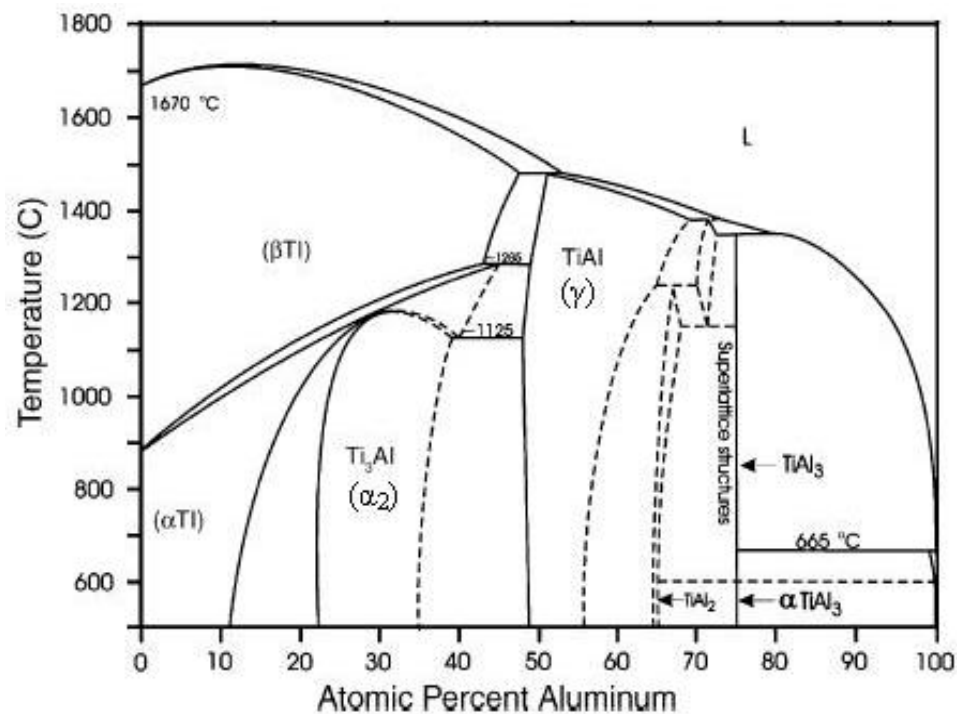


**Fig. 1.2** Binary phase diagram of titanium aluminides (with permission from [9]).

$\alpha_2$ -Ti<sub>3</sub>Al phase (DO<sub>19</sub>) has a homogeneity range extending at the room temperature from 23 at.% up to about 38 at.% Al as shown in the binary phase diagram of Ti-Al system (Fig. 1.2 [9]). Intermetallic compound Ti<sub>3</sub>Al is formed during cooling through  $\beta \rightarrow \alpha \rightarrow \alpha_2$ . Therefore, the structural ordering range of Ti<sub>3</sub>Al compound is between 1125 °C and 1150 °C [10]. Moreover,  $\gamma$ -TiAl has composition range from 34 at.% to about 64 at.% Al; either a single  $\gamma$  (L1<sub>0</sub>) phase (48 at.% to 56 at.%Al) or a dual phase of  $\alpha_2 + \gamma$  can be formed [11]. During cooling to  $\gamma$ -TiAl, the peritectic reaction is  $L + \alpha \rightarrow \gamma$  [12]. Also, the favorable solidification transformation of intermetallics with aluminum content (at.%) between 49 and 55 is  $L \rightarrow \alpha + L \rightarrow \alpha + \gamma \rightarrow \gamma$ . Moreover, cooling of the dual phase ( $\alpha_2 + \gamma$ ) follows the path:  $L \rightarrow \beta + L \rightarrow \beta + \alpha \rightarrow \alpha \rightarrow \beta + \gamma \rightarrow \alpha_2 + \gamma$  and the disadvantage of this solidification path is that during the transformation to  $\alpha$  phase,  $\beta$  phase becomes unstable and leads to stacking faults. Also,  $\alpha_2 + \gamma$  titanium aluminides can solidify by passing through the phase and leads to two reactions:  $\alpha \rightarrow \alpha_2 \rightarrow \alpha_2 + \gamma$  or  $\alpha \rightarrow \alpha + \gamma \rightarrow \alpha_2 + \gamma$ . Thus,  $\alpha_2 + \gamma$  phase characterizes TiAl based intermetallics at high temperatures field.  $\gamma$ -TiAl remains ordered up to the melting point [13].

Crystal structure of the ordered titanium aluminides phases is an hcp for  $\alpha_2$ -Ti<sub>3</sub>Al, and fcc for both  $\gamma$ -TiAl and TiAl<sub>3</sub>, as shown in Fig. 1.3 [14]. Over last four decades, a lot of research and developments have been carried out on the ordered group of titanium aluminides. In addition, TiAl<sub>3</sub> exhibits very low ductility at elevated temperatures compared with two other phases ( $\alpha_2$ -Ti<sub>3</sub>Al and  $\gamma$ -TiAl). Therefore, structural transformation has been made to TiAl<sub>3</sub> by adding ductile metals such as copper or iron, yet the ductility has not exhibited a significant improvement. On the other hand, large homogeneity range of both  $\alpha_2$ -Ti<sub>3</sub>Al, and  $\gamma$ -TiAl in solid solution allows them to accept particular alloying elements in substitution; thus, that has led to promising results in terms of ductility particularly at high temperatures tests [15]. One of the major issues of Ti<sub>3</sub>Al phase is high absorption of hydrogen and oxygen at high rates which affects its performance by inducing embrittlement at elevated temperatures. However, the attention toward developing pure

Ti<sub>3</sub>Al intermetallic compounds has been reduced. Thus, most of the interest recently is on either near Gamma ( $\alpha_2 + \gamma$ ) titanium aluminides or on  $\gamma$ -TiAl intermetallic compounds [16].

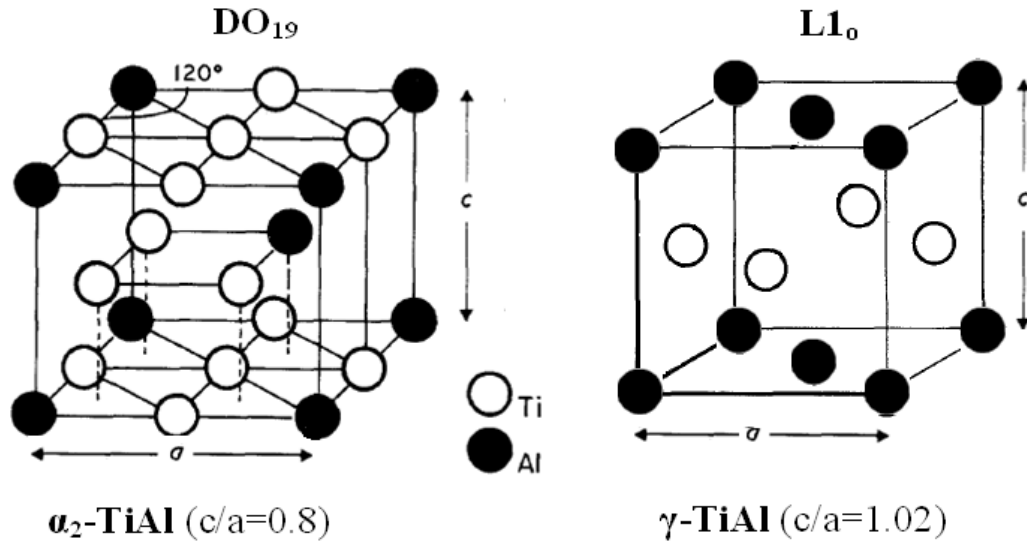


**Fig. 1.3** Crystal structures of the three main titanium aluminides (with permission from [14]).

#### 1.4.2 Microstructure of Titanium Aluminides

The microstructure of TiAl intermetallics plays significant role in controlling and enhancing mechanical properties. The formation of different microstructures is influenced by heat treatment. There are four categories of microstructures in dual phase titanium aluminides compounds, near Gamma, duplex, nearly lamellar, and fully lamellar resulted from the thermal treatment at temperatures  $T_1$ ,  $T_2$ ,  $T_3$  and  $T_4$ , respectively as shown in Fig. 1.4 [17]. Near Gamma microstructure is achieved by annealing titanium aluminides to a temperature below the eutectoid temperature ( $T_1$ ). Near Gamma is characterized by non-uniform microstructure and has equiaxed coarse  $\gamma$  grains and fine stringers  $\gamma$  grains that are pinned at the grain boundaries by  $\alpha_2$  particles, as shown in Fig. 1.5 (a). The average grain size of near Gamma microstructure is between 30 to 50  $\mu\text{m}$ .



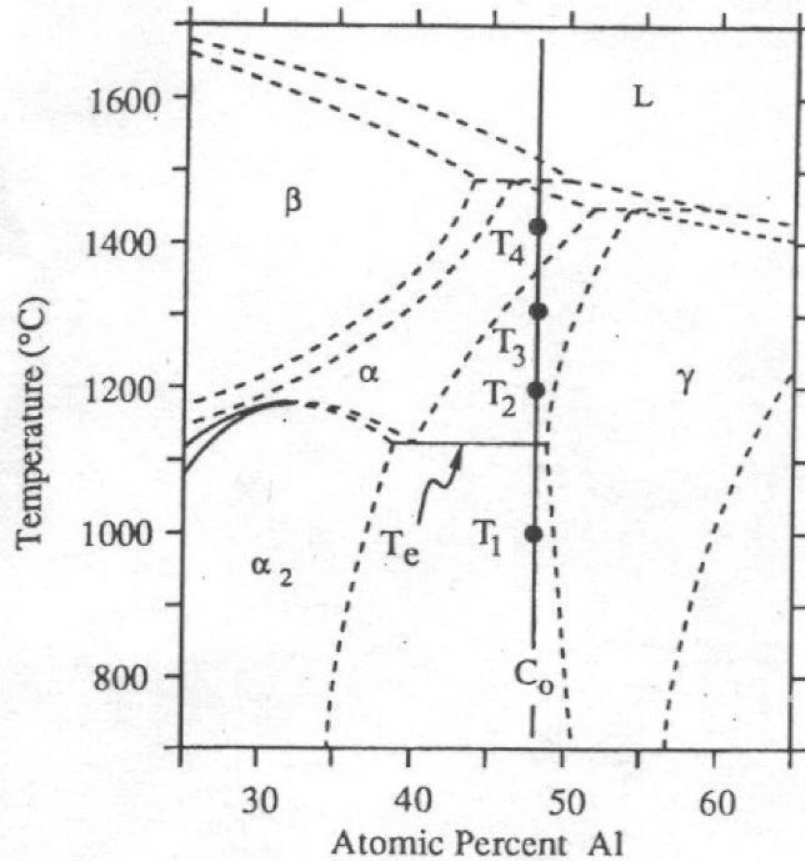


**Fig. 1.4** Heat treatment of TiAl for different microstructures (with permission from [17]).

Thermal treatment up to  $T_2$  leads to the formation of duplex microstructure which has an equal volume ratio between  $\alpha_2$  and  $\gamma$ . This microstructure contains both fine Gamma grains together with colonies of fully fine lamellar; thus, the produced fine microstructure is due to the growth competition between  $\gamma$  and  $\alpha_2$ . The average grain size of duplex fine microstructure is about 10  $\mu\text{m}$ , as shown in Fig. 1.5 (b). Further heat treatment to a temperature  $T_3$  produces near lamellar microstructure. Near lamellar microstructure is characterized by coarse  $\alpha_2$  lamellar grains as the major constituent and the other minor amount is left to fine  $\gamma$  grains, as shown in Fig. 1.5 (c).

The other microstructure of dual titanium aluminides is fully lamellar which is formed by heat treatment up to temperature  $T_4$  lying in  $\alpha$  field. This microstructure consists of

crystallographically related plates which are alternated between  $\gamma$  and  $\alpha_2$ . Fully lamellar microstructure is formed due to growth of  $\alpha$ -Ti in between  $\gamma$  and  $\alpha_2$  plates during cooling to the room temperature. The average grain size of the fully lamellar microstructure is in range between 200 to 1000  $\mu\text{m}$ , as shown in Fig. 1.5 (d).

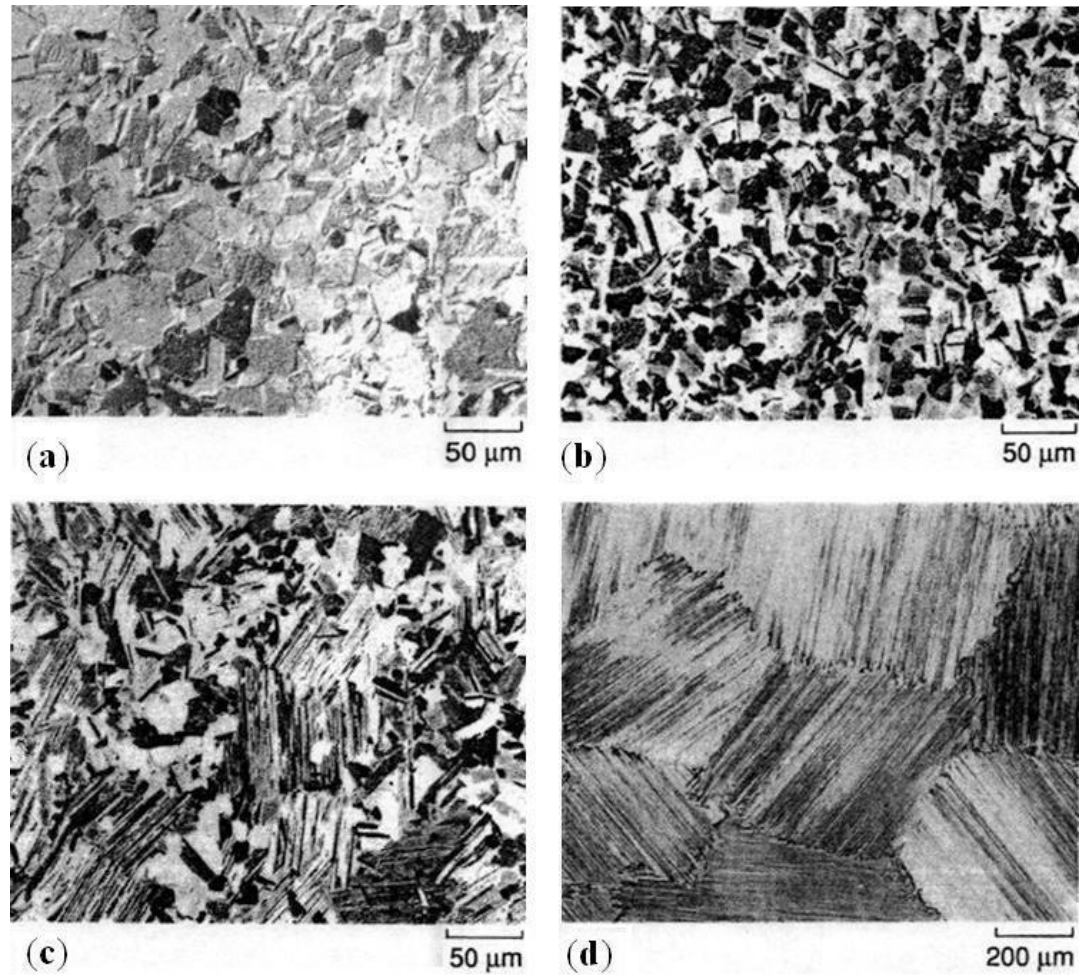


**Fig. 1.5** Dual TiAl intermetallics microstructures: a) Near  $\gamma$ , b) Duplex, c) Nearly lamellar, and d) Fully lamellar (with permission from [18]).

Among these four titanium aluminide microstructures, fully lamellar microstructure exhibits the highest fatigue and creep resistance, yet coarse grains lead to low room temperature strength and ductility. However, highest strength and ductility at the room temperature is

obtained by duplex microstructure, but it also suffers from very low creep and fatigue resistance. Therefore, attention has been drawn towards obtaining optimized properties through developing  $\gamma$  titanium aluminides combining the features of fully lamellar and duplex microstructures [19].

### **1.4.3 Mechanical properties of Titanium Aluminides**

$\gamma$ -titanium aluminide intermetallics exhibit poor ductility, low creep, fatigue and fracture toughness at room temperature, and improved mechanical properties at high temperatures. However, dual phase ( $\alpha_2 + \gamma$ ) titanium aluminide intermetallics show better ductility and strength at room temperature than that of single  $\gamma$ -TiAl phase. Also, mechanical properties of the dual phase ( $\alpha_2 + \gamma$ ) are dependent on microstructural morphology. High strength and ductility at room temperature are obtained by duplex microstructure whereas fully lamellar microstructure leads to high temperature creep and fatigue resistance. Moreover, ductility of lamellar microstructure can be improved as the grain size of lamellae reduces. Fracture toughness of coarser grains is independent of the grain size, yet coarser grains exhibit development in the creep resistance [20; 21].

Mechanical properties are also sensitive to the change in aluminum content over the range of dual phase to single  $\gamma$  phase. It has been observed that  $\gamma$ -TiAl compounds show a decrease in Vickers microhardness at room temperature as aluminum content varies from 46 at.% to 53 at.%. However, significant increase in Vickers microhardness is observed for samples having aluminum content  $> 53$  at.%, as shown in Fig. 1.6. Also, elongation at room temperature of dual phase titanium aluminides increases as composition of aluminum ranges between 45.5 at.% to 47 at.% and beyond this range a decreasing trend is observed. Low aluminum content in titanium aluminides enhances strength, yet that decreases ductility and oxidation resistance [22].

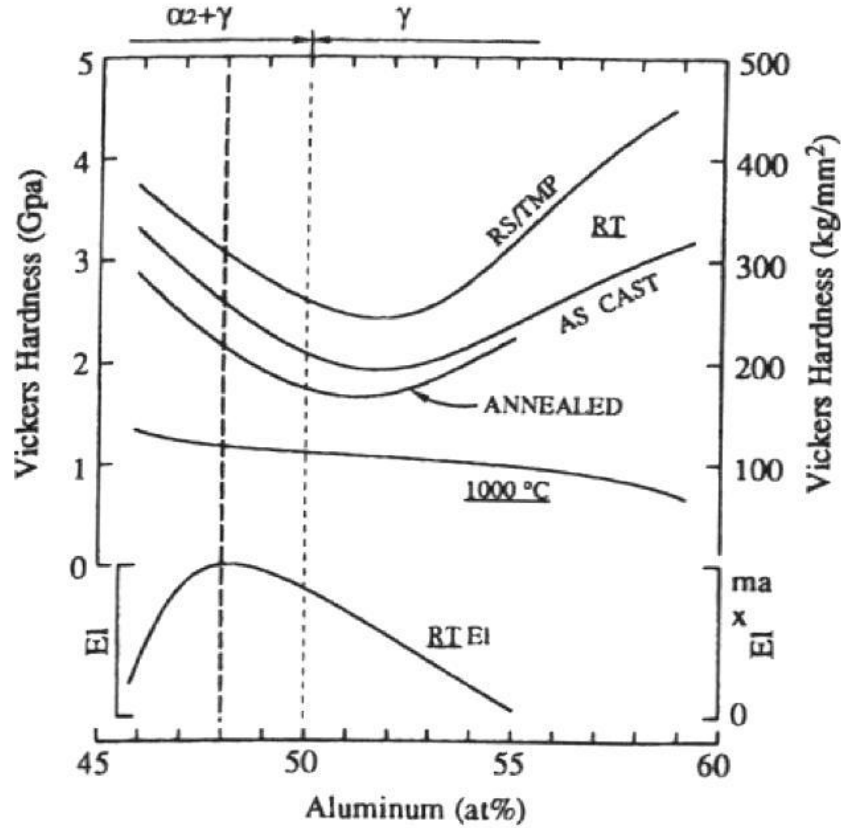


**Fig.1.6** Effect of increasing Al content on the Vickers hardness and elongation of binary Ti-Al alloys (with permission from [22]).

Alloying elements such as B, Cr, V, W, Si, C, Mo and Nb are used with  $\gamma$ -TiAl in order to improve room temperature mechanical properties [23]. Hence, addition of these elements in only small percentages leads to better mechanical properties. Alloying guidelines have been established for  $\gamma$ -TiAl to design intermetallics with desired properties, as shown in table 1.2 [24]. Table 1.3 presents different  $\gamma$ -TiAl compounds consisting of different additives with their corresponding processing conditions. This table was constructed based on tensile test data conducted at room temperature (RT) as well as at high temperatures. Mechanical properties, yield strength ( $\sigma_y$ ), fracture strength ( $\sigma_f$ ), elongation ( $\epsilon_f$ ) and fracture toughness ( $K_{IC}$ ), have clearly influenced by alloying elements in different levels [25].

**Table 1.2** Effect of alloying elements on  $\gamma$ -TiAl intermetallics [24].

<b>Alloying additives</b>	<b>Effect</b>
0.2 - 2 at.% of Boron	Refine grains
	Stabilize microstructure at elevated temperatures
2 at.% for each V, Mn and Cr	Improve ductility
1 - 2 at.% Nb	Increase oxidation resistance
0.2 - 2at.% for each W, Si, C, and Mo	Improve creep resistance

**Table 1.3** Mechanical properties of various  $\gamma$ -TiAl fabricated with alloying elements [25]

Alloy at. %	Processing	T °C	$\sigma_y$ MPa	$\sigma_f$ MPa	$\epsilon_f$ %	$K_{IC}$ MPa m <sup>1/2</sup>
Ti-48Al-1V-0.3C-0.2 O	(Forging + HT*)	RT7	392	406	1.4	12.3
		60	320	470	11	
Ti-48Al-1V-0.2C-0.14 O	(Forging + HT)	RT8	480	530	1.5	-
		15	360	450	-	
Ti-48Al-2Cr-2Nb	(Casting + HIP* + HT)	RT7	331	413	2.3	20-30
		60	310	430	-	
Ti-45Al-1.6Mn	Reactive sintering	RT8	465	566	1.4	-
		00	370	540	14	
Ti-47.3Al-0.7V-1.5Fe-0.7B	Casting	RT8	-	520	0.6	-
		00		424	40	
Ti-46.2Al-xCr-y(Ta,Nb)	(Casting + HT)	RT7	425	520	1.0	22
		60	350	460	2.5	
Ti-46Al-4Nb-1W	(Extrusion + HT)	RT7	648	717	1.6	-
		60	517	692	-	
Ti-47Al-2Mn-2Nb-0.8TiB <sub>2</sub>	(Casting + HIP + HT)	RT7	402	482	1.5	15-16
		60	344	458	-	-

\*Hot isostatic pressing (HIP) and heat treatment (HT).

#### **1.4.4 Importance of Titanium Aluminides as Structural Material**

$\gamma$ -TiAl possesses excellent properties such as low density, high melting point, high Young's modulus and strength, and good resistant to oxidation and creep. Considering such excellent physical and mechanical properties,  $\gamma$ -titanium aluminide intermetallics have exhibited significant potential to replace conventional alloys used in high temperature structural applications due to high specific strength. Also, high melting temperature allows  $\gamma$ -TiAl compounds to be more stable in the range of low and high temperatures. Automotive and aeroengines industries have employed some of titanium aluminide products to replace the existing Ti-6242 and IMI 834 alloys. Titanium aluminides exhaust valves, turbocharger wheels, and low pressure turbine blades are in service [26; 27].

#### **1.4.5 Difficulties with Titanium Aluminides**

The major disadvantage of titanium aluminides is poor/limited ductility at room to intermediate temperatures ( $< 500\text{ }^{\circ}\text{C}$ ). Lacking of this important mechanical property, however, puts titanium aluminides behind other structural materials possessing high ductility such as Ni-superalloys. This also makes titanium aluminides limited to engineering designs with low ductility requirements. Other challenges with titanium aluminides are processing and production costs that are still uncompetitive to those of Ni-superalloys [28].

Other physical and mechanical properties outweigh poor ductility at the service temperature as well as create broader interest in developing more ductile components especially at the elevated temperatures. Also, developments in manufacturing techniques lead to more competitive prices of titanium aluminides products. Thus, in order to overcome this ductility limitation, a lot of effort has been put towards developing titanium aluminide intermetallics based on  $\gamma$ -TiAl to obtain a more reliable and sustainable ductility at both room temperature and elevated temperatures [29].

#### 1.4.6 Titanium Aluminides with Other Aluminides

Iron aluminide intermetallics compounds are based on FeAl and Fe<sub>3</sub>Al phases. The iron aluminides exhibit unique properties like high temperature corrosion and oxidation resistance, and low cost. However, environmental embrittlement can be observed in the presence of water vapor. Iron aluminides' yield strength is temperature dependent decreasing with the increase in testing temperature. As listed in Table 1.4, iron aluminides show higher Young's modulus compared with nickel and titanium aluminides. The iron aluminides have higher density than titanium aluminides. In addition, nickel aluminides are mostly based on intermetallic phases Ni<sub>3</sub>Al and NiAl which exhibit excellent mechanical properties at room temperature such as ductility. High corrosion resistance is also observed in air, carburizing and oxidizing atmospheres. The nickel aluminides show dependency of yield strength on testing temperature. Among aluminide intermetallics (iron, nickel, and titanium), nickel aluminides possess the highest density [30-33].

Titanium aluminide intermetallics that are based on  $\alpha_2$ -Ti<sub>3</sub>Al and  $\gamma$ -TiAl have a density about half of that for superalloys (9.1 g/cm<sup>3</sup>). Also,  $\gamma$ -TiAl possesses lower density than that of iron and nickel aluminides. Melting temperature of  $\gamma$ -TiAl is comparable to melting temperatures of iron and nickel aluminides. Young's modulus of  $\gamma$ -TiAl is relatively high. Therefore,  $\gamma$ -TiAl appears to be future excellent replacement to iron and nickel aluminides in the high temperatures structural applications (up to 700 °C) [34].



**Table 1.4** Physical and mechanical properties of aluminide intermetallics [29, 30].

Phase Property	Fe <sub>3</sub> Al	FeAl	Ni <sub>3</sub> Al	NiAl	Ti <sub>3</sub> Al	TiAl
<b>Crystal-Structure</b>	D0 <sub>3</sub>	B2	L1 <sub>2</sub>	B2	D0 <sub>19</sub>	L1 <sub>0</sub>
<b>Density g/cm<sup>3</sup></b>	6.72	6.1	7.5	6.5	4.15	3.76
<b>Melting-Temperature °C</b>	1520	1310	1383	1638	1680	1480
<b>Young's Modulus GPa</b>	180	244- 267	180	225-235	144-149	176-185

#### 1.4.7 Applications of Titanium Aluminides

Considering the attractive properties of  $\gamma$ -TiAl intermetallics, a lot of effort has been carried out to implement these lightweight materials in commercial applications to replace conventional Ti alloys or Ni-superalloys. Also, advancement in processing technologies has helped to produce titanium aluminide components. Titanium aluminide parts are made to operate at high temperature environments [34].

**Aircraft Applications:** Aircraft components that are exposed to both high temperature and pressure are mostly dominated by Ni-superalloys. Although Ni-superalloys possess excellent physical and mechanical properties, they still suffer from high density which leads to heavy structures as well as increase in operation expenses. Moreover, lightweight  $\gamma$ -TiAl components made for aeroengines exhibited excellent performance compared with Ni-superalloys at both high

speeds and temperatures [35]. An example of that is a high-pressure rotor's blades manufactured by GKSS Research Center, Thyssen Krupp Turbinenkomponenten (Remscheid, Germany) and Rolls-Royce Deutschland (Dahlewitz, Germany) using extrusion and isothermal forging, as shown in Fig. 1.7 [36]. In addition, low pressure  $\gamma$ -titanium aluminides turbine rotor blade of CF6-80C engine was fabricated, as shown in Fig. 1.8 [37]. As an environmental purpose, it also has been proven that producing divergent flaps from titanium aluminides have led to magnificent reduction in exhaust pollution as well as good noise attenuation [38].

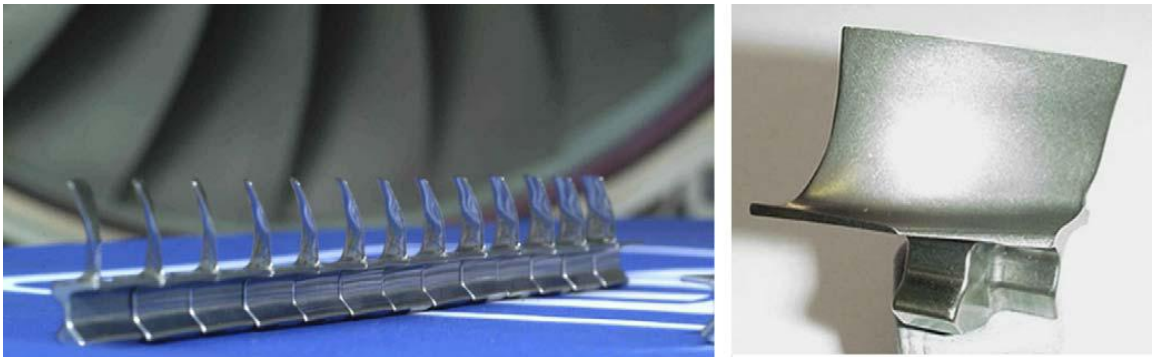


**Fig. 1.7** Gamma titanium aluminide turbine engine blade (with permission from [36]).



**Fig. 1.8** Low pressure  $\gamma$ -titanium aluminides turbine rotor of CF6-80C engine (with permission from [37]).

**Automotive Applications:** Another area of high performance applications (pressure and heat) is the automotive engines. Several advantages can be obtained through using titanium aluminide components in car's engines such as: weight reduction, efficient fuel consumption, high reliability and lifetime, enhanced performance and reduced pollution and noise [39]. An example of that is high performance  $\gamma$ -titanium aluminides car valves, as shown in Fig. 1.9 [40]. The other fields of structural applications operated at room temperature are still limited to the conventional titanium alloys. Since Gamma TiAl intermetallics are a new class of material, production cost is still high which restricts proposing them to daily-life applications (sports, house appliances, and accessories).



**Fig. 1.9** Gamma titanium aluminide high performance car valves (with permission from [40]).

### **1.5 Processing Methods of Titanium Aluminides**

Processing of the commercial  $\gamma$ -TiAl is similar to those of conventional titanium alloys and Ni-based superalloys. There are two major routes of processing titanium aluminide compounds; ingot metallurgy (IM) and powder metallurgy (PM) [41].

Ingot metallurgy route is mostly applied in large scale industries for  $\gamma$ -TiAl components [42]. Titanium aluminide compounds which are fabricated by casting (ingot metallurgy) lack chemical homogeneity due to segregation from huge differences in melting temperatures and densities between Ti and Al [43]. It is also found that obtaining fully homogenized microstructure after thermomechanical treatment (hot forging and extrusion) remains difficult leading to fluctuation in mechanical properties. Therefore, using master-alloys during fabrication of titanium aluminides is required to overcome macroscopic chemical inhomogeneity. Also, further thermomechanical (hot extrusion and annealing) treatment is required in order to obtain desired mechanical properties [44]. Microstructural evolution of cast  $\gamma$ -TiAl is sensitive to solidification

route from liquid phase (L) to  $\gamma$  phase. Therefore, solidification from  $\alpha$  phase to  $\gamma$  phase leads to coarser grains which require subsequent multistage heat-treatment to obtain good mechanical properties [45]. On the other hand, solidification from  $\beta$  results in more refined grains with insignificant segregations [46].

Producing fine and segregation free prealloyed  $\gamma$ -TiAl powder in large quantities is easy by using high pressure argon atomization. Along with that powder metallurgy (PM) technique has been largely used to fabricate titanium aluminide parts due to enhancement in consolidation methods. The advantage of using powder metallurgy over the ingot metallurgy is the ability of producing uniform microstructure titanium aluminides without requiring advance homogenizing treatment. Also, powder metallurgy produces titanium aluminides with improved chemical homogeneity and fine-grains microstructure [47]. Hot Isostatic Press (HIP) is a popular example of PM method that has been widely used to fabricate near net shape  $\gamma$ -TiAl [48]. Using HIP leads to full consolidation of  $\gamma$ -TiAl compounds with refined microstructure and without any observation of macrosegregation [48].

### **1.1 Reactive Sintering**

Reactive sintering is one of the powder metallurgy techniques involving the formation of a transient liquid phase. Powder is heated to a melting temperature of first liquid in order for the reaction to take place. Generally, reaction between solid and liquid elements occurs at the interface of contacting particles. Therefore, once the liquid spreads through the compacts, reactive sintering proceeds spontaneously leading to densification. In comparison with conventional casting technique, the major advantage of reactive sintering is low processing temperature as well as formation of homogenous materials [49].

Sintering of titanium aluminide compounds using reactive sintering has been carried out. Reactive sintering in Ti-Al system takes place through an exothermic reaction between liquid aluminum and solid titanium. According to the binary phase diagram of Ti-Al, reaction between

elemental powders of Ti(s) and Al(l) leads to the formation of TiAl<sub>3</sub>, Ti<sub>3</sub>Al, and TiAl. However, other titanium aluminides such as Ti<sub>2</sub>Al<sub>5</sub> and TiAl<sub>2</sub> can't be obtained as a result of the reaction between solid Ti and liquid Al because they require TiAl as an intermediate product of their formation. Reactive sintering also helps to control morphology and porosity of titanium aluminide products [50]. Furthermore, reactive sintering or liquid-phase sintering has the potential to be a rapid processing technique leading to fully densified near-net shape titanium aluminide compounds [51]. Along with the ability to obtain desired intermetallic phases, the reactive sintering method promises enhancement in workability of the titanium aluminide compounds can be achieved by this technique.

Reaction mechanism of the reactive sintering process that happens between elemental Ti (s) and Al (l) can be described in three steps. First, the first product of the exothermic reaction taking place at the interface of Ti (s)/Al (l) proved by many researchers is TiAl<sub>3</sub>. Secondly, TiAl<sub>3</sub> diffuses into Ti leading to the formation of  $\gamma$ -TiAl. Finally, further diffusion between remaining Ti and  $\gamma$ -TiAl leads to the formation of titanium rich phase  $\alpha_2$ -Ti<sub>3</sub>Al as shown in Fig. 1.10 [52]. Reactions during the liquid phase sintering between Ti(s) and Al(l) are in equations (1.1-1.3) [53; 54].

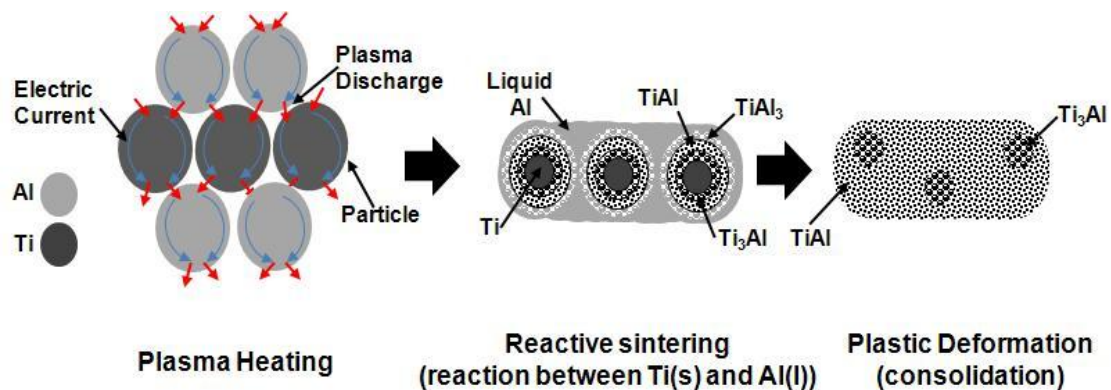


**Fig. 1.10** Mechanism of reactive SPS process (adapted from [52]).



Reaction synthesis of Ti-Al powders can be carried out using different powder metallurgy methods. Examples of these techniques are:

- Hot isostatic pressing.
- Hot extrusion reaction synthesis.
- Spark plasma sintering.

Hot isostatic pressing and hot extrusion reaction synthesis techniques require pre-compacting of the elemental powders. Also, further subsequent thermomechanical treatment may be required to obtain homogenized compounds. On the other hand, spark plasma sintering is a novel powder processing technique that processes products without any extra treatments as well as leads to near-net shape materials in a shorter time period.

## 1.6 Spark Plasma Sintering

Spark Plasma Sintering (SPS) is one of the powder metallurgy novel processing techniques. SPS process provides three main conditions: 1) vacuumed atmosphere, 2) uniaxial pressure, and 3) pulsed direct current [55]. A schematic diagram of the spark plasma sintering set up is shown in Fig. 1.11. The elemental powder is placed inside the graphite die with two graphite punches compacting from the top and bottom. Mechanism of spark plasma sintering process is based on three main stages: plasma heating, joule heating and plastic deformation. At the first stage, powder particles are locally and momentarily heated up to high temperatures due to electrical discharge. Therefore, surface layers start melting and fusing leading to necking between

powder particles. After that, necking allows electrical current to flow between powder particles increasing temperature as well as enhancing growth of grains through diffusion. Along with the diffusion, uniaxial applied pressure on soft material produces densified products. Other conventional processing techniques of titanium aluminides that require long sintering time as well as post thermomechanical treatment suffer from uncontrolled grain growth. However, the advantage of short soaking time of spark plasma sintering technique plays a crucial role in minimizing grain growth as well as leading to fully densified compacts. Therefore, the relation between high density values and grain growth of samples fabricated using spark plasma sintered can be correlated to less exposing time which means the higher the density value, the minimum the grain growth [56].

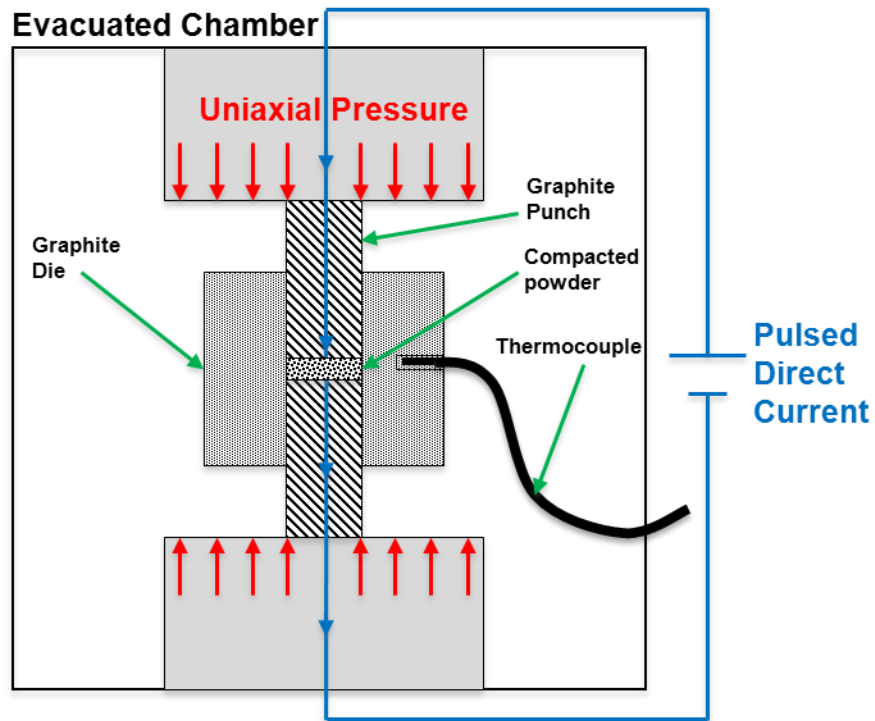


**Fig. 1.11** Schematic diagram of Spark Plasma Sintering set up.



Spark plasma sintering technique can be used to process different kind of materials such as metals, composite materials and ceramics. Thermomechanical treatment steps following other conventional fabrication methods are not required in the SPS because thermal treatment and compaction are included during sintering process leading to a stable microstructure. Moreover, it is possible to prepare fine structures (up to nano-grain) and that attributed to limited grain growth during SPS. Spark plasma sintering is short-timed process (<20 minutes) and easy to handle [57].

### 1.6.1 Spark Plasma Sintering Parameters

As of every manufacturing process, several processing parameters usually contribute in quality of final products. For spark plasma sintering, parameters influencing densification and microstructure of sintered materials are holding temperature (maximum), heating rate, holding pressure (maximum), and applied and removal load rates [58].

**Temperature:** In the SPS consolidation process, current is the source of heat which is applied to compact powder. The influence of sintering temperature obtained from current on fabricated materials can be observed in the samples' density. Hence, a relation that interprets the dependency of density on the sintering temperature is given by Garay [58].

$$\rho = s (T/T_m) + b \quad (1.4)$$

where:  $\rho$  = relative density,

$s$  = Slope (referred to the temperature sensitivity)

$T$  = Sintering temperature,

$T_m$  = Material's melting point,

$b$  = Intercept of the density axis.

Values of temperature sensitivity play a crucial role in specifying dependency of density on the sintering temperatures which means high temperature sensitivity leads to higher dependency of density on temperature and vice versa, specifically in ceramics and carbides.

**Pressure:** Presence of uniaxial load in the spark plasma sintering process plays a significant role in densification of the sintered samples. This effect can be seen on to two useful aspects during sintering. Pressure assists in rearranging the activated powder particles as well as clearing the agglomeration. Also, pressure accelerates the sintering process by acting as the driving force. The relation that explains the pressure effect is given as [59]:

$$\frac{d\rho}{(1-\rho)dt} = B \left( g \frac{\gamma}{x} + P \right) \quad (1.5)$$

Where  $\rho$  is fractional density,  $B$  is diffusion coefficient and temperature,  $g$  is geometrical constant,  $\gamma$  is surface energy,  $t$  is the sintering time,  $x$  is scale of particle size, and  $P$  is the applied pressure. Sintering driving force is presented by the right hand term of equation (2), and the left hand side designates the sintering driving force external applied pressure.

**Heating rate:** The effect of heating rate on compact powder is significant in the way that sintering with high heating rate helps in diminishing grain growth. High heating rate has an advantage in the sintering process by shorting the fabrication time. Sinterability increases with high heating rate through activating the powder particles which cause them to neck and diffuse on the grain boundary. Differences in measuring the exact temperatures of sintered sample from the graphite surface could affect the influence of heating rate on the densification of the sintered sample [60].

## 1.6 Spark Plasma Sintering of Titanium Aluminides

Spark plasma sintering is a novel rapid consolidation technique that has been used in fabrication of  $\gamma$ -titanium aluminides. Since last decade, the work on  $\gamma$ -TiAl intermetallics have been focused on using spark plasma sintering due to the advantage of getting fully densified samples as well as near net shape  $\gamma$ -TiAl compounds without any further thermomechanical treatment. Highly-purified samples with fine microstructure can be achieved using SPS [61].

Tae *et al.* [62] sintered TiAl intermetallics at different aluminum contents with different percentages of Cr; hence, a dense TiAl compound was fabricated. Moreover, punch displacement during compacting of TiAl powder against sintering temperature helps understanding densification behavior. It has been observed that the combustion reaction between solid titanium and liquid aluminum starts at melting of Al ~ 660 °C. It is possible to sinter titanium aluminide compound with homogenized microstructure in short time (< 10 min). Thus, Molénat *et al.* fabricated TiAl intermetallics using SPS for soaking time as short as 2 min[63] which was a crucial achievement in processing fully densified  $\gamma$ -titanium aluminides in comparison with other conventional processing methods that take around 37 hrs for similar results including subsequent thermomechanical treatment. Therefore, the novelty of SPS is concluded in fast convergence of microstructure and density with near net shape materials as well as in competitive mechanical characteristics [64; 65].

## 1.7 Objective

Most of the work on spark plasma sintering of  $\gamma$ -TiAl discussed earlier was carried out using prealloyed titanium aluminide powders as the starting materials. Also, it can be seen that fewer studies have been done on processing titanium aluminides via reactive sintering. A detailed reactive synthesis processing of titanium aluminide composites using SPS has not been studied. Therefore, the aim of this work is to:

- Fabricate  $\gamma$ -titanium aluminide intermetallics using spark plasma sintering technique at different temperatures using elemental powders of Ti and Al.
- Study the effect of sintering temperature on the formation of titanium aluminide phases as well as on mechanical and tribological properties.
- Study the influence of adding graphene nanoplatelets to titanium aluminides on the physical, tribological and mechanical properties.

## CHAPTER 2

### EXPERIMENTAL DETAILS

#### 2.1 Materials

The material used in this current study consists of pure titanium powder 99.5% which has particles' size ranges between 30-40  $\mu\text{m}$  and pure aluminum powder 99.7% with an average particle size of 14  $\mu\text{m}$ . According to Ti-Al phase diagram, the composition of both Ti and Al powders was selected based on  $\gamma$ -TiAl range which is 47 atomic % Ti and 53 atomic % Al. Also, the addition of graphene nanoplates to previously mixed Ti-Al powder was done in two weight percentages (2 wt. % and 4 wt. %). The graphene nanoplates used in this study has dimensions of 30  $\mu\text{m}$  diameter and 25 nm thickness, as shown in Table 2.1.

**Table 2.2** Specifications of the materials used in the current work.

Material	Density ( $\text{g/cm}^3$ )	Particle/Plate ( $\mu\text{m}$ )	Thickness
Ti	4.5	30-40	--
Al	2.7	~ 14	--
Graphene (GNPs)	2.1	Ø 30	25 nm

## **2.2 Ball Milling**

A high energy ball mill (Model: PULVERISETTE 7 premium line; Make: FRITSCH) was used to mix Ti and Al powders in a dry and wet milling. For dry milling, Ti and Al powders were poured into tungsten carbide jar and then tungsten carbide balls were used to mix the two powders together at speed of 350 rpm for 15 min. Also, graphene nanoplatelets were added at two different weight percentages (2% and 4%) to the already mixed Ti and Al powders with the use of polyacrylic acid PAA (0.05%) and acetone to ensure a good dispersion of graphene. The titanium aluminide composite mixture was wet milled using tungsten carbide balls at speed of 300 rpm for 4 hours.

## **2.3 Spark Plasma Sintering (SPS)**

Spark plasma sintering machine (Model: 10-3; Make: Thermal Technologies, LLC) was used to fabricate titanium aluminides materials. Fig. 2.1 shows main components of SPS machine, as power control unit, furnace chamber, vacuum and hydraulic pumps. With three power units supplying a direct current of 3000 amps and a potential of 5 V, the machine is capable of generating maximum process temperature up to 2500 °C. Also, the SPS equipment can achieve high heating rate as high as 600 °C/min. Moreover, vacuum pump can provide a highly evacuated medium inside the furnace up to 0.002-0.003 Torr preventing contamination of samples. High forces up to 100 kN can be applied on sample in the SPS using a hydrolytic pump. In the low pressure range ( $< 100$  MPa), graphite dies and punches are suitable for samples fabrication. SPS machine is equipped with a punch displacement measurement feature, which allows users to monitor punch movement during complete sintering process. The punch displacement can be used to study densification behavior of fabricated samples.

Compaction of titanium aluminide samples using SPS is achieved by placing Ti-Al powder inside a graphite die in between two punches at a required temperature and pressure. The desired sintering temperature and pressure controls the selection and design of graphite dies, punches, and spacers. Fabrication of titanium aluminides through liquid phase sintering requires a temperature above the melting temperature of Al ( $> 660\text{ }^{\circ}\text{C}$ ). High thermal conductivity particularly at elevated temperatures, abundance, and ease of machining makes the graphite to be the most widely used material in SPS process as dies, punches, and spacers. The sintered samples obtained from SPS are fabricated using two different graphite dies and punches dimensions. For most of characterizations of TiAl samples, disc shaped samples are used.

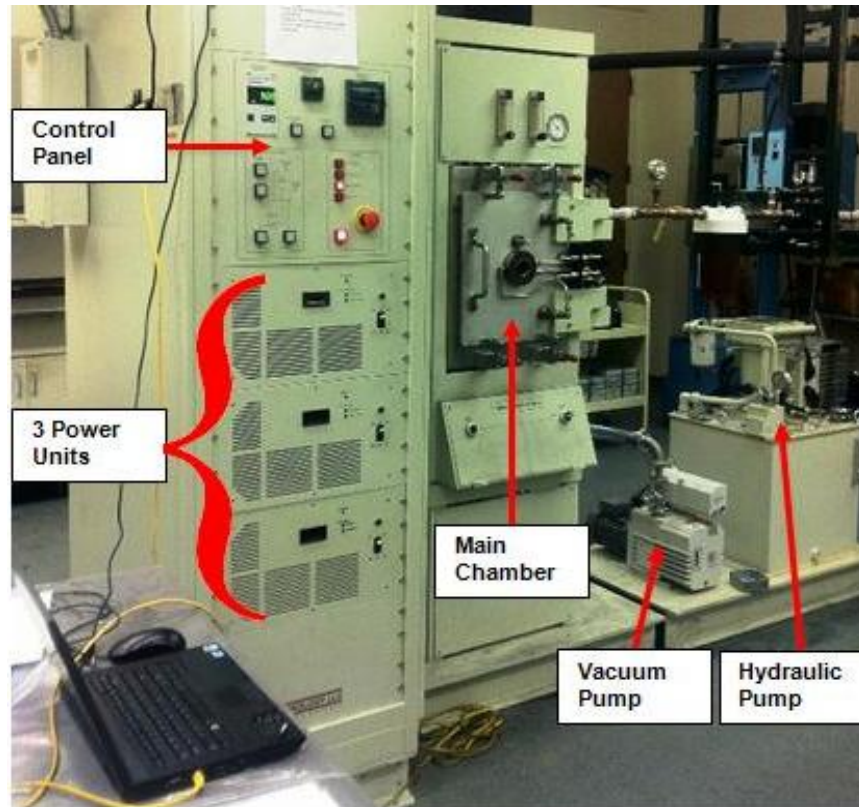


**Fig. 2.1** Spark Plasma Sintering machine components.

## 2.4 Fabrication of Bulk Samples of Titanium Aluminides and Composites

Spark plasma sintering was used to fabricate two different sets of titanium aluminide samples, as shown in Fig. 2.2. Titanium aluminides were sintered at four different temperatures (900 °C, 1000 °C, 1100 °C, and 1200 °C) and at constant pressure of 50 MPa with a heating rate of 100 °C/min and soaking time of 5 min. The samples were processed under vacuum ( $10^{-2}$  torr) throughout the experiment. For the first three temperatures up to 1100 °C, thermocouple (K type) was used to measure the temperature during the experiment, and a pyrometer was used to monitor temperature during sintering process at 1200 °C. Similarly, all processing parameters, that were used to fabricate  $\gamma$  titanium aluminides samples, were also used for the fabrication of titanium aluminide composites having 2 and 4 wt.% of graphene nanoplatelets. Fig. 2.3 presents detailed description of the experiments for sintering of both  $\gamma$  titanium aluminides and titanium aluminide composites.

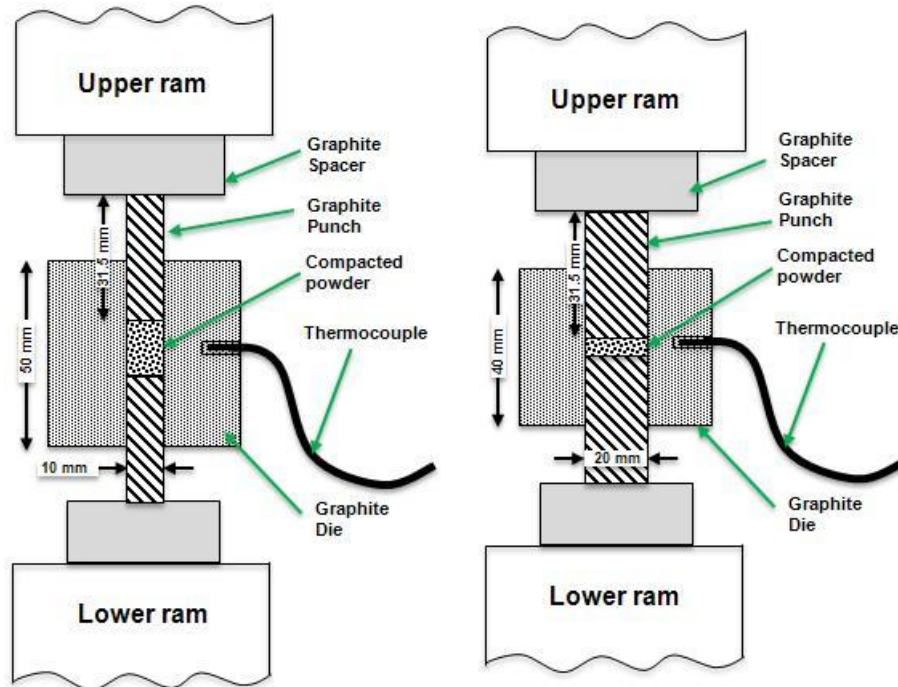


**Fig. 2.2** Two different graphite dies and punches dimensions.

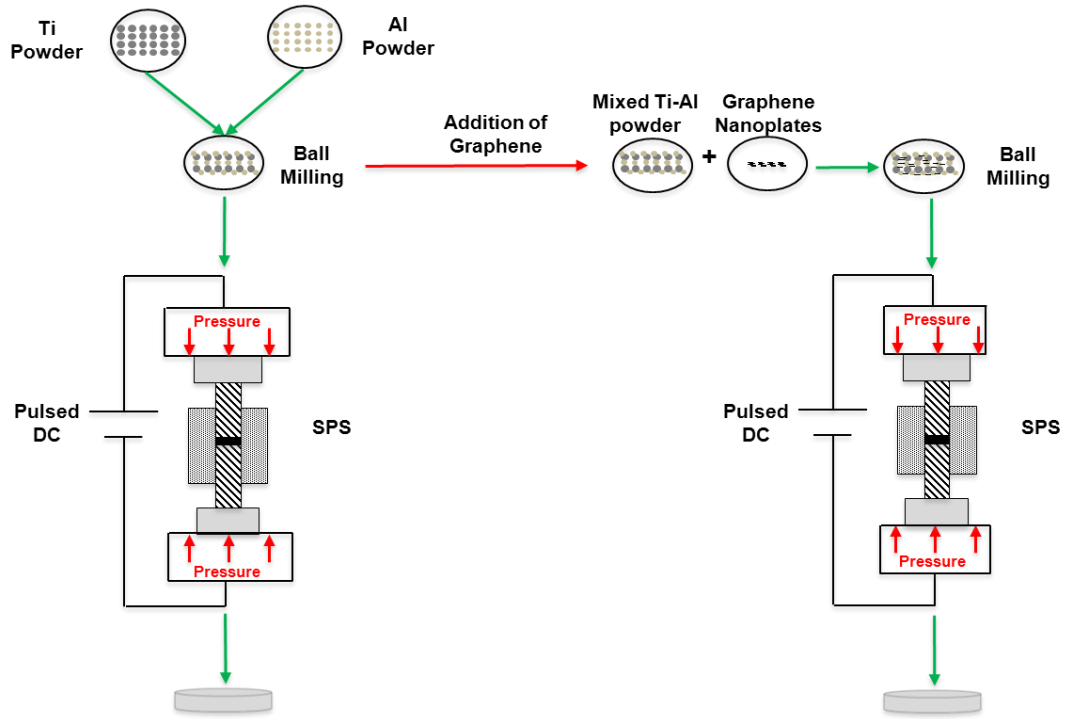


**Fig. 2.3** Schematic description of ball milling and SPS of titanium aluminides and titanium aluminide composites.

## 2.5 Characterization and Testing Methods

### 2.5.1 Density Measurement

Densities of sintered  $\gamma$ -titanium aluminide and titanium aluminide composites samples have been measured using Archimedes principle. Using this principle, density can be measured using equation 2.1.

$$\rho = \frac{x}{x-y}(\rho_0 - \rho_L) + \rho_L \quad (2.1)$$



where,  $\rho$  is density of the bulk sample;  $x$  is sample weight in air;  $y$  is weight of sample;  $\rho_o$  is auxiliary liquid density;  $\rho_L$  is density of air ( $0.0012 \text{ g/cm}^3$ ); theoretical density of titanium aluminide is  $4 \text{ g/cm}^3$ ; and water density at room temperature is  $0.99804 \text{ g/cm}^3$ .

$$\text{Percentage of densification} = \frac{\text{density of sintered sample}}{\text{Theoretical density of powder}} \times 100 \quad (2.2)$$

The measurement of density of all sintered samples was done using the density determination kit (Model: 11106706 XP/XS; Make: Mettler Toledo).

### 2.5.2 Phase and Microstructure Analysis

The x-ray diffraction (XRD) analysis of mixed powders, SPS titanium aluminide samples and titanium aluminide composites was conducted using Philips Noreco x-ray diffractometer which operates with Cu K $\alpha$  ( $\lambda = 1.54178 \text{ \AA}$ ) radiation at 45kV and 40 mA. The diffraction angle with a step increment of  $0.02^\circ$  and count time of 1 s was adjusted between  $20^\circ$  and  $80^\circ$ .

The titanium aluminide samples were etched using Kroll reagent which consists of 2 vol.% HF, 5 vol.% HNO<sub>3</sub> and 92 vol.% H<sub>2</sub>O. The microstructure characterization of etched samples was carried out using scanning electron microscope (Make: JEOL; Model: JSM-6360). Also, energy dispersive spectroscopy (EDS) was used to characterize elemental composition of the titanium aluminides matrix. EDS characterization was done using HKL EBSD system and FEI Quanta 600 field-emission-gun Environmental Scanning Electron Microscope equipped with an Evex x-ray microanalysis system.

### 2.5.3 Wear Test

Wear test of the spark plasma sintered titanium aluminide samples and titanium aluminide composites was conducted using micro-tribometer (Model: TRB; Make Nanovea Inc., Irvine, CA) with a ball-on-disc technique under dry/unlubricated conditions. An alumina ball with a 6 mm diameter was used as a counter body of wear test. Testing parameters of wear test were: 150

rpm speed, 10 N normal force, and 4 mm diameter wear track. The test was carried out for 60 min total sliding time by having test segments of 10 min. Weight loss and average coefficient of friction as a function of sliding time were reported for sintered samples. An optical surface profilometer (Model: PS50; Make Nanovea Inc., Irvine, CA) was used to get the profiles of across the wear track.

## **2.6 Mechanical Testing**

### **2.6.1 Microhardness**

Vickers microhardness of sintered samples was measured by creating an indent at a load of 15 g with a holding time of 10 s using microhardness tester. Well-polished surfaces of the titanium aluminide and titanium aluminide composite samples were prepared for microhardness testing. Average microhardness readings were reported for each sample along with the standard deviation of these readings.

### **2.6.2 Compression Test**

Spark plasma sintered titanium aluminide and titanium aluminide composite samples were fabricated to a cylindrical shape. Obtained cylindrical shaped samples have 15 mm length (L) and 10 mm diameter satisfying 1.5 L/D ratio required for compression testing as per ASTM (vol. 9) standards. The compression test was conducted using (an INSTRON 5582 series) universal testing machine operated by quasi-static mechanical loading. In order to ensure the quasi-static nature of the experiment, a  $10^{-4}$  /s strain rate was applied. For strain measurement, a laser extensometer (Model LE-05; Make: Electronic Instrument) was connected to compression testing machine through standard RS-232 and an analog ports in order to obtain accurate readings as well as to avoid steel platens compliance, as shown in Fig. 2.4.

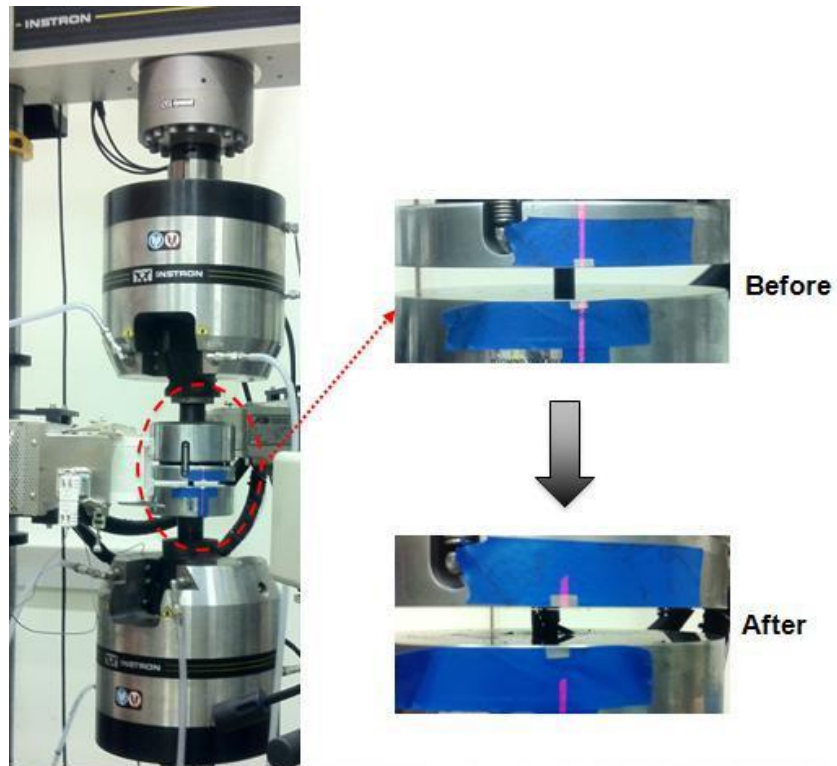


**Fig. 2.4** Compression testing equipment.

## CHAPTER 3

### RESULTS AND DISCUSSION

#### 3.1 Characterization of the Milled Powder

Titanium and aluminum milled powder was observed under the SEM as shown in Fig. 3.1. It can be clearly seen that larger titanium powder particles ( $\sim 40\text{ }\mu\text{m}$ ) and smaller aluminum powder particles ( $\sim 14\text{ }\mu\text{m}$ ) are uniformly mixed after ball milling. Formation of titanium aluminide intermetallic phases was not observed in the milled powder. Addition of graphene nanoplates to the previously mixed titanium-aluminum powder was done using the wet milling as described earlier. After the mixture dried out, the powder was also analyzed using SEM, as shown in Fig. 3.2. Similarly, wet milling didn't lead to the formation of any intermetallic or carbide phases in titanium aluminum graphene mixture.

X-ray diffraction (XRD) patterns from titanium-aluminum milled powder and titanium-aluminum-graphene nanoplatelets (2 and 4 wt.%) are presented in Fig. 3.3. XRD pattern of titanium-aluminum mixed powder shows only peaks of elemental powders Ti and Al, and there is no evidence of formation of any titanium aluminide intermetallic phases. For other mixtures containing graphene nanoplatelets, similar XRD patterns that have only elemental peaks of Ti, Al and C were observed. Peaks corresponding to titanium aluminide intermetallic phases or carbide phases were not observed in the XRD patterns of powder mixtures.

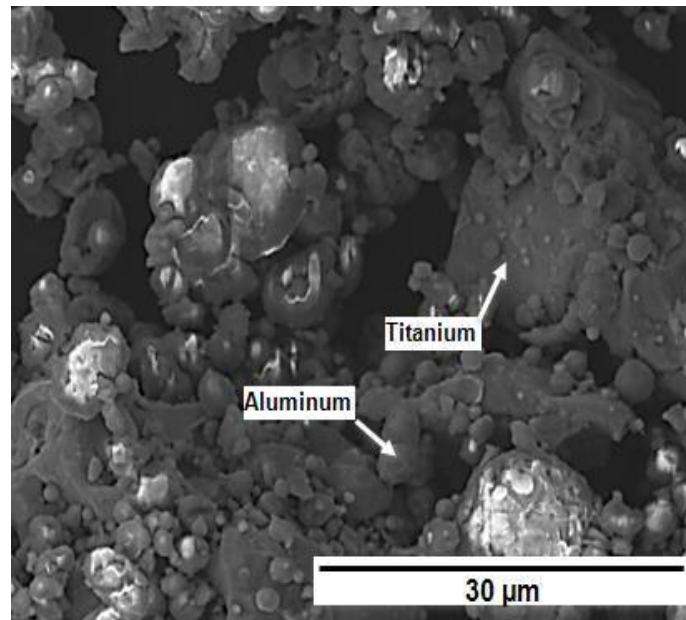


**Fig. 3.1** SEM micrograph of milled of Ti-Al powders.

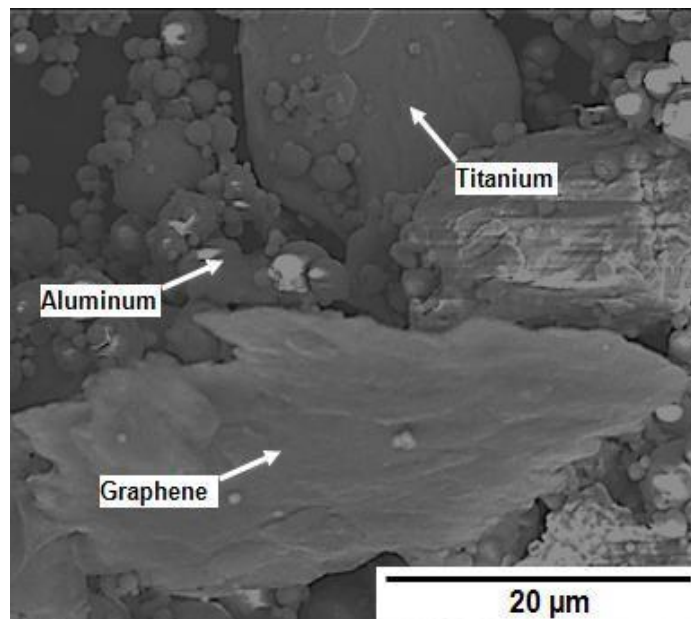


**Fig. 3.2** SEM micrograph of milled Ti-Al-graphene.

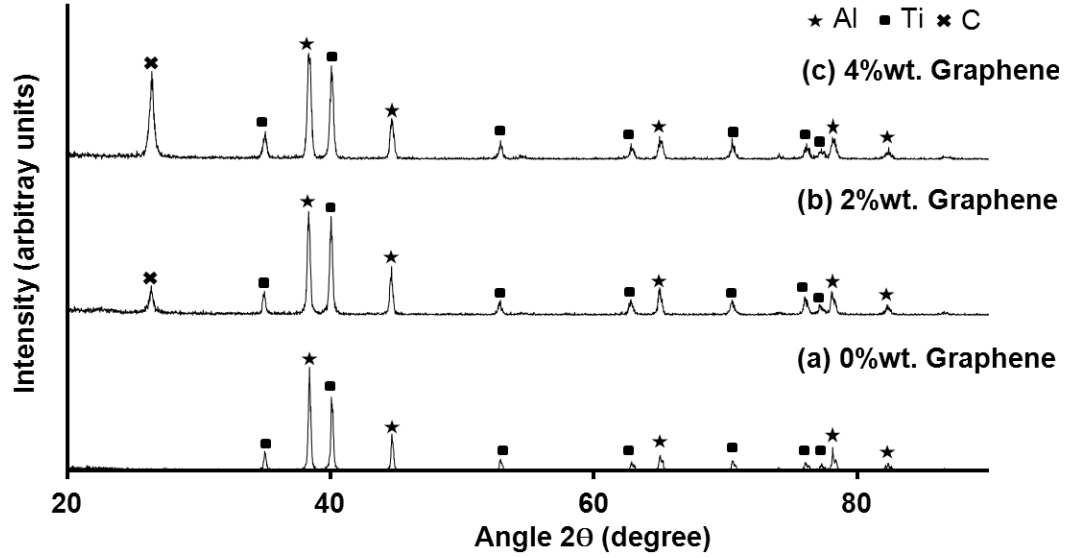


**Fig. 3.3** XRD patterns of ball milled Ti-Al powder with a) 0 wt.% graphene, b) 2 wt.% graphene and c) 4 wt.% graphene.

### 3.2 Spark Plasma Sintering of Titanium Aluminides

Spark plasma sintering of composite powders (Ti-Al; Ti-Al-graphene) was performed at temperatures from 900 °C to 1200 °C to understand the effect of sintering temperature on development of phases. Typical discs with their corresponding dimensions fabricated SPS process are shown in Fig. 3.4.

Fabrication of  $\gamma$ -titanium aluminides in this current work is based on liquid phase sintering (reactive sintering) in which an exothermic reaction takes place between solid titanium and liquid aluminum. Moreover, during liquid phase sintering of titanium aluminides samples, punch displacement fluctuation was observed as SPS temperature approached melting point of Al leading to three densification steps. Punches start moving in a contracting (densification) mode for a temperature range below 660 °C. After that, as Al melts, a retracing (expansion) mode of punches occurs. Finally, solid state diffusion and solidification take place with no further change in punch displacement. Fig. 3.5 shows both heating rate curves and punch displacement curves as

a function of processing time at four sintering temperatures (900 °C, 1000 °C, 1100 °C and 1200 °C). Also, recorded displacement values versus sintering temperature are presented in Fig. 3.6. According to recorded displacement data the initiation temperature of each sample is 667 °C, 671 °C, 698 °C, and 705 °C for samples sintered at 900 °C, 1000 °C, 1100 °C and 1200 °C, respectively. It is reported that during the liquid phase sintering (reactive synthesis) of titanium aluminide compounds using powder metallurgy techniques initiation temperature ranges between melting point of Al (600 °C) to 740 °C [62; 66].

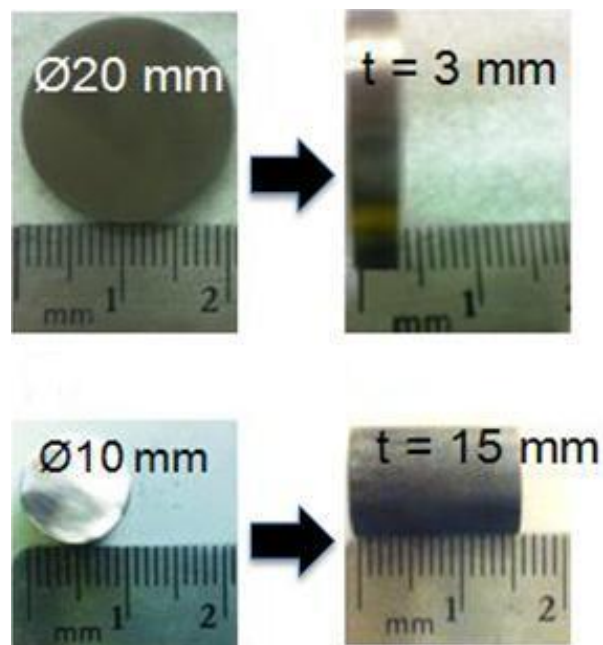


**Fig. 3.4** Typical spark plasma sintered disc shapes of titanium aluminide composites.

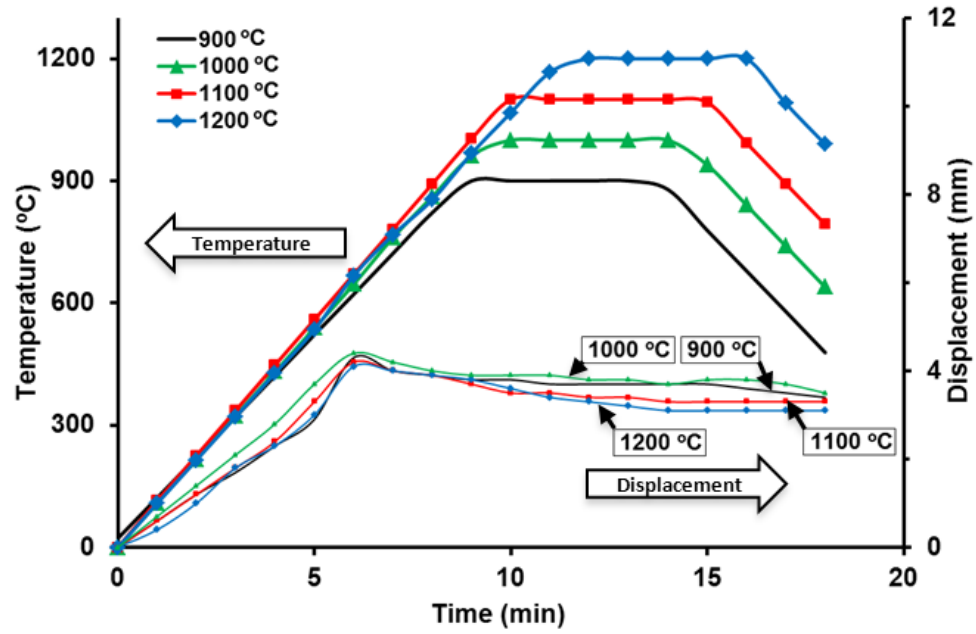


**Fig. 3.5** Temperature and punch displacement as function of processing time during spark plasma sintering of composite powders (Ti-Al; Ti-Al-graphene).

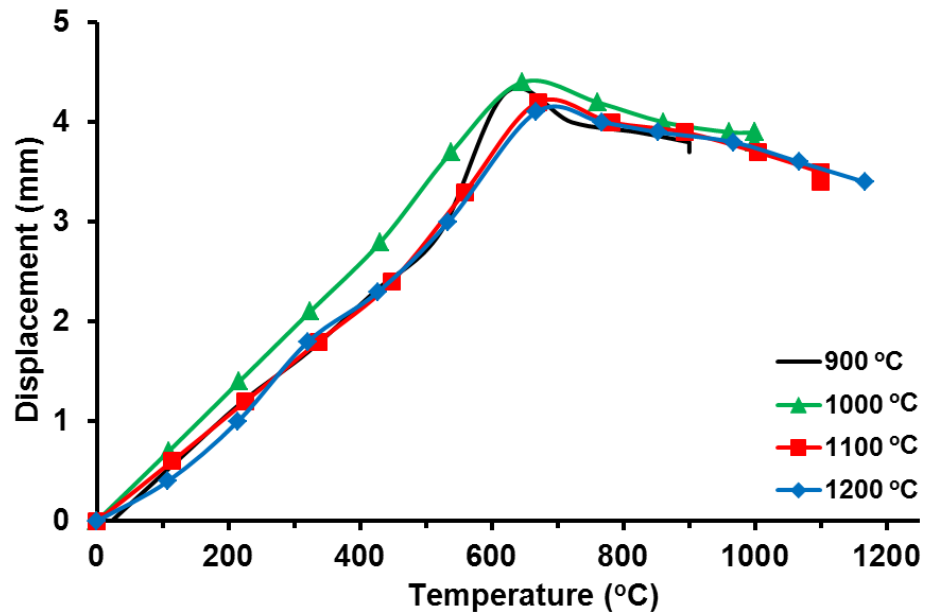


**Fig. 3.6** Punch displacement as function of sintering temperature during spark plasma sintering of composite powders (Ti-Al; Ti-Al-graphene).



### 3.2.1 Effect of the Sintering Temperature on Density

Fig. 3.7 shows the variation of density values of spark plasma sintered samples as a function of temperature. A noticeable influence of sintering temperature on the density of titanium aluminide samples was observed. As the SPS temperature increases from 900 °C to 1100 °C, a significant increase in density values was observed leading to fully densified specimens. However, further increase in sintering temperature (upto 1200 °C) does not affect density. Apparent porosity of the fabricated samples versus sintering temperature is shown in Fig. 3.8. The reactive sintering between solid titanium and liquid aluminum takes place under an exothermic reaction which leads to abrupt expansion of the compound creating porosity in sintered materials [67]. However, lower amount of porosity in titanium aluminide samples are attributed to the effect of uniaxial applied pressure during sintering process.

Considering the density values measured from sintered titanium aluminide samples of this work, these values are high attributing the reason to the processing parameters employed in the experiment. Matsugi *et al.* [68] fabricated titanium aluminide compacts using spark sintering technique over a higher sintering temperature range (1300 °C - 1400 °C) that had a composition of 47 at.% Ti and 53 at.% Al, 15-30 min soaking time, and 18.9-33 MPa applied pressure. They reported density values ranging from 3.56 to 3.71 g/cm<sup>3</sup> that were measured for samples fabricated at temperature range of (1300 °C - 1400 °C). Spark plasma sintered titanium aluminide samples of this work have shown influence of applied pressure (50 MPa) on density values at a lower sintering temperature and shorter holding time. Correlation between density values and sintering temperature of this current work follows similar trend with what was presented by Matsugi *et al.* Therefore, higher values of density of this current work are attributed to the effect of the liquid phase sintering that is accompanied with higher uniaxial pressure. Aluminum particles melt and then infiltrate into porous areas between titanium particles due to contribution of the unidirectional applied pressure. On the other hand, solid state sintering requires longer

sintering time for interdiffusion to take place between aluminum and titanium whereas shorter time is sufficient for liquid phase sintering. Furthermore, it is believed that formation of oxide film on surface of powder particles in conventional sintering methods is inevitable consequence of the process leading to an obstruction of grain to grain contact [69]; therefore, this results in low density values.

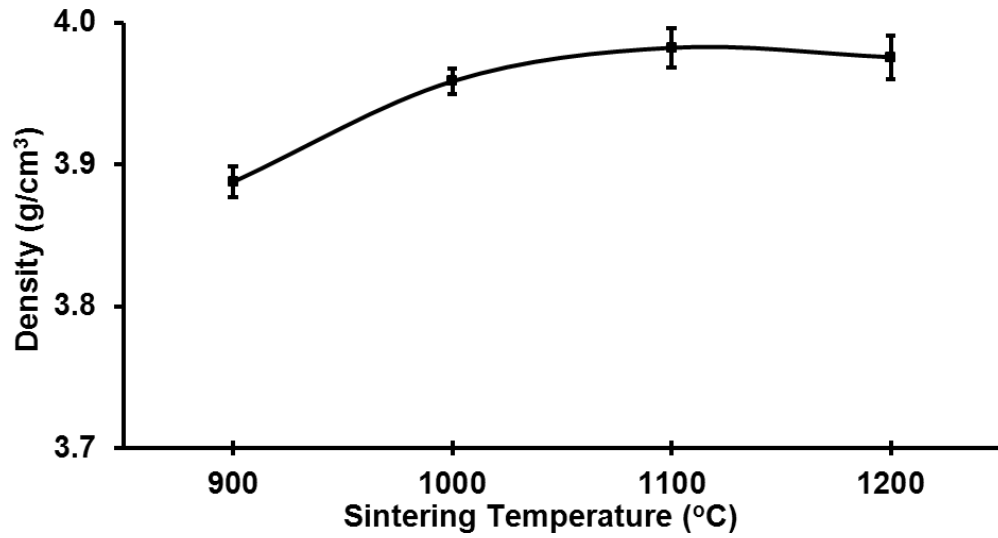


**Fig. 3.7** Density of SPS titanium aluminide samples at different temperatures.

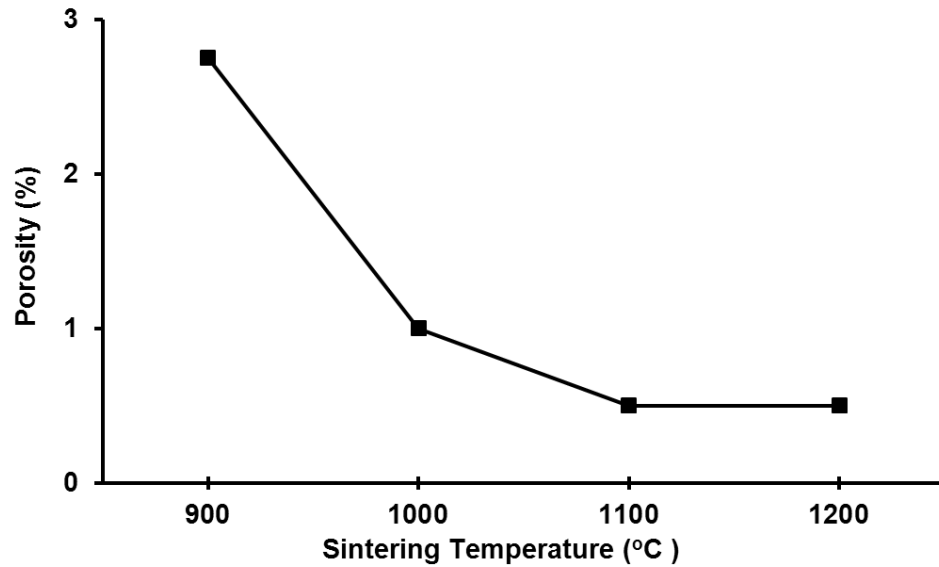


**Fig. 3.8** Porosity of titanium aluminide samples sintered at different temperatures.

### 3.2.2 Effect of the Sintering Temperature on Ti-Al Phases Formation

Gibbs free energy of formation,  $G_f$ , plays a crucial role in formation of intermetallic phases in the Ti-Al system during reaction synthesis from solid titanium with liquid aluminum. A thermodynamic assessment of the binary Ti-Al intermetallic system was done by Kattner *et al.* [70] in which they calculated Gibbs free energy of formation with processing temperature as (equations 3.1-3.5) for all titanium aluminide phases. According to Kattner model, Fig. 3.9 presents Gibbs free energy of formation of all titanium aluminide phases at four different sintering temperatures of this work. It is considered that the ordered stoichiometric phases,  $\gamma$ -TiAl,  $\alpha_2$ -Ti<sub>3</sub>Al and TiAl<sub>3</sub> prefer to form during the reaction between Ti (s) and Al (l). Although TiAl<sub>2</sub> and Ti<sub>2</sub>Al<sub>5</sub> have the lowest free energy of formation, both of them require the presence of TiAl as a starting phase.

$$\gamma\text{-TiAl} \rightarrow G_f = -37445.1 + 6.70801T \quad (3.1)$$

$$\alpha_2\text{-Ti}_3\text{Al} \rightarrow G_f = -29633.6 + 16.79376T \quad (3.2)$$

$$\text{TiAl}_3 \rightarrow G_f = -40349.6 + 10.36525T \quad (3.3)$$

$$\text{Ti}_2\text{Al}_5 \rightarrow G_f = -40495.4 + 9.52964T \quad (3.4)$$

$$\text{TiAl}_2 \rightarrow G_f = -43858.4 + 11.02077T \quad (3.5)$$

The effect of heating rate during liquid phase sintering process on the formation of titanium aluminide phases was studied thoroughly by Lee *et al.* [71]. They reported that increasing heating rate plays a significant role on formation of the main stoichiometric ordered phases (TiAl, Ti<sub>3</sub>Al and TiAl<sub>3</sub>). According to Gibbs free energy of formation map, the formation of TiAl<sub>3</sub> is favorable over other two intermetallic phases (TiAl and Ti<sub>3</sub>Al) in the presence of liquid aluminum. However, Lee *et al.* showed that at high heating rates (50-300 °C/min), TiAl and Ti<sub>3</sub>Al form first instead of TiAl<sub>3</sub>. Therefore, low heating rate (< 50 °C/min) leads to the formation of TiAl<sub>3</sub> below

melting point of Al at the interface of Ti and Al by solid state diffusion and then proceeds till the end of the exothermic reaction. Therefore, as the heating rate increases, the amount of TiAl and Ti<sub>3</sub>Al phases increases too.

Reaction between Ti and Al powders in liquid phase sintering takes place when liquid aluminum is formed leading to the formation of titanium aluminide phases at the interface between contacting particles. Moreover, the main mechanism in the liquid phase sintering that leads to the formation of titanium aluminides is diffusion controlled mechanism. As it was discussed earlier, Gibbs free energy of formation plays magnificent role in specifying which phase forms first among Ti<sub>3</sub>Al, TiAl<sub>3</sub>, TiAl, Ti<sub>2</sub>Al<sub>5</sub> and TiAl<sub>2</sub> that are resulted from exothermic reaction [72].

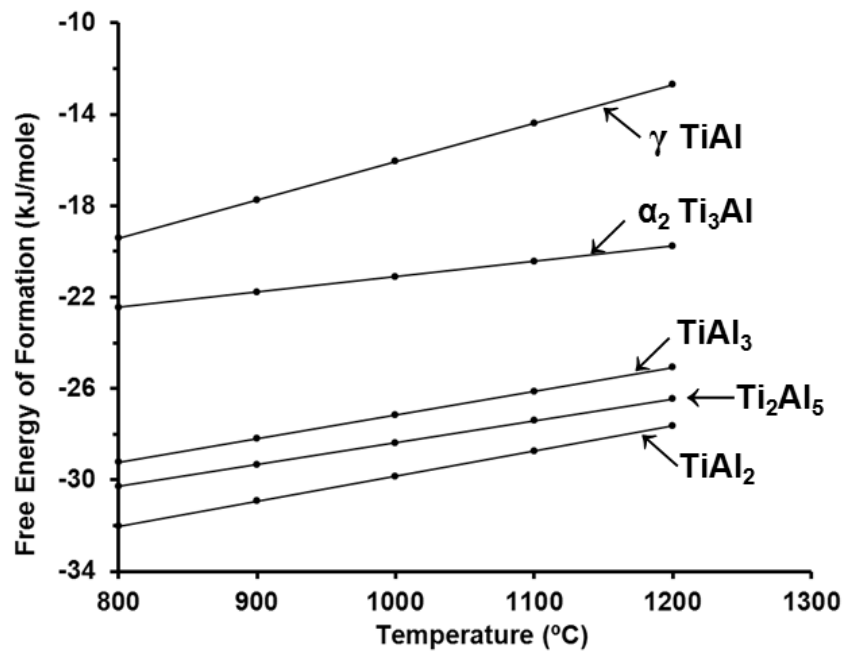


**Figure 3.9** Free energy of formation of Ti-Al intermetallic compounds as a function of temperature.

X-ray diffraction (XRD) patterns of spark plasma sintered samples at four different temperatures are presented in Fig. 3.10. The predominant peak is  $\gamma$ -TiAl phase as shown in Fig. 3.10 (b). Insignificant amount of  $\text{TiAl}_3$  was also observed due to the influence of low sintering temperature. Also, rich titanium aluminide phase  $\alpha_2$ - $\text{Ti}_3\text{Al}$  was observed as the second highest peak. A shorter peak of  $\text{TiAl}_2$  was also observed. On the other hand, samples sintered at 1000 °C showed XRD pattern that is slightly different from the one of 900 °C in which  $\text{TiAl}_3$  peak was disappeared, as shown in figure 3.10 (c). Therefore, the only predominant phase is  $\gamma$ -TiAl phase followed by  $\alpha_2$ - $\text{Ti}_3\text{Al}$  phase. Furthermore, the XRD patterns of other two samples fabricated at temperatures of 1100 °C and 1200 °C shown in Fig. 3.10 (d) and (e) show similar phases having  $\gamma$ -TiAl phase as the predominant peak followed by  $\alpha_2$ - $\text{Ti}_3\text{Al}$  phase. However, it is observed that intensity of  $\alpha_2$ - $\text{Ti}_3\text{Al}$  peak was slightly increased.

Sujata *et al.* [73] reported that  $\text{TiAl}_3$  is the first phase formed during reactive sintering between Ti(s) and Al(l). Sujata *et al.* also confirmed that using elemental powders of Ti and Al leads only to the formation  $\text{TiAl}_3$  phase during liquid phase sintering and they concluded that formation of  $\gamma$ -TiAl and  $\alpha_2$ - $\text{Ti}_3\text{Al}$  phases directly from element powders is difficult. However, in this current work, elemental powders were used during spark plasma sintering process; and as it was shown above,  $\gamma$ -TiAl is the only predominant phase followed by  $\alpha_2$ - $\text{Ti}_3\text{Al}$  phase. Therefore, the effect of high heating rate of 100 °C/min and the findings of Lee *et al.* helped to explain the reason behind the formation of the  $\gamma$ -TiAl and  $\alpha_2$ - $\text{Ti}_3\text{Al}$ .

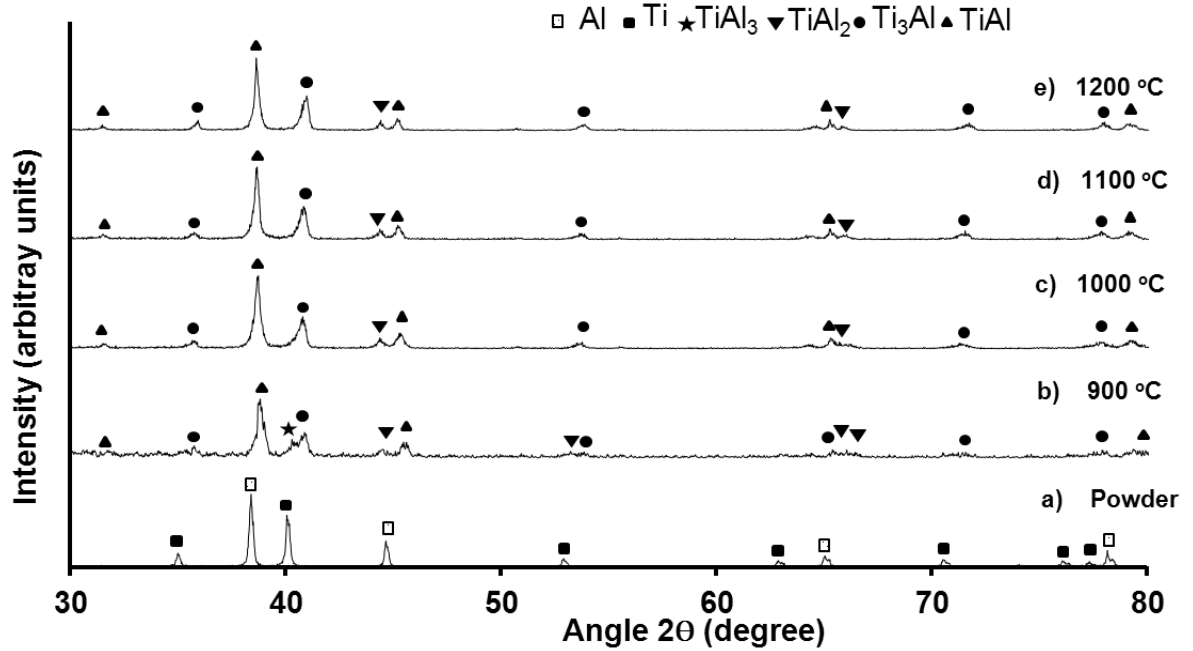


**Fig. 3.10** XRD patterns of a) Ti-Al powder, and spark plasma sintered samples at, b) 900 °C, c) 1000 °C and d) 1100 °C, and b) 1200 °C,

### 3.2.3 Effect of the Sintering Temperature on Evolution of the Microstructure

SEM and EDS micrographs of spark plasma samples sintered at 900 °C are shown in Fig. 3.11. It can be seen that most of the area is occupied by rich aluminum phase ( $\gamma$ -TiAl). Island like shape represents  $\alpha_2$ - $\text{Ti}_3\text{Al}$  phase. Also,  $\text{TiAl}_3$  phase was slightly observed confirming XRD results. EDS micrograph, Fig. 3.11 c and d, presents the areas of aluminum rich (TiAl) and titanium rich ( $\text{Ti}_3\text{Al}$ ) phases. During the liquid phase sintering of Ti-Al powder, it is explained that  $\text{Ti}_3\text{Al}$  phase is formed through the quick growth of  $\text{Ti}_3\text{Al}$  diffusion layer from the remaining titanium particles while the evolution of TiAl phase takes place through the development of  $\text{TiAl}_3$  matrix [74]. Porosity can clearly be observed in the 900 °C micrograph which therefore leads to a decrease in density values.

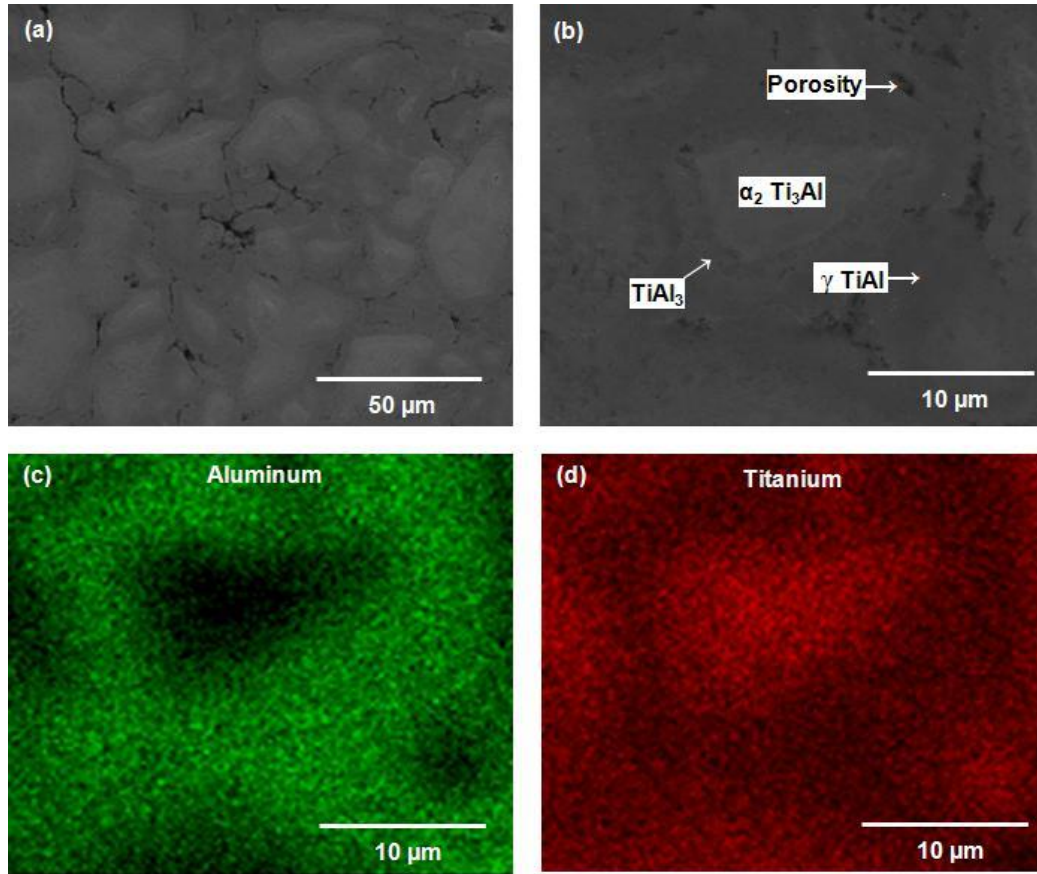


**Fig. 3.11** a) and b) SEM micrograph of 900 °C, c) and d) EDS images of (b).

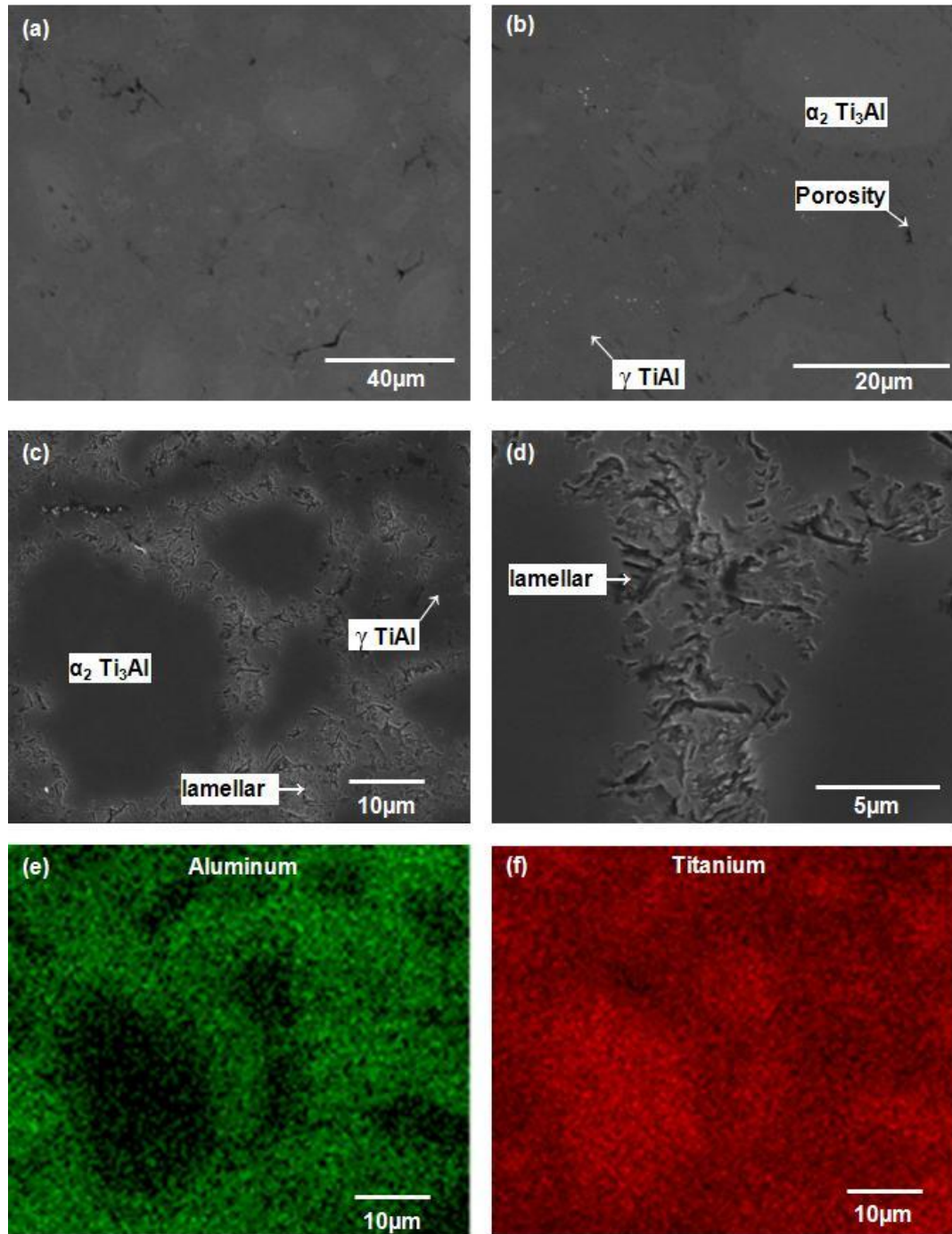
In comparison with samples sintered at 900 °C, sintering at 1000 °C led to a distinct microstructure as shown in Fig. 3.12. SEM micrograph shows that amount of  $\gamma$ -TiAl was increased as well as a significant decrease in porosity was noticed. Also, titanium rich ( $\alpha_2$ -Ti<sub>3</sub>Al) phase was slightly reduced. EDS micrograph, Fig. 3.11(e) and (f), presented an increase in the  $\gamma$ -TiAl phase. Moreover, lamellar phase was evolved from precipitates resulted from interdiffusion between Ti particles and Al in TiAl<sub>3</sub> matrix as the effect of the high heating rate [74]. The lamellar phase is a dual structure of both  $\gamma$ -TiAl and  $\alpha_2$ -Ti<sub>3</sub>Al.

Fig. 3.13 presents SEM and EDS micrographs of samples sintered at 1100 °C. It can be seen that  $\gamma$ -TiAl phase becomes predominant and outweighs Ti<sub>3</sub>Al phase as shown in EDS micrograph. Also, amount of lamellar or dual phase ( $\gamma$ -TiAl and  $\alpha_2$ -Ti<sub>3</sub>Al) was increased. In

contrast to titanium aluminide specimens fabricated at 900 °C and 1000 °C, porosity in sample sintered at 1100 °C was not observed and that explains the reason of getting fully densified samples.

SEM and EDS micrographs of spark plasma sintered samples at 1200 °C are presented in Fig. 3.14. Significant phase evolution was observed in which Gamma TiAl is the only observed phase along with lamellar phase. It seems that the lamellar phase was also reduced leading TiAl to dominate the microstructure. Fully densified microstructure was also observed. EDS micrograph confirmed the absence of titanium rich phase  $\alpha_2$ -Ti<sub>3</sub>Al.





**Fig. 3.12** Sample sintered at 1000 °C a) and b) SEM micrograph, c) and d) SEM micrograph of the etched surface, e) and f) EDS images of (c).

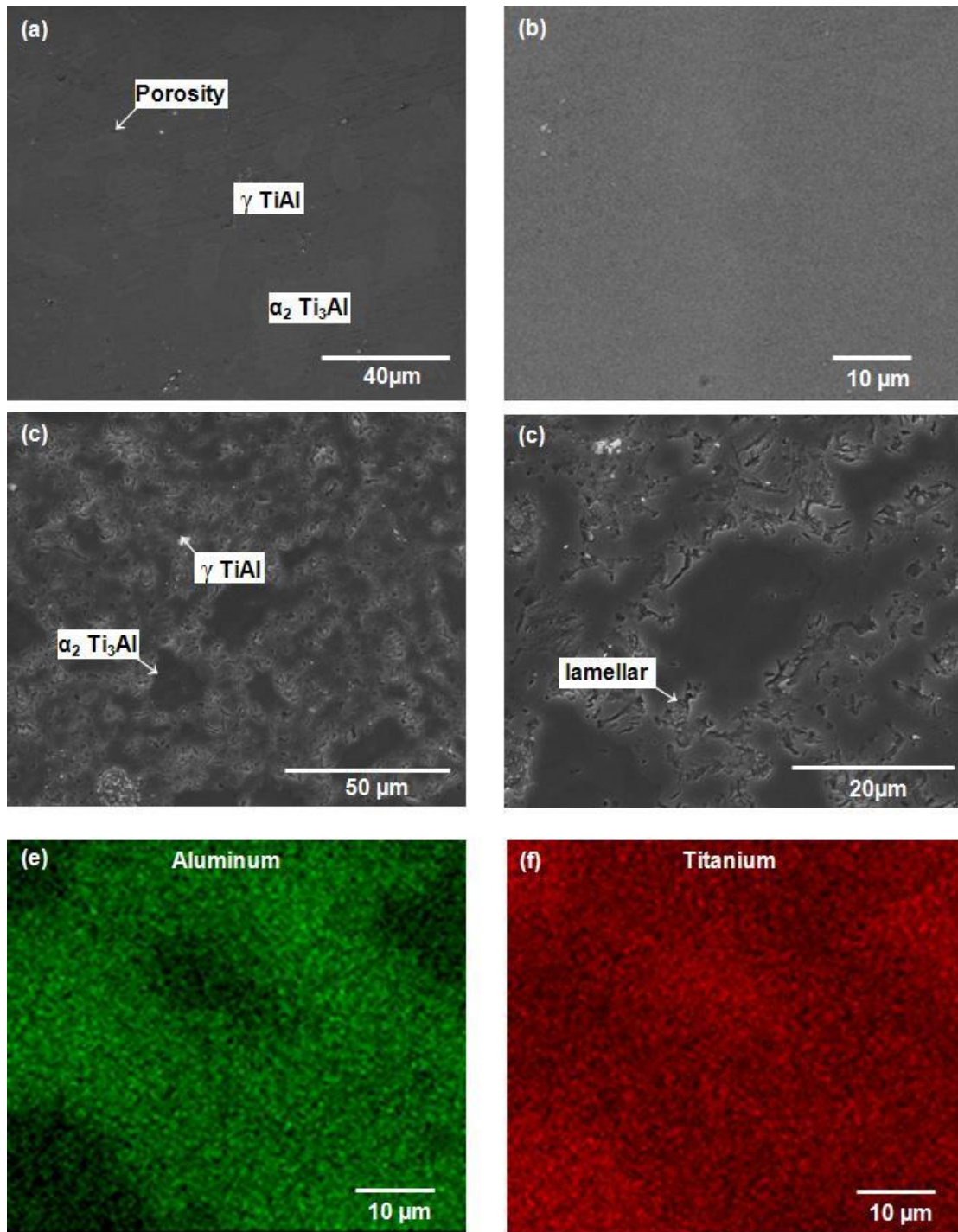


**Fig. 3.13** Sample sintered at 1100 °C a) and b) SEM micrograph, c) and d) SEM micrograph of the etched surface, e) and f) EDS images of (c).

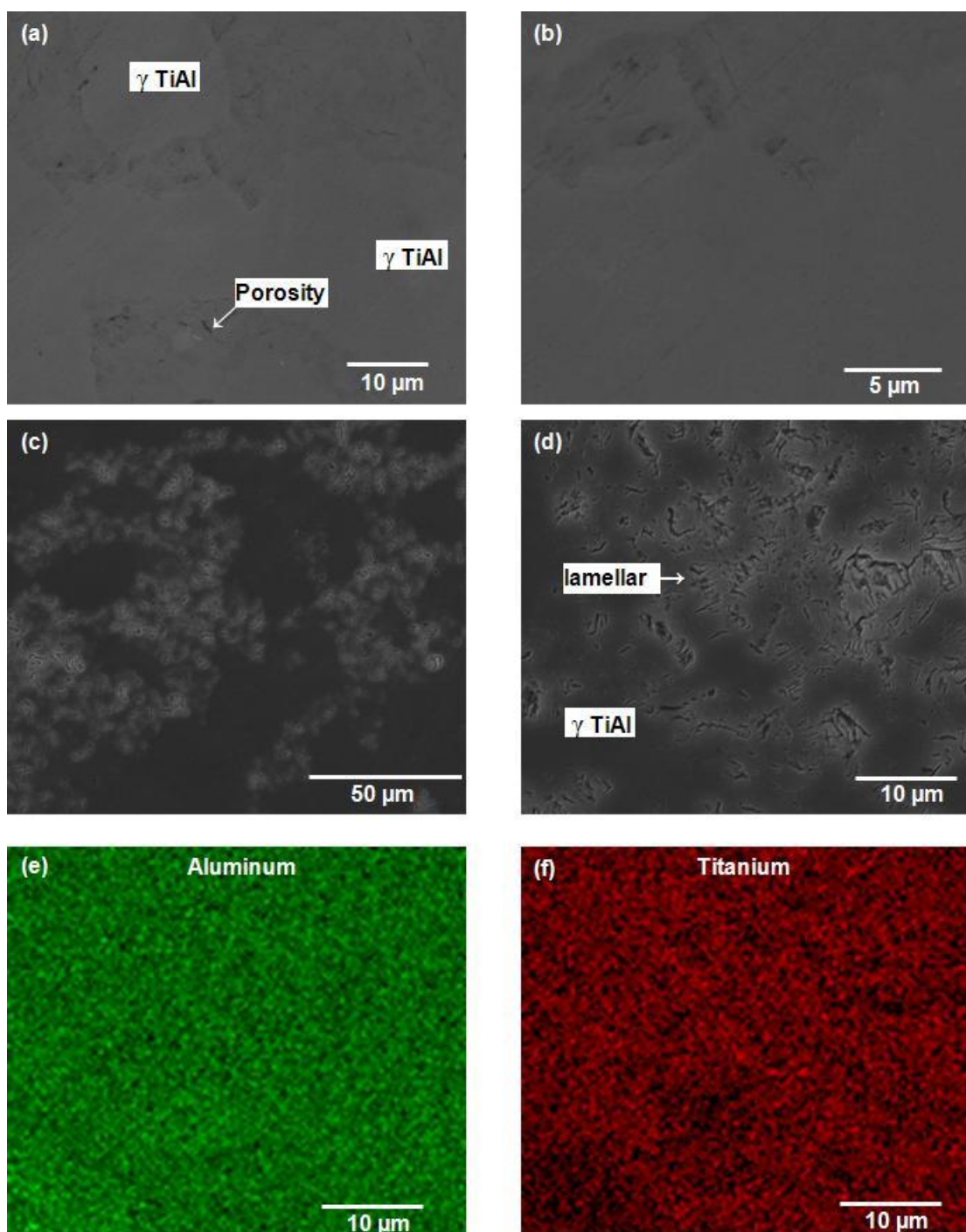


**Fig. 3.14** Sample sintered at 1200 °C a) and b) SEM micrograph, c) and d) SEM micrograph of the etched surface, e) and f) EDS images of (c).

### 3.2.4 Microhardness and Compression Testing Analysis of Titanium Aluminides

Vickers microhardness results were averaged and then reported for all samples fabricated at temperatures ranging from 900 °C-1200 °C, as shown in Fig. 3.15. SPS specimen at 900 °C exhibited an average hardness value of 3.85 GPa. Similarly, samples fabricated at 1000 °C and 1200 °C show the same hardness of the one of 900 °C. A slight decrease in hardness values was observed in samples sintered at 1100 °C.

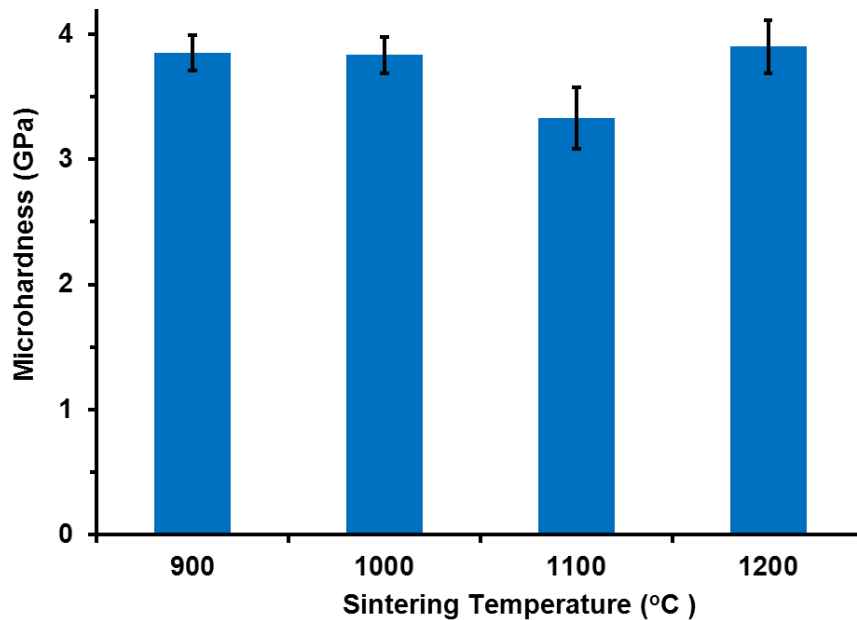


**Fig. 3.15** Microhardness values of titanium aluminide samples sintered at different temperatures.

Although there is a slight difference in hardness values of sample fabricated at 1100 °C, all samples possess hardness values which are in an acceptable range that falls in agreement with reported data. Matsugi *et al.* reported Vickers microhardness results for samples that had the same composition, but they were sintered at higher temperature range (1300 °C - 1400 °C). The range of the Vickers microhardness results of this work is (3.3–3.9 GPa) which is in agreement with that obtained by Matsugi *et al.* (2.8–4.2 GPa). On the other hand, Wang *et al.* [75] fabricated titanium

aluminide samples using hot isostatic pressing (HIP) and subsequent heat treatment. Their observation on the Vickers microhardness values led to that the lamellar phase ( $\gamma$ -TiAl +  $\alpha_2$ -Ti<sub>3</sub>Al) exhibited the highest microhardness values (4.35–4.83 GPa) while  $\gamma$ -TiAl showed the lowest values (2.14–3.14 GPa) and the titanium rich phase  $\alpha_2$ -Ti<sub>3</sub>Al microhardness results were close to the lamellar microhardness values (4.14–4.78 GPa). Therefore, by considering Vickers microhardness values reported by Wang *et al.*, microhardness results of this current work were totally influenced by the presence of lamellar and  $\alpha_2$ -Ti<sub>3</sub>Al phases.

Spark plasma sintered titanium aluminide samples compressive stress-strain curves are presented in Fig. 3.16. Compressive yield strength of samples sintered at 900 °C and 1100 °C was comparable ( $\sigma_{YS, 900}^{\circ C} = 1250$  MPa and  $\sigma_{YS, 1100}^{\circ C} = 1150$  MPa). A decrease in compressive yield strength was observed in 1000 °C ( $\sigma_{YS, 1000}^{\circ C} = 900$  MPa). The lowest value of compressive yield strength was obtained by 1200 °C sample ( $\sigma_{YS, 1200}^{\circ C} = 450$  MPa). All samples which were fabricated over the range (900 °C - 1200 °C) exhibited similar strain behavior. Significant decrease in the strength of 1200 °C sample may be attributed to the grain growth which can be correlated to temperature. Chen *et al.* [76] conducted compression test on samples fabricated using extensive ball milling (12 hrs) and spark plasma sintering technique over a temperature range (800 °C - 1100 °C) with a lower aluminum content (47 at.% Al). The reported compression data showed higher compressive yield strength ranging from 1250 to 1700 MPa. Comparing compressive data of this current work with that of Chen *et al.* explains the influence of ball milling that led to smaller grain size as well as powder composition had less aluminum content. Although yield strength of this work is low, increase in aluminum content (53 at.% Al) led to higher strain.

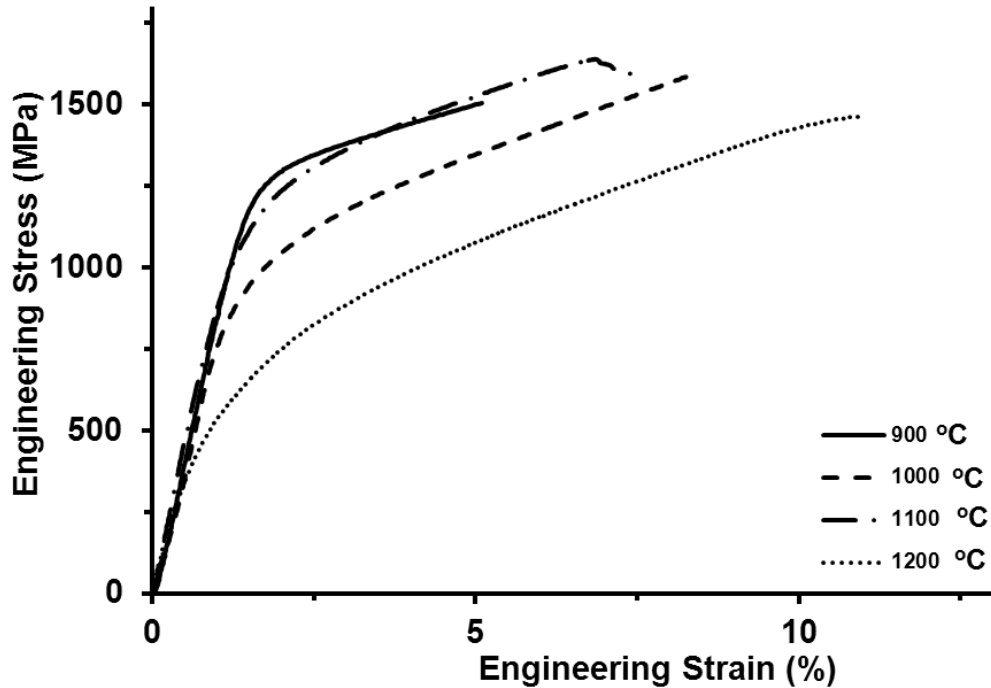


**Fig. 3.16** Compressive stress-strain curves of SPS titanium aluminide compounds.

### 3.2.5 Fractography of the Spark Plasma Sintered Titanium Aluminides

Fracture surfaces were all obtained from tested specimens that underwent compression testing. SEM micrograph of fracture surfaces was done in order to help studying the effect of sintering temperature on fracture behavior of sintered samples. Fig. 3.17 presents fracture surfaces micrograph of all samples sintered over the range 900 °C -1200 °C. It is observed that structure of samples sintered at 900 °C consists of equiaxed  $\gamma$ -TiAl grains (Fig. 3.17 a-b). Also it was clearly observed that grain boundary or intergranular failure was the only fracture mechanism in specimen sintered at 900 °C. However, samples fabricated at 1000 °C have similar crystal structure those samples sintered at 900 °C, yet they presented three different fracture mechanisms: transgranular, intergranular and cleavage (Fig. 3.17 c-d). Also, sintering at 1100 °C leads to structure that consists of both lamellar structure and  $\gamma$ -TiAl grains. Intergranular fracture was also observed as well as cleavage failure in this latter sample (Fig. 3.17 e-f). For samples fabricated at 1200 °C, transgranular, intergranular, and cleavage were the fracture mechanisms (Fig. 3.17 g-h).

As sintering temperature increased from 900 °C to 1200 °C, gradual grain growth was noticed. The grain size of SPS titanium aluminide samples sintered at 900 °C, 1000 °C, 1200 °C and 1200 °C is 1.1µm, 1.3 µm, 3.3 µm and 2.9 µm, respectively. Moreover, grain boundaries of  $\gamma$ -TiAl,  $\text{Ti}_3\text{Al}$  and lamellar interfaces are not strong enough to prevent crack propagation along the grain boundaries as well as along interfaces [77]. Therefore, grain boundaries embrittlement is attributed to the inevitable penetration of oxygen during processing which leads to the formation of undetectable oxides on grain boundaries [78]. Moreover, initial powder defect, larger particle or inclusion, are other factors contributed to fracture failure [79].



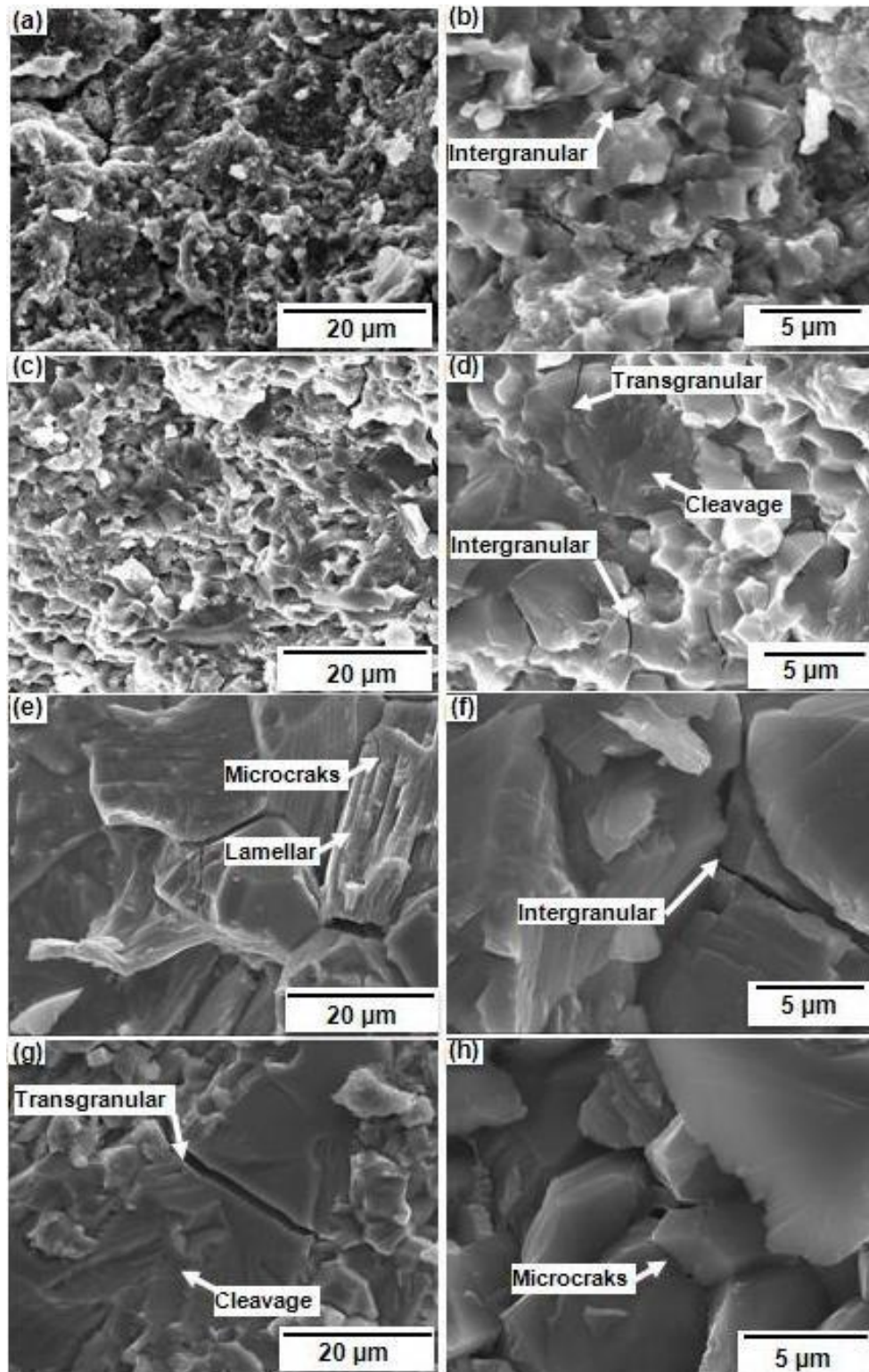


**Fig. 3.17** Fracture surfaces of compressive loading samples sintered at (a) - (b) 900 °C, (c) - (d) 1000 °C, (e) - (f) 1100 °C, and (g) - (h) 1200 °C.



### 3.2.6 Wear Analysis of the Spark Plasma Sintered Titanium Aluminides

The cumulative weight loss as a function of sliding time of sintered titanium aluminide samples measured at each test segment (10 min) is shown in Fig. 3.18. All of the four samples sintered at 900 °C, 1000 °C, 1100 °C and 1200 °C present a similar trend, which means as the sliding time increases, the amount of weight loss increases as well. Sample sintered at 900 °C exhibited a slight increase in cumulative weight loss results whereas other samples fabricated at 1000 °C, 1100 °C and 1200 °C presented similar weight loss results to each other. Moreover, total weight loss was calculated during wear test and then plotted for each sintered sample, as shown in Fig. 3.19. It is observed that sample sintered at 1100 °C exhibited a slight improvement in total weight loss data compared to that of the other three samples fabricated at 900 °C, 1000 °C and 1200 °C. It is reasonable to attribute this improvement in weight loss of the sample fabricated at 1100 °C to higher density value (~100 %).

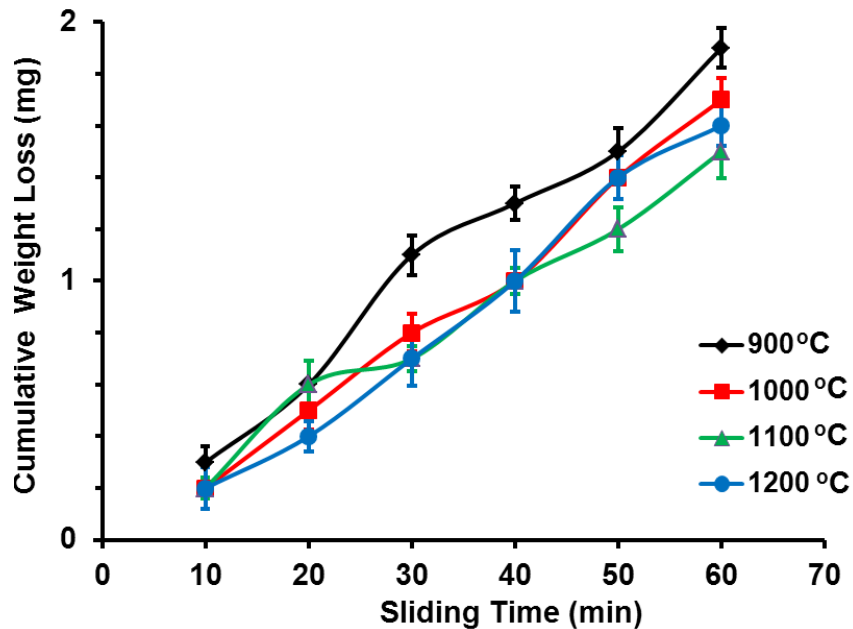


**Fig. 3.18** Cumulative weight loss versus sliding time of spark plasma sintered titanium aluminide samples fabricated at different temperatures.

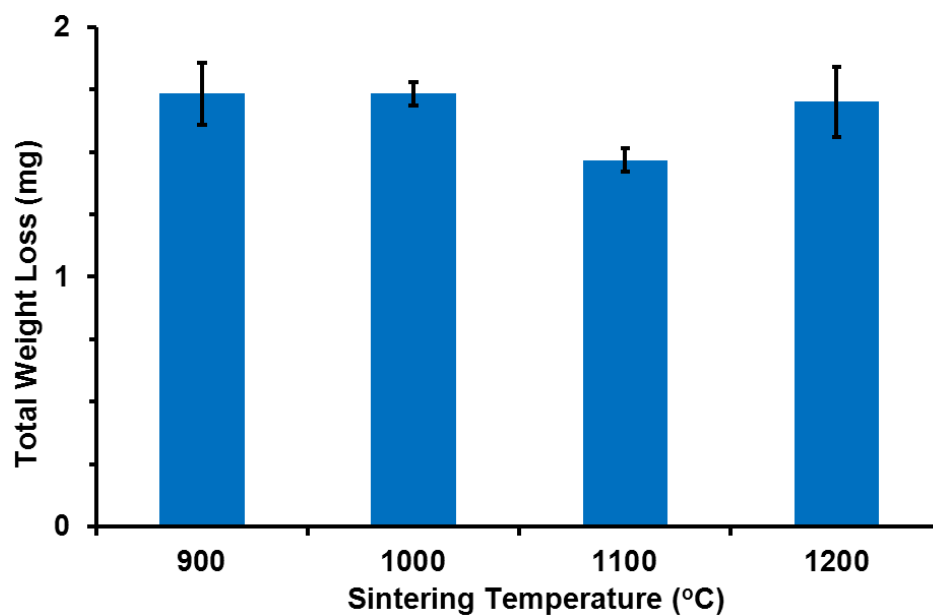


**Fig. 3.19** Total weight loss of spark plasma sintered titanium aluminide samples as function of sintering temperature.

The average coefficient of friction values as a function of sliding time of all spark plasma sintered titanium aluminide samples are presented in Fig. 3.20. The sample sintered at 900 °C exhibited average coefficient of friction values of about  $0.58 \pm 0.04$ . Similarly, samples of 1000 °C and 1200 °C exhibited average values close to that of 900 °C of  $0.6 \pm 0.02$  and  $0.59 \pm 0.02$ , respectively. However, spark plasma sintered titanium aluminide sample fabricated at 1100 °C exhibited a slight improvement on the average coefficient of friction of  $0.53 \pm 0.03$ .

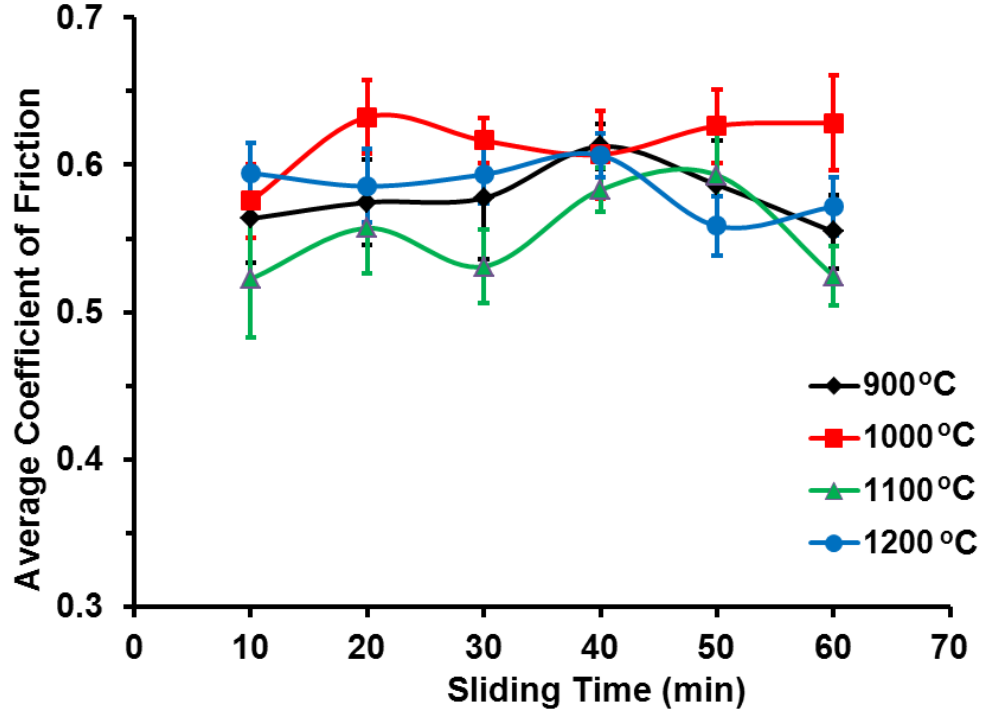


**Fig. 3.20** Average coefficient of friction as a function of sliding time of SPS titanium aluminide samples fabricated at different temperatures.

All the obtained average coefficient of friction values of titanium aluminide samples sintered at different temperatures fall in the range of reported data of samples with similar composition. Chu *et al.* [80] conducted wear tests of titanium aluminide samples having composition ranges from 25 at.% to 53 at.% Al in order to study the effect of Al content on the sliding behavior of the fabricated samples. In their work, the influence of operating speed as well as normal applied load was not noticeable and most of the effect on coefficient of friction values was completely attributed to aluminum content. This indicates that samples fabricated with low aluminum contents (25 at.%) which were tested under different loads presented the lowest coefficient of friction ( $\sim 0.42$ ) whereas high aluminum content samples that underwent the same testing parameters exhibited the highest coefficient of friction values ( $\sim 0.62$ ). Moreover, Chu *et al.* concluded that increasing sliding speed from (0.236 m/s) to (0.628 m/s) led to a significant

decrease in the coefficient of friction values for the low aluminum content samples while samples with high aluminum content retain the same coefficient of friction value at all different speeds. Therefore, the effect of high aluminum content ( $> 50$  at.%) on the wear behavior of titanium aluminide compounds was explained by the formation  $\gamma$ -TiAl intermetallic phase to be the predominant or single phase which is characterized by low hardness as well as poor ductility leading to high coefficient of friction. Also, low aluminum content ( $\sim 25$  at.%) samples are characterized by the formation of  $\alpha_2$ -Ti<sub>3</sub>Al phase or lamellar phase ( $\gamma$ -TiAl and  $\alpha_2$ -Ti<sub>3</sub>Al) which has more ductility and higher hardness leading to low values of coefficient of friction. Comparing the obtained wear analysis of this current work's samples fabricated by SPS with that reported by Chu *et al.* and relating the effect of the phase formation on the sliding behavior led to confirmation that formation of  $\gamma$ -TiAl plays a significant role on tribological behavior of the sintered samples. The predominance of  $\gamma$ -TiAl phase in all the fabricated samples is reason behind the high coefficient of friction values. Chu *et al.* discussed the wear mechanism in both low and high aluminum content titanium aluminide which can be attributed to three causes relating sliding friction between the surface of sintered sample and the counterface ball: adhesion, ploughing and asperity deformation. Therefore, the wear of low aluminum content samples was caused by ploughing and adhesion. On the other hand, high aluminum content samples' wear was attributed to asperity deformation.

The depth and width profiles across the worn surface of all sintered samples in temperature range of 900 °C-1200 °C are presented in Fig. 3.21. Comparing all the four curves together, it can be seen that samples sintered at 900 °C and 1200 °C exhibited higher depth whereas sample sintered at 1000 °C was slightly improved. However, the least effect in terms of small track depth and width was observed in samples sintered at 1100 °C. Surface profile across the wear tracks of samples sintered at different temperatures is presented in Fig. 3.22. Sample sintered at 1100 °C show the least wear track width leading to an agreement with weight loss data and having the best wear properties compared with others.

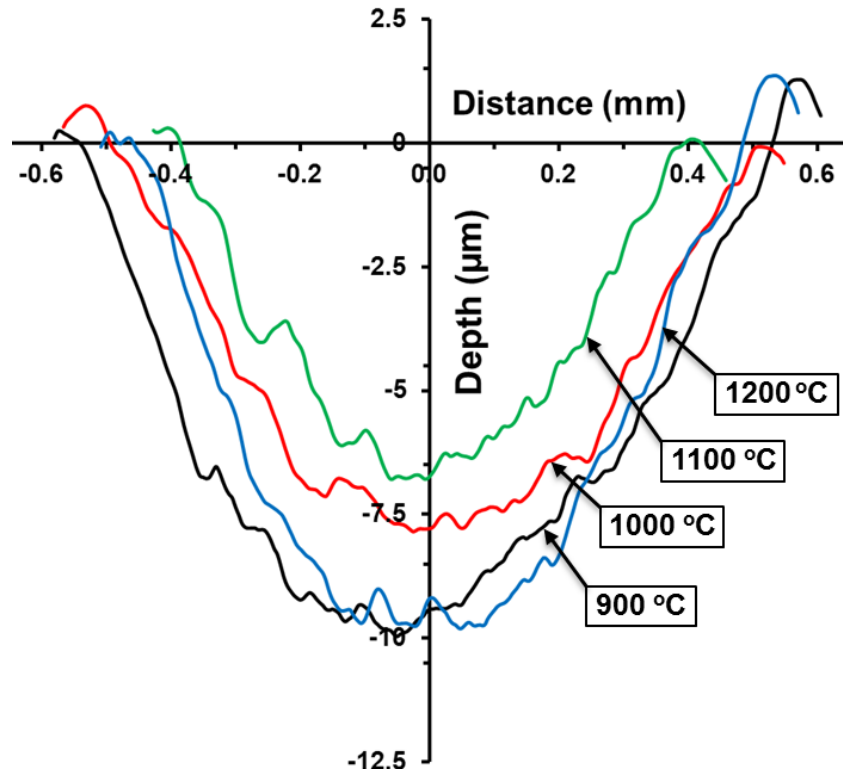


**Fig. 3.21** Line profiles across the wear track of SPS samples at different temperatures.

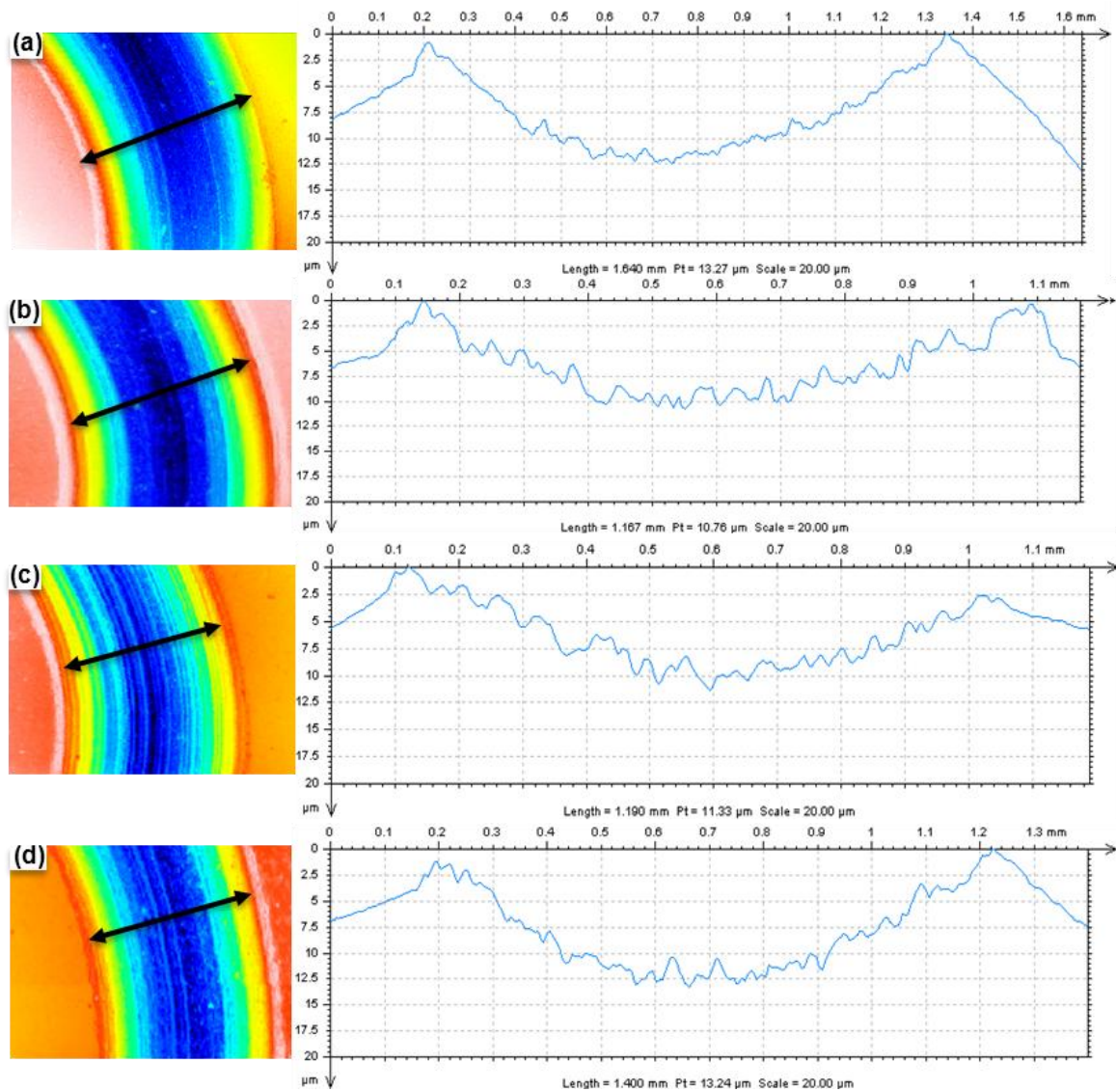
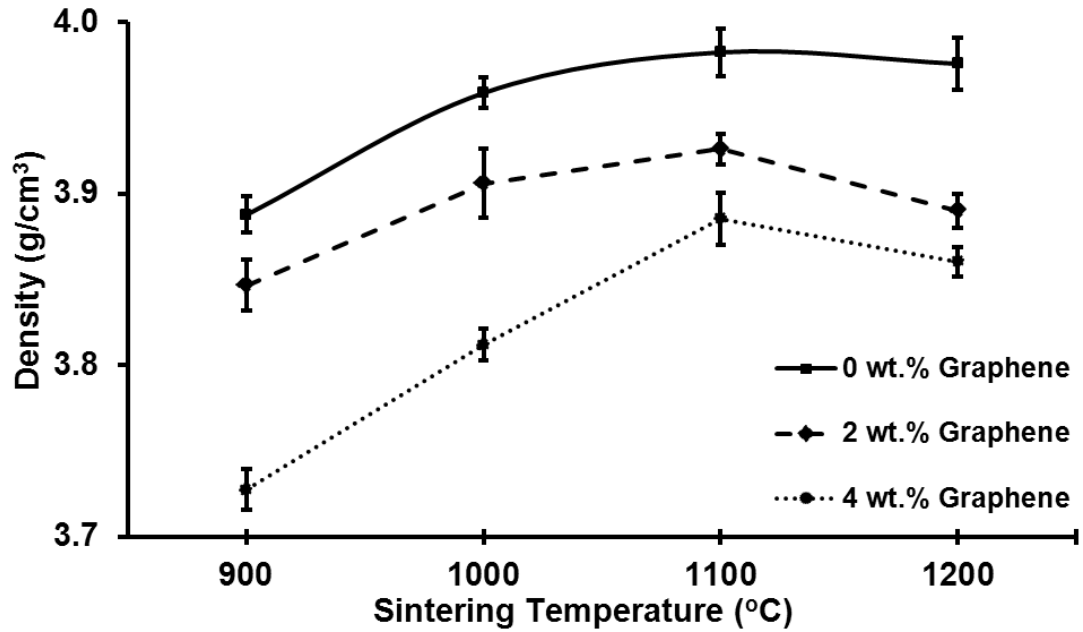


**Fig. 3.22** Surface profiles of wear tracks of SPS titanium aluminides fabricated at (a) 900 °C, (b) 1000 °C, (c) 1100 °C, and (d) 1200 °C..

### **3.3 Spark Plasma Sintering of Graphene reinforced Titanium Aluminides composites**

#### **3.3.1 Effect of the Sintering Temperature on Density**

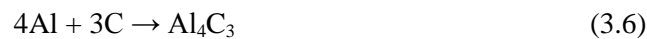
Density of the spark plasma sintered titanium aluminide composites (0%, 2% and 4 wt.% graphene) fabricated at four different sintering temperatures is shown in Fig. 3.23. In comparison with samples sintered without graphene, a significant decrease in density values was clearly observed as the weight percentage of graphene increases. Moreover, the density curves of samples fabricated with 2 wt.% and 4 wt.% graphene show similar behavior to that of titanium aluminide samples (0 wt.% graphene). Samples sintered at 900 °C exhibits the lowest density values as well as sintering at 1100 °C leads to the highest density values in both 2 wt.% and 4 wt.% graphene. Even though density values showed a gradual increase as sintering temperature increases up to 1100 °C, density values cannot be correlated to sintering temperature because as the sintering temperature approaches 1200 °C a noticeable decrease in density was observed for both 2 wt.% and 4 wt.% samples. Generally, the decrease in density values is attributed to the presence of graphene which led to density values lower than that of titanium aluminides. It is also presumable to attribute the decrease in density values of titanium aluminide composite samples to the presence of unreacted graphene. This decrease in density can be also explained as unknown phase transformation at higher temperatures resulted from *in-situ* reactions.



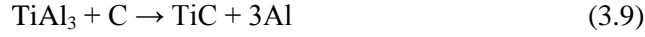
**Fig. 3.23** Density of SPS titanium aluminide composite samples at different sintering temperatures.

### 3.3.2 Effect of the Sintering Temperature on Ti-Al Composites Phases Formation

Fig. 3.24 presents XRD patterns of SPS titanium aluminide composites that were fabricated with 2 wt.% graphene over a temperature range of 900 °C -1200 °C. Generally in Ti-Al-C system, two carbide phases,  $\text{Al}_4\text{C}_3$  and TiC, are common to form.  $\text{Al}_4\text{C}_3$  is formed as a result of a reaction between molten Al and solid carbon as shown in equation 3.6. The other carbide phase TiC can be formed through a direct reaction of liquid titanium with carbon as in equation 3.7. Also, further reaction of TiC with molten aluminum leads to  $\text{Al}_4\text{C}_3$ , and reaction between carbon and the first intermetallic titanium aluminide phase  $\text{TiAl}_3$  results in the formation of TiC as in equations 3.8 and 3.9, respectively [81].







In this current work no carbide phases were formed as a result of the exothermic reaction caused by the liquid aluminum. Therefore, low graphene content (2 wt.% and 4 wt.%) used in the powder is a reasonable reason for absence of carbide phases. Yang *et al.* [82] reported that if carbon to titanium ratio is less than  $\text{Ti}:\text{C} = 1:2$ , it is difficult for carbide phases to be formed. Also, inadequate milling of the Ti-Al-graphene powder during ball milling (< 15 min) contributes in the absence of carbide phases [83]. Furthermore, the only distinctive observation of XRD patterns of titanium aluminides composites was presence of carbon peak confirming what was explained before of unreacted carbon. Although undesirable carbide phases did not form, the presence of carbon in the microstructure led to the decrease observed in the density values. Furthermore, titanium aluminide composites (2 wt.% graphene) fabricated at different temperatures presented similar XRD patterns to that of titanium aluminides (0 wt.% graphene). It can be seen that  $\gamma$ -TiAl intermetallic phase is the predominant phase in all samples which is also followed by the rich titanium phase  $\alpha_2$ -Ti<sub>3</sub>Al. These two main phases are also accompanied with fractions of other intermetallic phases, TiAl<sub>3</sub> and TiAl<sub>2</sub>. Fig. 3.25 presents XRD patterns of samples sintered with 4 wt.% graphene at different temperatures. With regards to the formation of carbides (Al<sub>4</sub>C<sub>3</sub> and TiC), similar observation to the previous titanium aluminide composite samples (2 wt.% graphene) was found. There was no formation of any carbide phases in titanium aluminide composite samples (4 wt.% graphene). Also,  $\gamma$ -TiAl remains the predominant phase. It is observed that amount of TiAl<sub>3</sub> phase slightly increases as the sintering temperature increases.

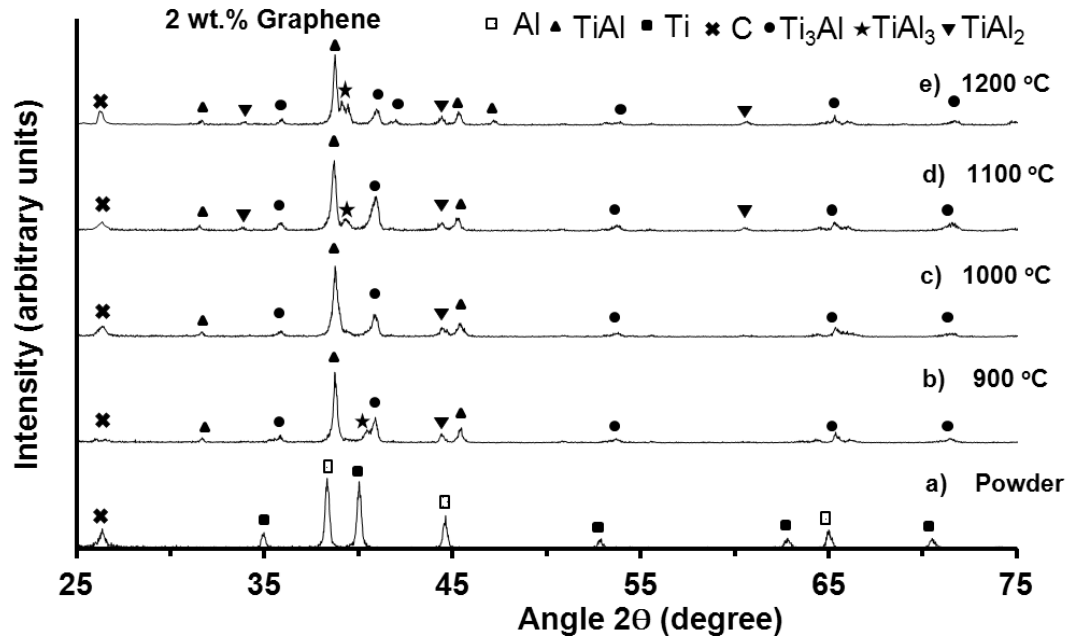


**Fig. 3.24** XRD patterns of a) Ti-Al-graphene powder, and titanium aluminide composites (2 wt.% graphene) samples sintered at, b) 900 °C, c) 1000 °C, d) 1100 °C, and e) 1200 °C.

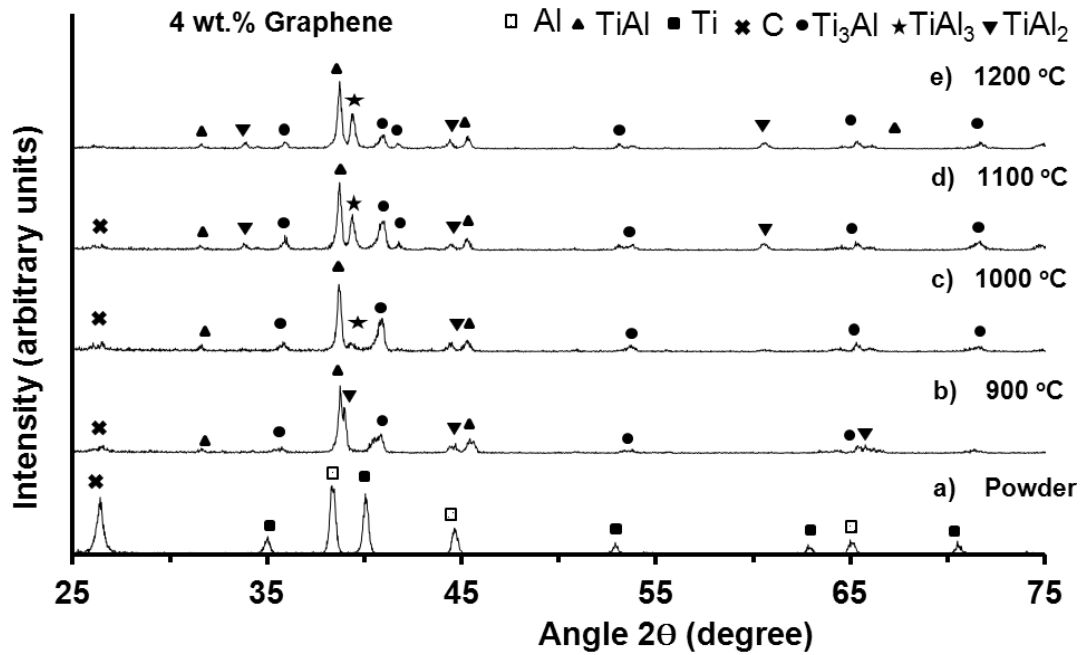


**Fig. 3.25** XRD patterns of a) Ti-Al-graphene powder, and titanium aluminide composites (4 wt.% graphene) samples sintered at, b) 900 °C, c) 1000 °C, d) 1100 °C, and e) 1200 °C.

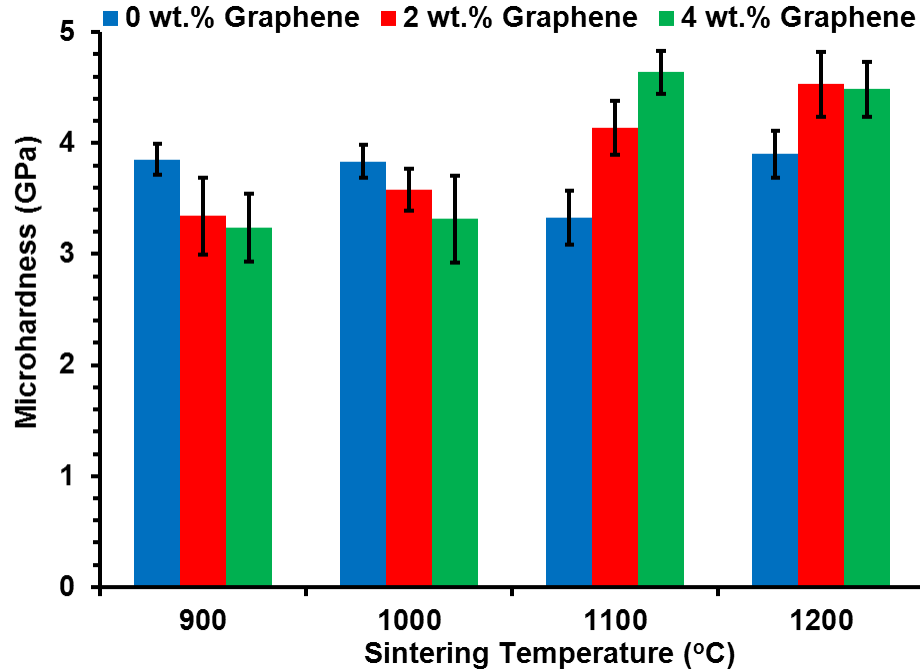
XRD patterns of titanium aluminide composites sintered at different temperatures with different graphene contents showed that  $\gamma$ -TiAl phase is the predominant phase. Along with it, a significant amount of  $\alpha_2$ -Ti<sub>3</sub>Al phase was also observed in samples sintered without graphene. Also for samples sintered with graphene, XRD peak of  $\alpha_2$ -Ti<sub>3</sub>Al phase was slightly decreased. Therefore, the ratio of TiAl phase to Ti<sub>3</sub>Al phase for all samples sintered at different temperatures is calculated from the XRD data (intensity) of each phase as shown in Table 3.1. It is observed that in samples fabricated without graphene, the TiAl to Ti<sub>3</sub>Al ratio decreased as the sintering temperature increased. This indicates that the amount of  $\alpha_2$ -Ti<sub>3</sub>Al phase increased. Thus, this increase of  $\alpha_2$ -Ti<sub>3</sub>Al is attributed to the increase of the lamellar phase ( $\gamma$ -TiAl+  $\alpha_2$ -Ti<sub>3</sub>Al) as the sintering temperature increased. The microstructure of sample sintered at 1200 °C presented only  $\gamma$ -TiAl phase and the lamellar phase. For samples sintered with 2 wt.% graphene, TiAl to Ti<sub>3</sub>Al ratio increased compared to that of 0 wt.% graphene due to the increase of TiAl<sub>3</sub> phase. Similarly, samples fabricated with 4 wt.% graphene exhibited relatively higher TiAl to Ti<sub>3</sub>Al Ti<sub>3</sub>Al phase ratio particularly at 1200 °C due to the increase of TiAl<sub>3</sub> phase and the absence of the lamellar phase as well. Also, it is presumable to attribute the presence of TiAl<sub>3</sub> phase to incomplete reaction between solid titanium and liquid aluminum caused by graphene. Subsequent heat treatment of the samples fabricated with graphene helps to produce more stabilized microstructures through further interdiffusion between TiAl<sub>3</sub> and  $\alpha_2$ -Ti<sub>3</sub>Al to form lamellar phase.

**Table 3** XRD TiAl toTi<sub>3</sub>Al ratio of titanium aluminide composites at different temperatures.

<b>GNPs wt.%</b> <b>Temperature</b>	<b>0 wt.%</b>	<b>2 wt.%</b>	<b>4 wt.%</b>
<b>900 °C</b>	2.48	3.18	3.46
<b>1000 °C</b>	2.26	3.1	2.1
<b>1100 °C</b>	2.18	2.41	2.3
<b>1200 °C</b>	1.82	4.66	4.8

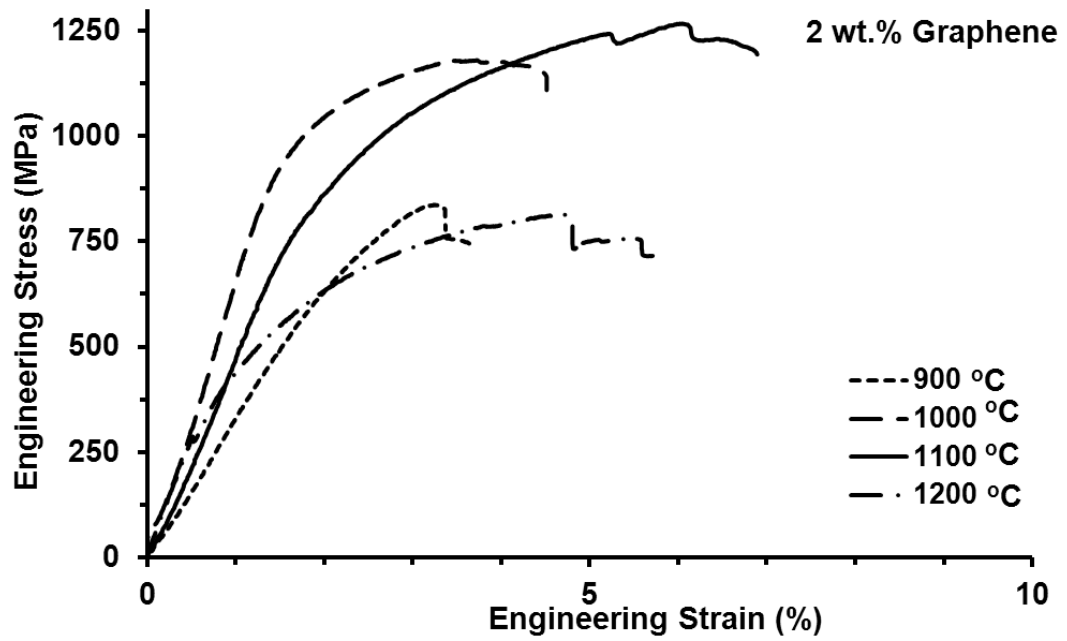
### 3.3.3 Microhardness and Compression testing Analysis

Vickers microhardness data of SPS samples processed with 2 wt.% and 4 wt.% graphene at different temperatures (900 °C, 1000 °C, 1100 °C and 1200 °C) are shown in Fig. 3.26. As it was discussed earlier for the 0 wt.% graphene samples, sintering temperature didn't influence microhardness values. However, for samples fabricated at 900 °C and 1000 °C, a decreasing trend in microhardness values as graphene content increases from 0 wt.% to 4 wt.% was observed. This reduction in microhardness can be attributed to the decrease in the density values of corresponding samples. On the other hand, as the graphene weight percentage increases from 0% to 4%, an increase in Vickers microhardness values was observed in samples sintered at temperatures 1100 °C and 1200 °C. Although gradual decrease in density values of titanium aluminide composite samples (2 and 4 wt.% graphene) was noticed in all samples sintered at (900 °C, 1000 °C, 1100 °C and 1200 °C) compared to that of titanium aluminides (0 wt.% graphene), the contribution of this effect on decreasing microhardness values of titanium aluminide composite samples sintered at 1100 °C and 1200 °C was not noticed. Also, it is known that grain growth is correlated with the increase in temperature. Moreover, Hall-Pitch relationship explains that the increase in grain size leads to a decrease in strength. Thus, with considering grain growth effect on strength, a better interpretation of the increased microhardness values observed in specimens sintered at 1100 °C and 1200 °C is the limited grain growth. Therefore, microhardness analysis can be related to the dual influence of sintering temperature and addition of graphene in temperatures over 1100 °C. Graphene plays a crucial role in restricting grain growth in samples fabricated at 1100 °C, and 1200 °C because it is believed that at high at temperature > 1000 °C carbon starts working as grain refinement agent [84].

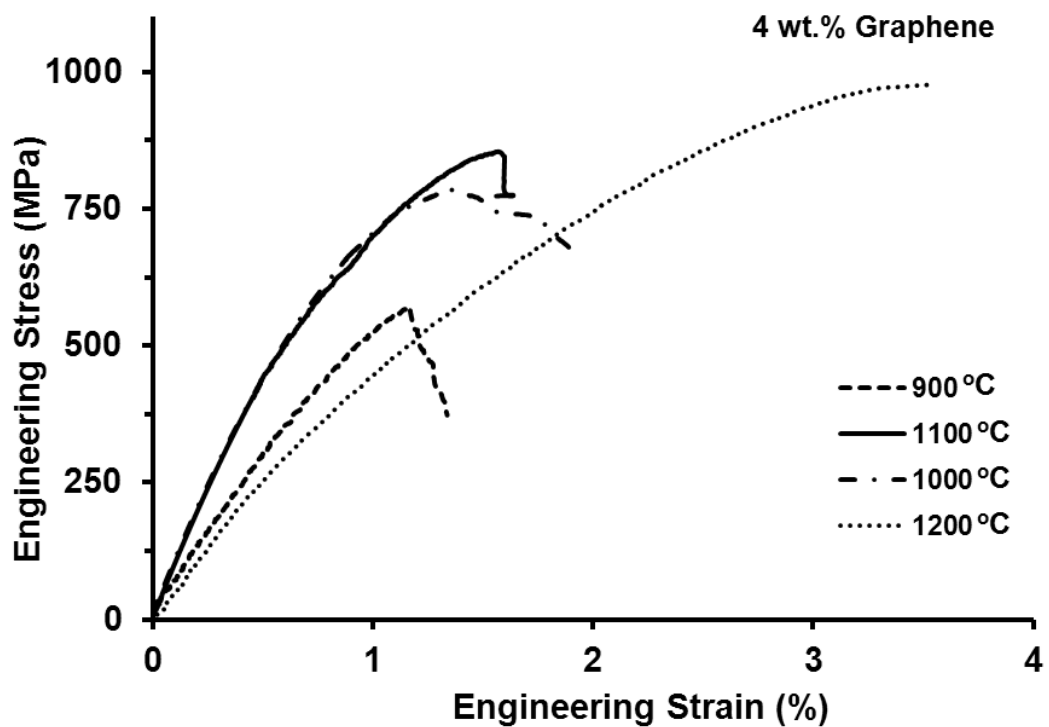


**Fig. 3.26** Vickers's microhardness of SPS titanium aluminide composites (0, 2 and 4 wt.% graphene) fabricated at different temperatures.

The representative compressive stress-strain curves of SPS titanium aluminide composites containing 2 wt.% graphene are presented in Fig. 3.27. Titanium aluminide composite samples (2 wt.% graphene) exhibited a noticeable decrease in compressive yield strength compared to titanium aluminide samples (0 wt.% graphene). Therefore, decrease in both compressive strength and strain values is presumably caused by partial dispersion of graphene in titanium aluminide matrix. It is also reasonable to attribute decrease in strength to the decrease in density values of titanium aluminide composites. Also, among all titanium aluminide composite samples with 2 wt.% graphene, samples sintered at 900 °C and 1100 °C present the highest compressive yield strength values. In addition, further increase in graphene content to 4 wt.% resulted in more decrease in strength, as shown in Fig. 3.28.



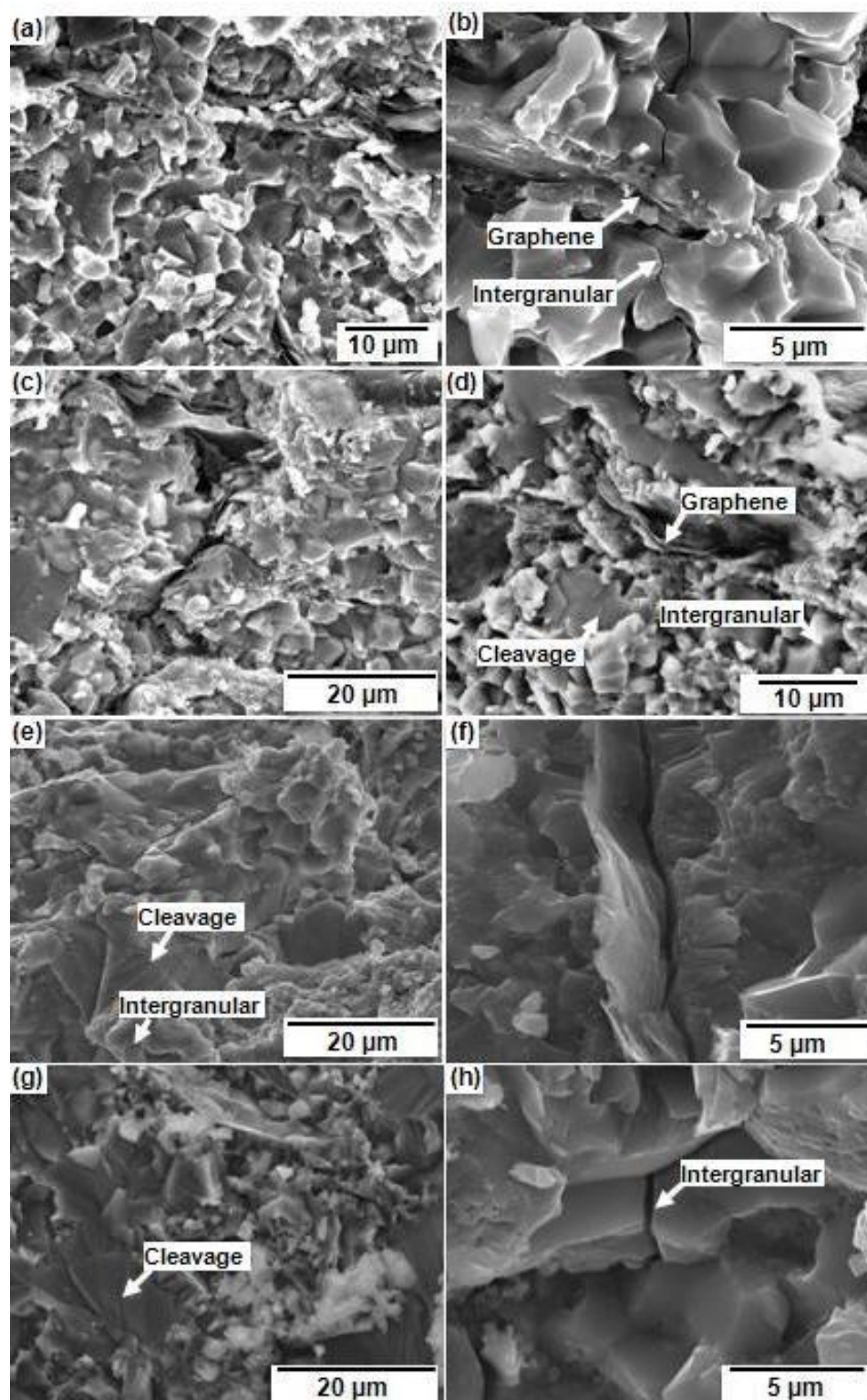
**Fig. 3.27** Compressive stress-strain curves of SPS titanium aluminide composites (2 wt.% graphene) fabricated at different temperatures.



**Fig. 3.28** Compressive stress-strain curves of SPS titanium aluminide composites (4 wt.% graphene) fabricated at different temperatures.

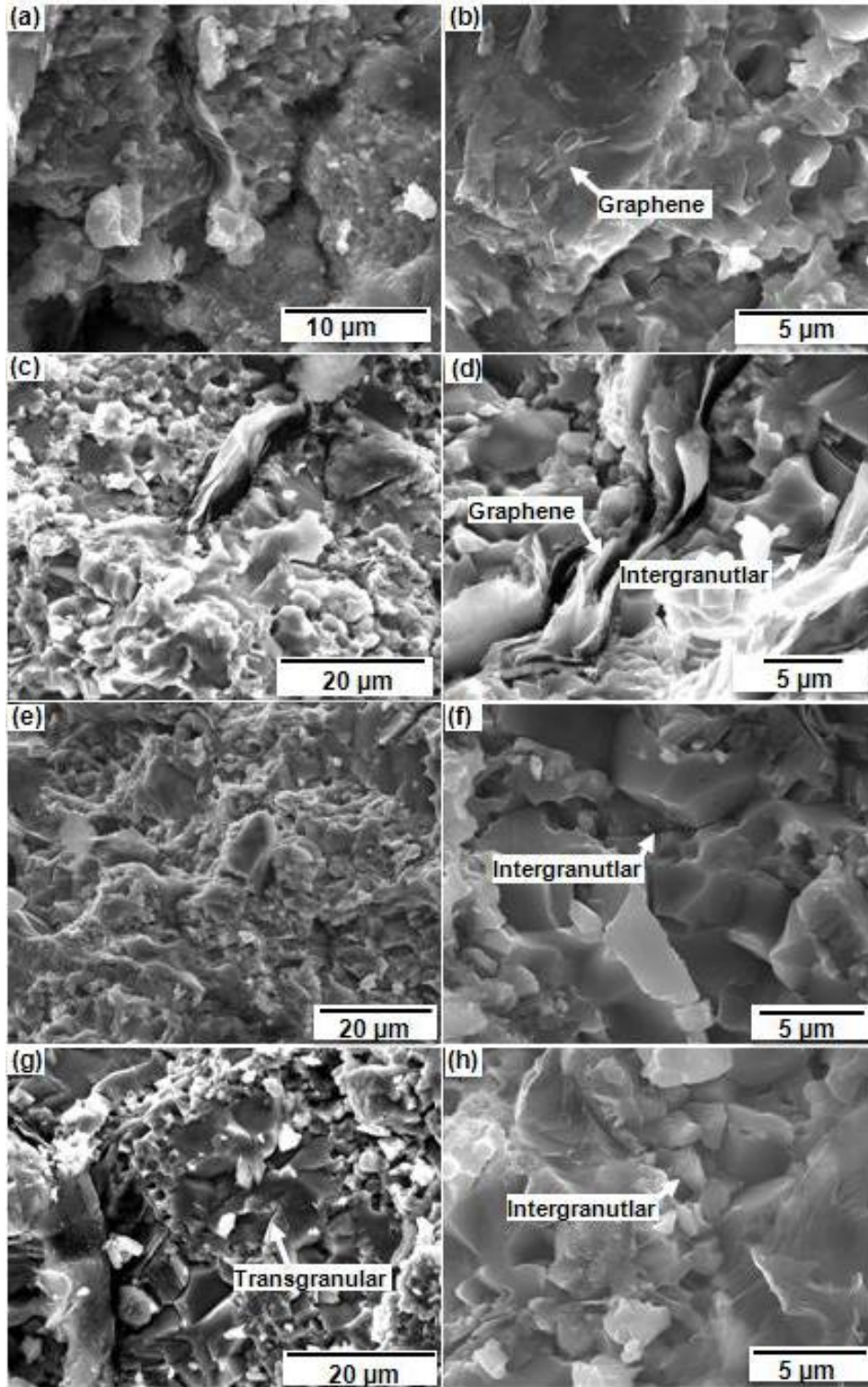
### 3.3.4 Fractography of Spark Plasma Sintered Titanium Aluminide Composites

Fig. 3.29 presents SEM micrographs of fracture surfaces of titanium aluminide composites samples (2 wt.% graphene) that underwent compressive loading. It is observed that samples sintered at 900 °C (Fig. 3.29 a-b) show only intergranular (grain boundary) fracture mode. On the other hand, samples fabricated at 1000 °C, 1100 and 1200 °C exhibit both intergranular and cleavage fracture modes. Unlike titanium aluminide samples (0 wt.% graphene), transgranular fracture mode was not observed in the titanium aluminide composite samples (2 wt.% graphene). Fracture surfaces of spark plasma samples sintered with 4 wt.% graphene are shown in Fig. 3.30. It can be seen that titanium aluminide composites specimens exhibited intergranular failure in all samples fabricated over the range 900 °C -1200 °C. In addition, along with intergranular fracture mode, transgranular failure was also observed in the sample sintered at 1200 °C (Fig. 3.30 g-h). It is observed that the grain size of titanium aluminide composites sintered at different temperatures was influenced by the presence of graphene. The grain size of titanium aluminide samples (0 wt.% graphene) fabricated at 900 °C and 1000 °C increased from (1.1 µm; 1.3 µm) to (1.65 µm; 1.9 µm) and (1.55 µm; 1.6 µm) for 2 and 4 wt.% graphene, respectively. On the other hand, the grain size of samples sintered at 1100 °C and 1200 °C decreased from (3.3 µm; 2.9 µm) to (2.6 µm; 2.3 µm) and (2.2 µm; 1.85 µm) for 2 and 4 wt.% graphene, respectively.



**Fig. 3.29** Fracture surfaces of compressive loading samples (2 wt.% graphene) sintered at (a) - (b) 900 °C, (c) - (d) 1000 °C, (e) - (f) 1100 °C, and (g) - (h) 1200 °C.

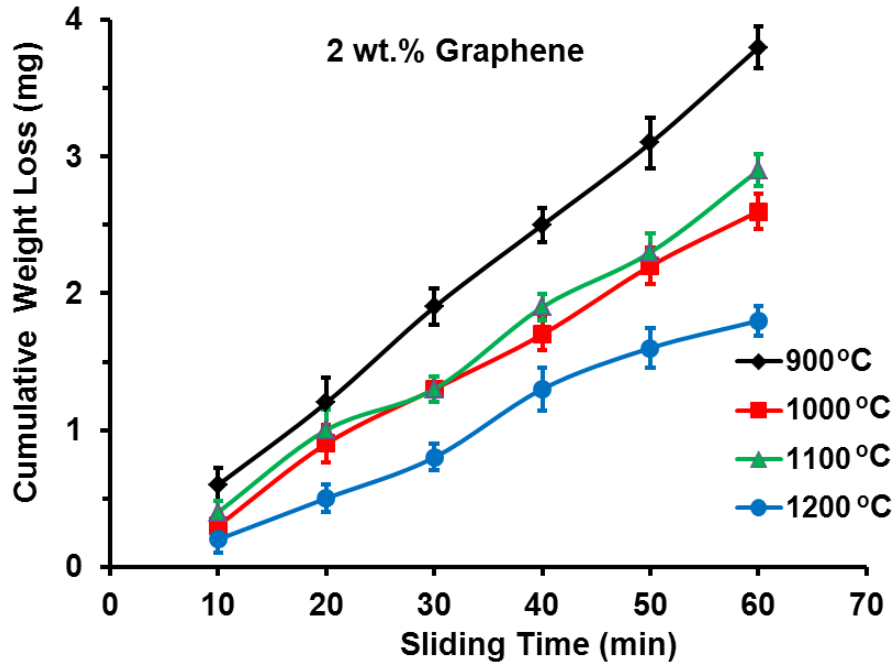




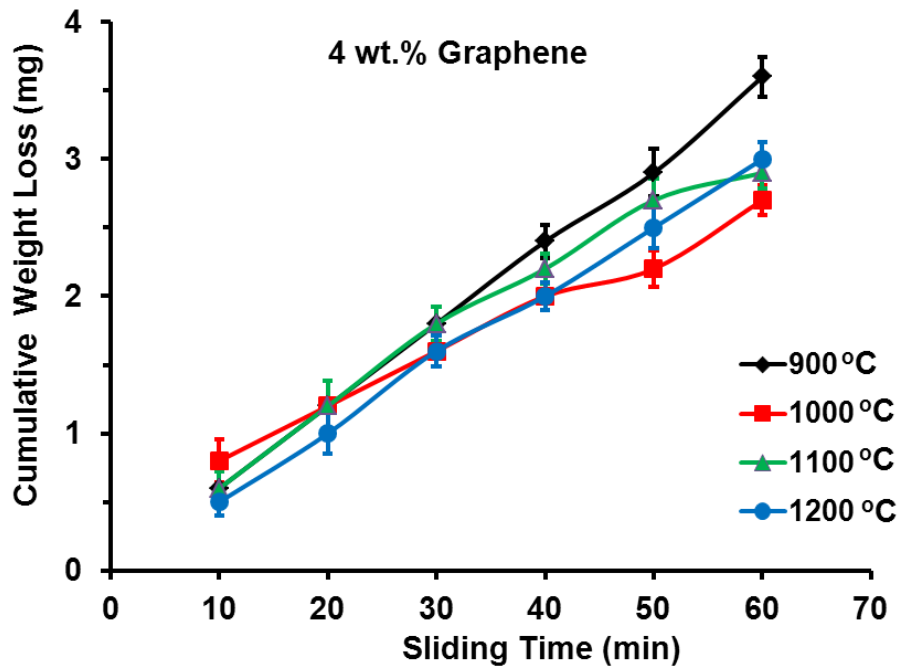
**Fig. 3.30** Fracture surfaces of compressive loading samples (4 wt.% graphene) sintered at (a) - (b) 900 °C, (c) - (d) 1000 °C, (e) - (f) 1100 °C, and (g) - (h) 1200 °C.

### 3.3.5 Wear analysis of Titanium Aluminide Composites

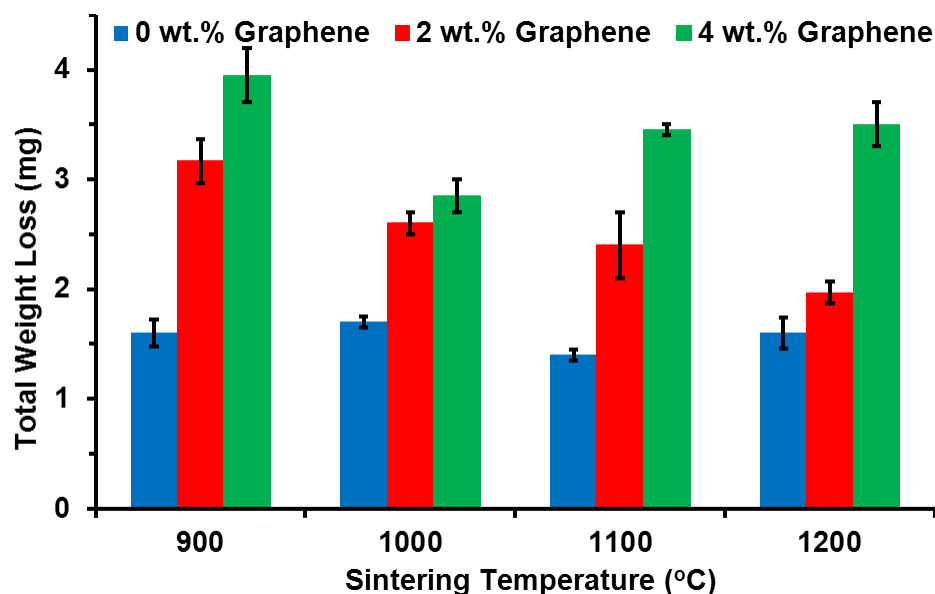
Fig. 3.31 presents the cumulative weight loss of titanium aluminide composite samples (2 wt.% graphene) sintered at different temperatures. Comparing weight loss data of titanium aluminide composite samples (2 wt.% graphene) with that of titanium aluminide samples (0 wt.% graphene), a noticeable change in the cumulative weight loss data was observed. It can be seen that addition of graphene led to an increase in the amount of lost material during the wear test. However, sintering temperature plays a crucial role in reducing weight loss among 2 wt.% graphene samples. As the sintering temperature increases from 900 °C to 1200 °C, significant decrease in the cumulative weight loss was observed. Moreover, increasing graphene content to 4 wt.% resulted in a similar increasing trend of weight loss as shown in Fig. 3.32. Moreover, the influence of sintering temperature was not noticed; for example, samples having 4 wt.% graphene exhibit similar weight loss behavior. Total weight loss was also reported as a function of sliding time for all titanium aluminide composite samples (2 and 4 wt.% graphene) fabricated at different temperatures as shown in Fig. 3.33. Also, it can be seen that increase in graphene content from (0, 2, and 4 wt.%) leads to a gradual increase in the total weight loss results. Therefore, it is presumable to relate the increase in weight loss of titanium aluminide composites (2 and 4 wt.% graphene) to their corresponding decrease in density and vice versa.



**Fig. 3.31** Cumulative weight loss as a function of sliding time of SPS titanium aluminide composites samples (2 wt.% graphene) fabricated at different temperatures.



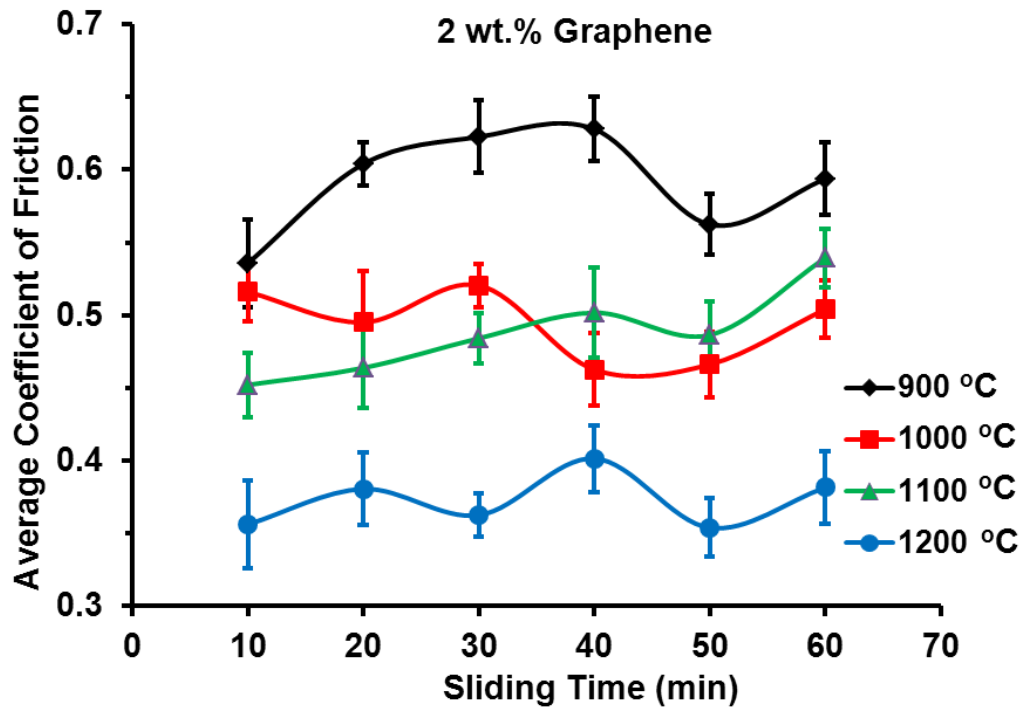
**Fig. 3.32** Cumulative weight loss as a function of sliding time of SPS titanium aluminide composites samples (4 wt.% graphene) fabricated at different temperatures.



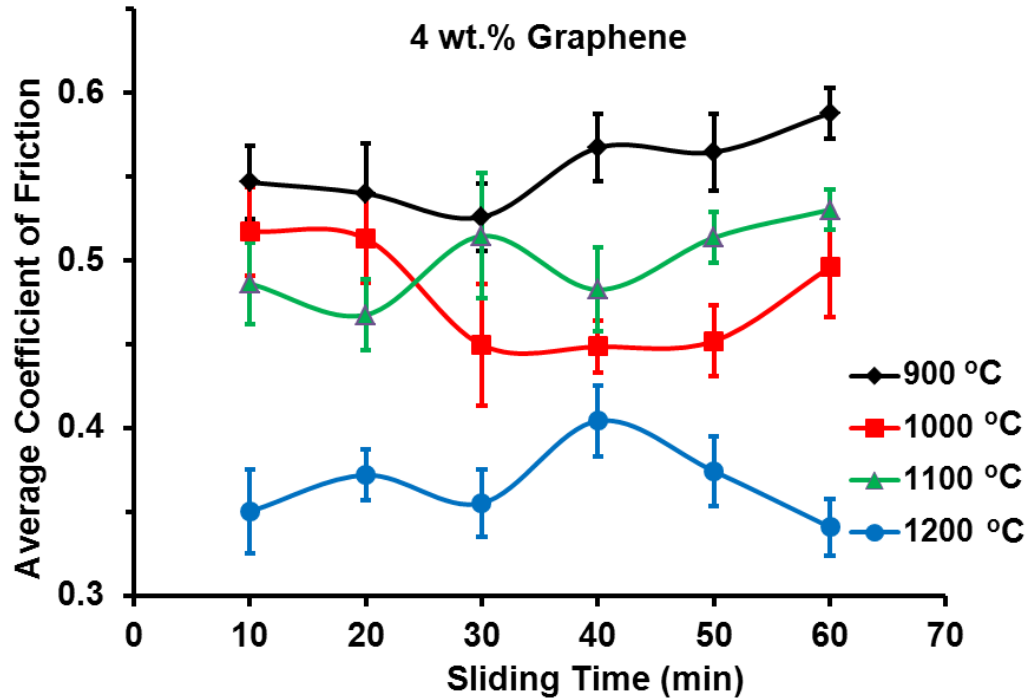
**Fig. 3.33** Total weight loss as a function of sliding time of sintered titanium aluminide composites samples (0, 2, 4 wt.% graphene) fabricated at different temperatures.

Fig. 3.34 presents average coefficient of friction values of titanium aluminide composites (2 wt.% graphene) sintered at different temperatures. Significant decrease in coefficient of friction was observed as the sintering temperature increases. The average recorded values of coefficient of friction of titanium aluminide (0 wt.% graphene) is 0.62. However, sintering titanium aluminide composites (2 wt.% graphene) at 1200 °C led to an average coefficient of friction as low as 0.35. Therefore, the role of sintering temperature was also noticed. Decrease in coefficient of friction can be mainly attributed to the presence of graphene which acted as a solid lubricant during the wear test [85]. Considering the atomic structure of graphene which has two dimensional covalent bonding and Van der Waals bonding in the third dimension between layers, solid lubrication comes through the ease of shearing of weak Van der Waals bond resulting in good frictional behavior [86]. Although contribution of graphene was observed in decreasing the coefficient of friction of titanium aluminide composites (2 wt.% graphene), samples were not intensively influenced by the further increase of graphene to 4 wt.%. Coefficient of friction values

of titanium aluminide composite samples (4 wt.% graphene) are similar to that of samples with 2 wt.% graphene as presented in Fig. 3.35. Samples sintered at 1200 °C exhibited the lowest coefficient of friction ( $\sim 0.35$ ) while other samples fabricated at 900 °C, 1000 °C, and 1100 °C showed coefficient of friction of  $\sim 0.55$ ,  $\sim 0.45$  and  $\sim 0.5$ , respectively. Therefore, it is reasonable to attribute this decrease in coefficient of friction of titanium aluminide composites (2 and 4 wt.% graphene) to the dual effect coming from addition of graphene and increasing the sintering temperature.



**Fig. 3.34** Average coefficient of friction as a function of sliding time of sintered titanium aluminide composite samples (2 wt.% graphene) fabricated at different temperatures.



**Fig. 3.35** Average coefficient of friction as a function of sliding time of sintered titanium aluminide composite samples (4 wt.% graphene) fabricated at different temperatures.

Fig. 3.36 presents the depth and width profiles across the worn surface of titanium aluminide composite samples (2 wt.% graphene) SPS over temperature range of 900 °C-1200 °C. Comparing all the four curves, it can be seen that sample sintered at 900 °C shows higher depth while samples fabricated at other temperatures exhibited better results. Therefore, wear track line profiles fall and weight loss data of sample sintered at 900 °C confirm the increase in depth of titanium aluminide composites samples. Also, surface profiles of the wear track of all SPS titanium composites samples (2 wt.% graphene) are shown in Fig. 3.37. The wear track surface profile of sample fabricated at 900 °C show the highest values of track width and depth.

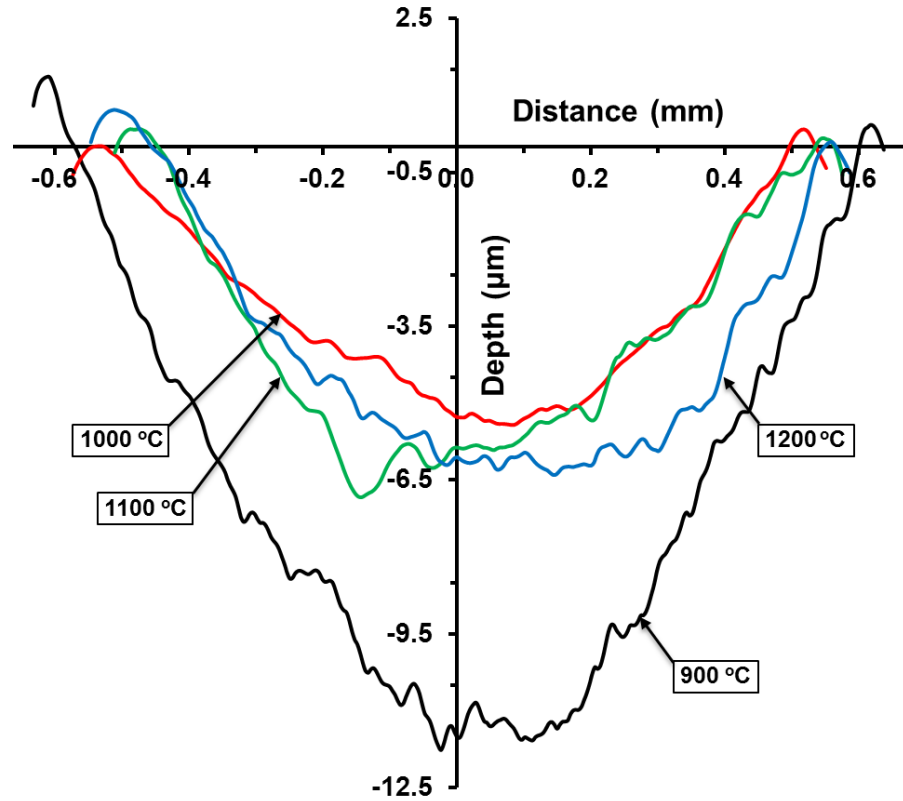


**Fig. 3.36** Line profiles across the wear track of SPS titanium aluminide composite samples (2 wt.% graphene) fabricated at different temperatures.

The depth and width profiles across the wear track of titanium aluminide composite samples (4 wt.% graphene) sintered over temperature range of 900 °C-1200 °C are presented in Fig. 3.38. Further increase in graphene content to 4 wt.% resulted in slight decrease in depth of the wear track for temperature 1000 °C, 1100 °C and 1200 °C. It can be seen that sample sintered at 900 °C exhibited the highest track depth and width. Fig. 3.39 presents surface profiles across the wear track of all SPS titanium composites samples (4 wt.% graphene). Surface profiles results show that sample fabricated at 1200 °C exhibits better wear behavior of this particular composition.



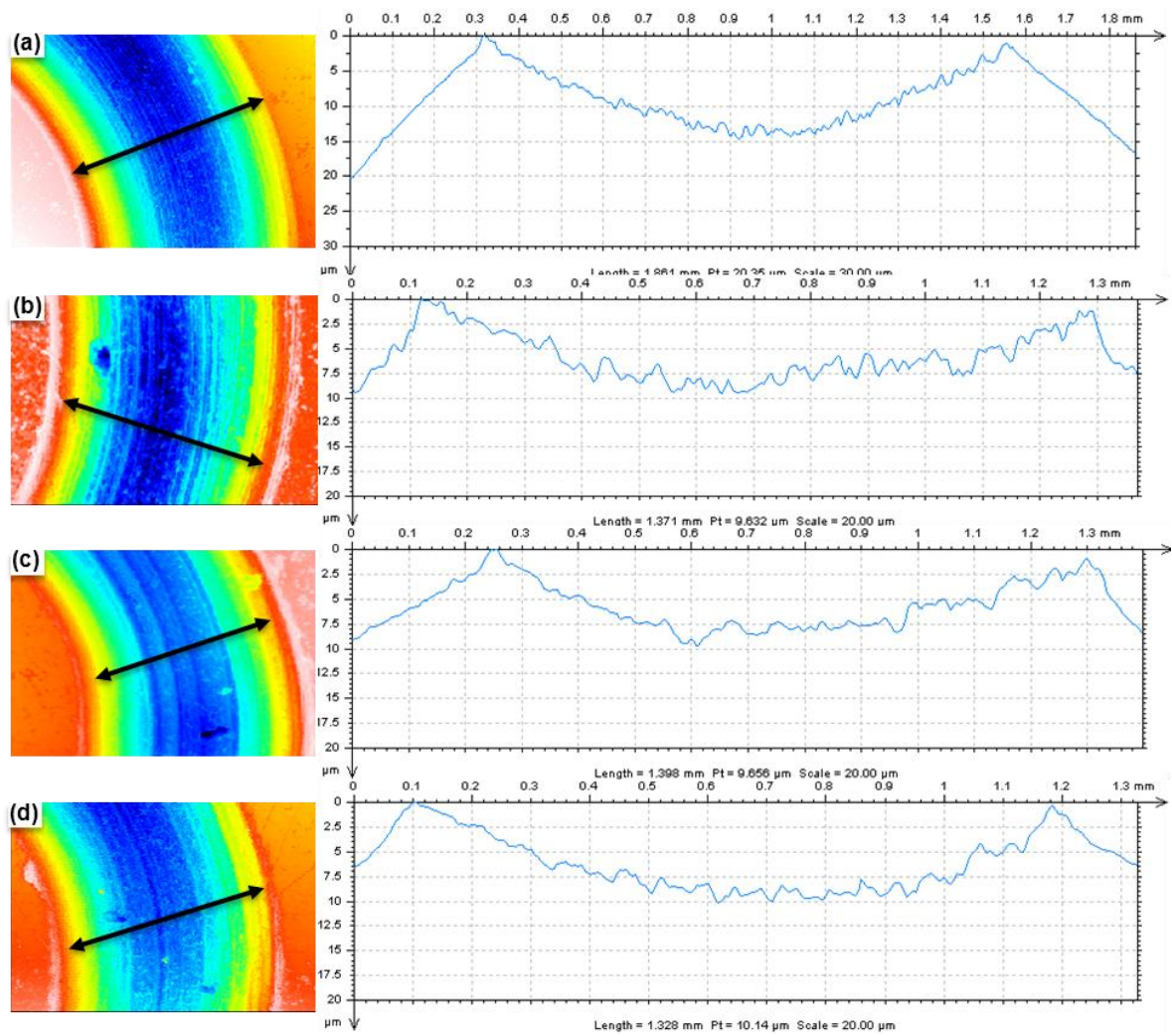


**Fig. 3.37** Surface profiles of wear tracks of sintered titanium aluminide composites (2 wt.% graphene) fabricated at (a) 900 °C, (b) 1000 °C, (c) 1100 °C, and (d) 1200 °C.



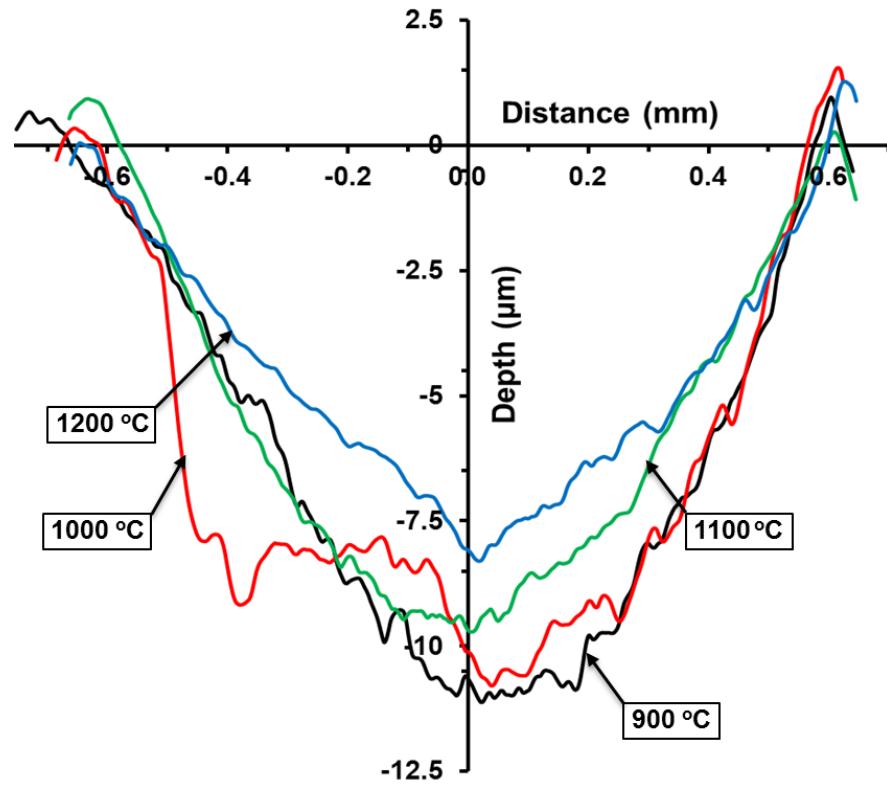


**Fig. 3.38** Line profiles across the wear track of SPS titanium aluminide composite samples (4 wt.% graphene) fabricated at different temperatures.

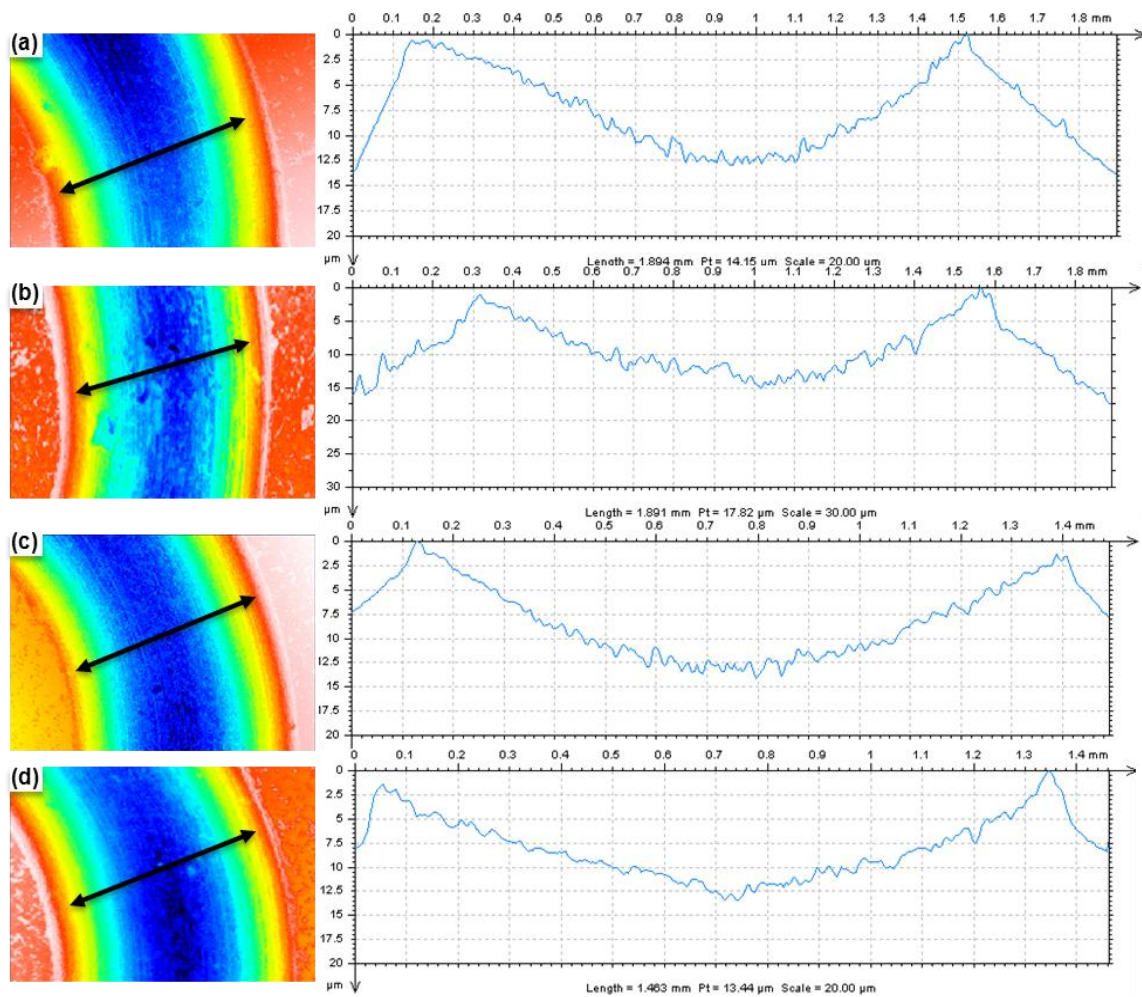


**Fig. 3.39** Surface profiles of wear tracks of sintered titanium aluminide composites (4 wt.% graphene) fabricated at (a) 900 °C, (b) 1000 °C, (c) 1100 °C, and (d) 1200 °C.

## CHAPTER 4

### CONCLUSIONS

- SPS of Ti-aluminide intermetallics through reactive synthesis route resulted in highly dense compacts (~ 100%) at a sintering temperature of 1100 °C.
- Reactive sintering led to formation of  $\gamma$ -TiAl . Small XRD peaks of other intermetallic phases were present indicating the formation of lamellar microstructure.
- $\gamma$ -TiAl phase was the predominant phase in all samples sintered at 900 °C, 1000 °C, 1100 °C and 1200 °C. Small XRD peaks of other intermetallic phases were present.
- Although change in microstructures was observed, microhardness did not exhibit significant change because TiAl and Ti<sub>3</sub>Al have similar properties. Compressive yield and ultimate strength were found to be higher for samples sintered at 1100 °C. Sample sintered at 1200 °C exhibited better toughness due to increase of lamellar phase.
- Sample fabricated at 1100 °C exhibited higher wear properties (weight loss and coefficient of friction) due to its high density.
- Addition of graphene resulted in a decrease in density of titanium aluminide composites.
- An increase in microhardness was observed with the increase of graphene in samples fabricated at 1100 °C and 1200 °C because of the restricted grain growth caused by graphene.

- Carbide phases (TiC, and Al<sub>4</sub>C<sub>3</sub>) were not observed during spark plasma sintering of titanium aluminide composites.  $\gamma$ -TiAl phase remained the predominant phase in all titanium aluminide composites samples at different processing temperatures.
- Compressive yield strength decreased for 2 wt.% and 4 wt.% graphene due to insufficient dispersion of graphene and decrease in density and due to absence of lamellar phase.
- Titanium aluminide composites exhibited slight increase in wear weight loss, but significant decrease in coefficient of friction was noticed due to solid lubrication caused by graphene (1200 °C).

## **CHAPTER 5**

### **FUTURE WORK**

- To perform detailed corrosion analysis of titanium aluminide composites.
- To understand interfacial properties between titanium aluminides and GNPs using Raman spectroscopy analysis.
- To investigate fracture toughness of SPS titanium aluminide composites.
- To investigate thermal conductivity and thermal expansion of titanium aluminide composites.

## REFERENCES

- [1] G. Sauthoff, Intermetallics VCH, Weinheim ;;New York, 1995.
- [2] R.L. Fleischer, D.M. Dimiduk, H.A. Lipsitt, Annual Review of Materials Science 19 (1989) 231-263.
- [3] J.E. Hatch, Aluminum : properties and physical metallurgy, Aluminum Association, American Society for Metals, 2005.
- [4] G. Sauthoff, in: P. Beiss, R. Ruthardt, H. Warlimont (Eds.), Refractory, Hard and Intermetallic Materials
- [5] M.A. Imam, F.H. Froes, K.L. Housley, in, Kirk-Othmer Encyclopedia of Chemical Technology, John Wiley & Sons, Inc., 2000.
- [6] G. Lütjering, J.C. Williams, Titanium (2nd Edition), Springer - Verlag, 2007.
- [7] L. Edward A, Intermetallics 8 (2000) 1339-1345.
- [8] J. Schuster, M. Palm, Journal of Phase Equilibria and Diffusion 27 (2006) 255-277.
- [9] J.R. Jokisaari, S. Bhaduri, S.B. Bhaduri, Materials Science and Engineering: A 394 (2005) 385-392.
- [10] S. Sastry, H. Lipsitt, Metallurgical and Materials Transactions A 8 (1977) 1543-1552.
- [11] Y.L. Hao, R. Yang, Y.Y. Cui, D. Li, Acta Materialia 48 (2000) 1313-1324.
- [12] C. McCullough, J.J. Valencia, C.G. Levi, R. Mehrabian, Acta Metallurgica 37 (1989) 1321-1336.
- [13] Z.G. Liu, G. Frommeyer, M. Kreuss, Scripta Metallurgica et Materialia 25 (1991) 1205-1210.
- [14] F.H. Froes, C. Suryanarayana, D. Eliezer, Journal of Materials Science 27 (1992) 5113-5140.
- [15] M.H. Yoo, C.L. Fu, J.K. Lee, J. Phys. III France 1 (1991) 1065-1084.

- [16] S. Djanarthany, J.C. Viala, J. Bouix, *Materials Chemistry and Physics* 72 (2001) 301-319.
- [17] Y.W. Kim, *Acta Metallurgica et Materialia* 40 (1992) 1121-1134.
- [18] Y-W. Kim, D. Dimiduk, *Journal of Materials* 43 (1991) 40-47.
- [19] D.M. Dimiduk, P.L. Martin, Y.W. Kim, *Materials Science and Engineering: A* 243 (1998) 66-76.
- [20] M. Hasegawa, H. Fukutomi, *Materials Science and Engineering: A* 508 (2009) 106-113.
- [21] M. Enoki, T. Kishi, *Materials Science and Engineering: A* 192–193, Part 1 (1995) 420-426.
- [22] Y.W. Kim, *Journal of Materials* 41 (1989) 24-30.
- [23] K. Young-Won, *Materials Science and Engineering: A* 192–193, Part 2 (1995) 519-533.
- [24] Leyens C., Peters M., *Titanium and Titanium Alloys: Fundamentals and Applications*, WILEY-VCH, 2003.
- [25] Y.W. Kim, *Journal of Materials* 46 (1994) 30-39.
- [26] P.A. Bartolotta, D.L. Krause, N.G.R. Center, National Aeronautics and Space Administration, GRC, Springfield, VA, 1999.
- [27] J.P. Immarigeon, R.T. Holt, A.K. Koul, L. Zhao, W. Wallace, J.C. Beddoes, *Materials Characterization* 35 (1995) 41-67.
- [28] V.S.S. Moxson, Fusheng; Draper, Susan L.; Froes, F. H.; Duz, V, NASA (2003).
- [29] NASA Glenn Research Center, LEW-17173, , NASA Tech Briefs Cleveland, OH (2002).
- [30] H. Mehrer, M. Eggersmann, A. Gude, M. Salamon, B. Sepiol, *Materials Science and Engineering: A* 239–240 (1997) 889-898.
- [31] M. Koiwa, *Materials transactions. JIM* 39 (1998) 1169.
- [32] C. Herzig, S. Divinski, *Intermetallics* 12 (2004) 993-1003.
- [33] C. Herzig, T. Przeorski, Y. Mishin, *Intermetallics* 7 (1999) 389-404.
- [34] A.K. Vasudévan, J.J. Petrovic, *Materials Science and Engineering: A* 155 (1992) 1-17.
- [35] D. D.M, *Materials Science and Engineering: A* 263 (1999) 281-288.

- [36] X. Wu, *Intermetallics* 14 (2006) 1114-1122.
- [37] E.A. Loria, *Intermetallics* 8 (2000) 1339-1345.
- [38] G. Das, H. Kestler, H. Clemens, P. Bartolotta, *JOM Journal of the Minerals, Metals and Materials Society* 56 (2004) 42-45.
- [39] N. T, *Intermetallics* 6 (1998) 709-713.
- [40] E.A. Loria, *Intermetallics* 9 (2001) 997-1001.
- [41] H. Clemens, H. Kestler, *Advanced Engineering Materials* 2 (2000) 551-570.
- [42] J.P. Kuang, R.A. Harding, J. Campbell, *Materials Science and Engineering: A* 329–331 (2002) 31-37.
- [43] V. Güther, C. Rothe, S. Winter, H. Clemens, *BHM Berg- und Hüttenmännische Monatshefte* 155 (2010) 325-329.
- [44] I. Weiss, S.L. Semiatin, *Materials Science and Engineering: A* 243 (1998) 46-65.
- [45] H. Clemens, A. Bartels, S. Bystrzanowski, H. Chladil, H. Leitner, G. Dehm, R. Gerling, F.P. Schimansky, *Intermetallics* 14 (2006) 1380-1385.
- [46] Y. Wang, Y. Liu, G.-y. Yang, H.-z. Li, B. Tang, *Transactions of Nonferrous Metals Society of China* 21 (2011) 215-222.
- [47] R. Gerling, H. Clemens, F.P. Schimansky, *Advanced Engineering Materials* 6 (2004) 23-38.
- [48] B. Préaucht, F. Popoff, M. Thomas, *Advanced Engineering Materials* 4 (2002) 133-138.
- [49] N.S. Stoloff, D.E. Alman, *Materials Science and Engineering: A* 144 (1991) 51-62.
- [50] M. Sujata, S. Bhargava, S. Suwas, S. Sangal, *Journal of Materials Science Letters* 20 (2001) 2207-2209.
- [51] E.K.Y. Fu, R.D. Rawlings, H.B. McShane, *Journal of Materials Science* 36 (2001) 5537-5542.
- [52] G. Wang, M. Dahms, *JOM Journal of the Minerals, Metals and Materials Society* 45 (1993) 52-56.
- [53] Y.S.G. Y. L. Yue, Q. Shen and L. M Zhang, *Key Engineering Materials* 249 (2003) 467-470.
- [54] J.C. Rawers, W.R. Wrzesinski, *Journal of Materials Science* 27 (1992) 2877-



2886.

- [55] V. Mamedov, Powder Metallurgy 45 (2002) 322-328.
- [56] D. Kopeliovich, Spark plasma sintering, 2010.
- [57] M. Tokita, Proceeding of NEDO International symposium (1999).
- [58] J.E. Garay, Annual Review of Materials Research 40 (2010) 445-468.
- [59] Z. Munir, U. Anselmi-Tamburini, M. Ohyanagi, Journal of Materials Science 41 (2006) 763-777.
- [60] E.A. Olevsky, S. Kandukuri, L. Froyen, Journal of Applied Physics 102 (2007) 114913-12.
- [61] M. Eriksson, Z. Shen, M. Nygren, Powder Metallurgy 48 (2005) 231-236.
- [62] T.-Y. Um, T. Abe, S. Sumi, Journal of Materials Synthesis and Processing 7 (1999) 303-309.
- [63] G. Molénat, M. Thomas, J. Galy, A. Couret, Advanced Engineering Materials 9 (2007) 667-669.
- [64] V. Recina, D. Lundström, B. Karlsson, Metallurgical and Materials Transactions A 33 (2002) 2869-2881.
- [65] F. Appel, M. Oehring, J.D.H. Paul, Advanced Engineering Materials 8 (2006) 371-376.
- [66] T.Y. Um, Ph.D. thesis Tohoku University, Japan (1994).
- [67] D.C. Dunand, Materials and Manufacturing Processes 10 (1995) 373-403.
- [68] K. Matsugi, N. Ishibashi, T. Hatayama, O. Yanagisawa, Intermetallics 4 (1996) 457-467.
- [69] I. Agote, et al., Intermetallics 16 (2008) 1310-1316.
- [70] Kattner U.R., Lin J.-C., C.Y. A., Metallurgical transactions A 23A (1992) 2081.
- [71] L. C. H., Journal of Materials Science Letters 17 (1998) 1367-1370.
- [72] Y.L.Y.e. al., Key Engineering Materials 249 (2003) 467.
- [73] M. Sujata, S. Bhargava, S. Sangal, Journal of Materials Science Letters 16 (1997) 1175-1178.
- [74] J.B. Yang, K.W. Teoh, W.S. Hwang, Journal of Materials Engineering and Performance 5 (1996) 583-588.
- [75] M.D. G.-X. Wang, Scripta Metallurgica et Materialia, 26 (1992) 717-722.

- [76] Y.Y. Chen, Yu, H.B., Zhang, D. & Chai, L.H. , Materials Science and Engineering: A 525(1-2) (2009) 166-173.
- [77] S.P. Brookes, H.J. Kühn, B. Skrotzki, H. Klingelhöffer, R. Sievert, J. Pfetzinger, D. Peter, G. Eggeler, Materials Science and Engineering: A 527 (2010) 3829-3839.
- [78] H. Sun, Sumi, Park and Abe, Acta Metallurgica Sinica 11 (1998) 417-424.
- [79] A. Couret, G. Molénat, J. Galy, M. Thomas, Intermetallics 16 (2008) 1134-1141.
- [80] C.L. Chu, S.K. Wu, Scripta Metallurgica et Materialia 33 (1995) 139-143.
- [81] A. Banerji, W. Reif, Metallurgical and Materials Transactions A 17 (1986) 2127-2137.
- [82] B. Yang, G. Chen, J. Zhang, Materials & Design 22 (2001) 645-650.
- [83] Y. Birol, Journal of Alloys and Compounds 460 (2008) L1-L5.
- [84] Y.M. Kim, C.D. Yim, B.S. You, Scripta Materialia 57 (2007) 691-694.
- [85] T. Filletier, J.L. McChesney, A. Bostwick, E. Rotenberg, K.V. Emtsev, T. Seyller, K. Horn, R. Bennewitz, Physical Review Letters 102 (2009) 086102.
- [86] J. Lin, L. Wang, G. Chen, Tribology Letters 41 (2011) 209-215.

## VITA

Abdelhakim Ahmed Aldoshan

Candidate for the Degree of

Master of Science

Thesis: SPARK PLASMA SINTERING OF TITANIUM ALUMINIDE INTERMETALLICS  
AND ITS COMPOSITES

Major Field: Mechanical and Aerospace Engineering

Biographical:

Education:

Completed the requirements for the Master of Science in Mechanical and Aerospace Engineering at Oklahoma State University, Stillwater, Oklahoma in July, 2012.

Completed the requirements for the Bachelor of Science in Mechanical Engineering at King Saud University, Riyadh, Saudi Arabia in 2005.

Experience:

Has over four years of experience as design engineer of mechanical parts of laser systems in Photonics Technology Center at KACST. Joined Nanotechnology Research Center at KACST in 2009. Two years of experience in processing intermetallic materials using Spark Plasma Sintering. Has expertise in characterizations of intermetallic phases of titanium aluminide composites.

Professional Memberships:

TMS, AIST, ASM.

Name: Abdelhakim Ahmed Aldoshan

Date of Degree: July, 2012

Institution: Oklahoma State University

Location: Stillwater, Oklahoma

Title of Study: SPARK PLASMA SINTERING OF TITANIUM ALUMINIDE  
INTERMETALLICS AND ITS COMPOSITES.

Pages in Study: 89

Candidate for the Degree of Master of Science

Major Field: Mechanical and Aerospace Engineering

**Scope and Method of Study:**

Titanium aluminide intermetallics are a distinct class of engineering materials having unique properties over conventional titanium alloys.  $\gamma$ -TiAl compound possesses competitive physical and mechanical properties at elevated temperature applications compared to Ni-based superalloys.  $\gamma$ -TiAl composite materials exhibit high melting point, low density, high strength and excellent corrosion resistance. Spark plasma sintering (SPS) is one of the powder metallurgy techniques where powder mixture undergoes simultaneous application of uniaxial pressure and pulsed direct current. Unlike other sintering techniques such as hot iso-static pressing and hot pressing, SPS compacts the materials in shorter time (< 10 min) with a lower temperature and leads to highly dense products. Reactive synthesis of titanium aluminide intermetallics is carried out using SPS. Reactive sintering takes place between liquid aluminum and solid titanium.

**Findings and Conclusions:**

In this work, reactive sintering through SPS was used to fabricate fully densified  $\gamma$ -TiAl and titanium aluminide composites starting from elemental powders at different sintering temperatures. It was observed that sintering temperature played significant role in the densification of titanium aluminide composites.  $\gamma$ -TiAl was the predominate phase at different temperatures. The effect of increasing sintering temperature on microhardness, microstructure, yield strength and wear behavior of titanium aluminide was studied. Addition of graphene nanoplatelets to titanium aluminide matrix resulted in change in microhardness. In Ti-Al-graphene composites, a noticeable decrease in coefficient of friction was observed due to the influence of self-lubrication caused by graphene.

ADVISER'S APPROVAL: Dr. Sandip P. Harimkar

---